Deliverable No. 3: Project K5/2338/1

Progress Report 2: River Reaches 1st year SW-GW connectivity determination & Surface Energy Balance Results

Quantification of transmission processes along the Letaba River for improved delivery of environmental water requirements (Ecological Reserve)

S Gokool[1], ES Riddell [1,3], T Strydom [1,2], C Jarmain [6], JM Nel [5], A Swemmer [4],

With inputs from R Minnaar[5]

1 **Centre for Water Resources Research, University of KwaZulu-Natal**

2 **Scientific Services, South African National Parks**

3 **Conservation Management, South African National Parks**

4 **SAEON Ndlovu Node, Phalaborwa**

5 **GCS Consulting, Pretoria**

6 **Private Agrometeorologist, Stellenbosch**

August 2015

TABLE OF CONTENTS

LIST OF FIGURES

LIST OF TABLES

1. Introduction

This deliverable report stems from the non-solicited Water Research Commission (WRC) research project K5/2338 titled:

Quantification of transmission processes along the Letaba River for improved delivery of environmental water requirements (Ecological Reserve)

This report covers progress to date in terms of river reaches surface energy balance results & SW-GW connectivity determination at the Letaba River Transmission Losses study site (Figure 1-1).

With financial support from the South African Environmental Observation Network (SAEON) as well as the Water Research Commission the project K5/2338 is now fully appointed, with the registration of the projects 2nd PhD student during April 2015. Both PhD students are registered at the Centre for Water Resources Research, University of KwaZulu-Natal, and both attended the specialist catchment monitoring training by SAEON at Cathedral Peak, KZN during April 2015.

This report presents data collected since the project commenced in April 2014, which includes:

- A continuation of the literature review presented in Deliverable 1 (October 2014), now with a focus on the Total Evaporation component of the Transmission Losses processes and ways in which this will be determined in this study.
- There then follows a presentation of the auto-classification process of remote sensing data available for the study site in order to classify the site into vegetation and miscellaneous objects based on spectral analysis of the terrestrial features.
- The Surface Energy Balance System (SEBS) analysis of the catchment and study site is performed using MODIS and LandSat-8 imagery, for a historical contextual determination of actual Total evaporation (i.e. evaporation and transpiration) at the site, and during the site specific surface energy balance campaigns which commenced in June 2015.
- Preliminary data from the Eddy Co-variance system is presented to show the components of the surface energy balance at the study site.
- A drilling report is presented for the study site, with progress to date on the installation of piezometric borehole network.
- Preliminary data is presented on the mass balance approach to estimate total Transmission losses between the two weirs at the study site.

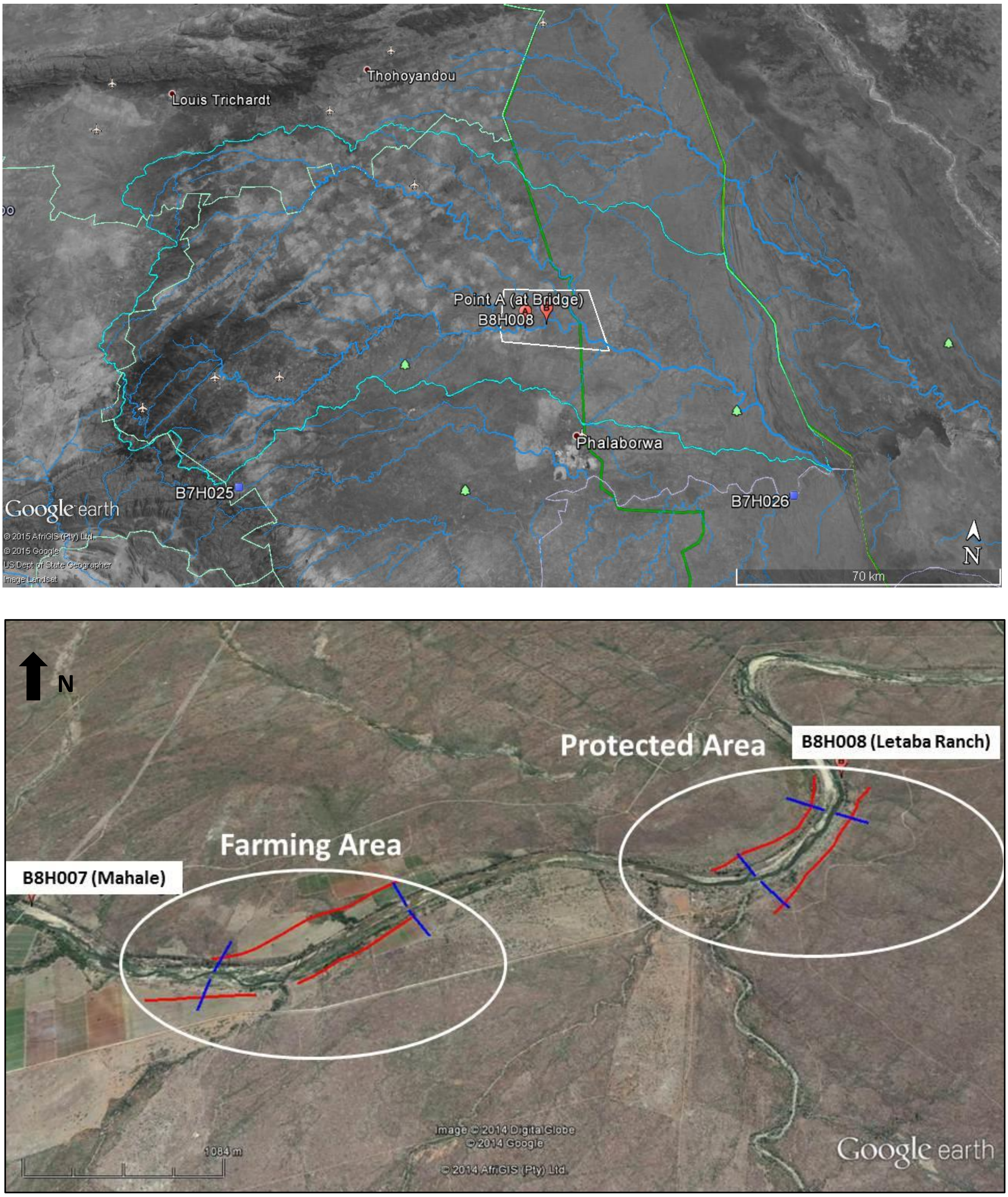

Figure 1-1 The location of the Transmission Losses study site within the Letaba catchment (above) and the study site with geophysics transects over two different land-uses (below).

2. Literature Review on Energy Balance studies in respect of Transmission Losses

The hydrological characteristics of South African catchments display a high degree of variability, which is largely due to its climatic zones which range from the tropical to the exceedingly arid. The variability in hydrological processes such as streamflow and runoff is notably high in semi-arid zones (McMahon, 1979). The efficient management of our limited water resources especially in the semi-arid and arid zones is therefore dependent on our ability to comprehensively quantify all hydrological processes, to enable us to understand and account for how these processes impact the flows within our river systems (van Dijk and Renzullo, 2011).

Presently, knowledge regarding precipitation inputs to a river system, releases from dams and water abstractions from river systems, which are relatively easy to quantify, have been used to manage the flows within river operations. However the lack of an adequate quantitative understanding with regards to the loss of water to streamflow transmission losses, hereafter referred to as TL, remains a constraint to the effective management of flows especially in arid and semi-arid environments (Hughes, 2008; Cataldo, 2010; Costa *et al.*, 2013).

TL can be defined as a reduction in the volume of flow in a river/stream channel system between upstream and downstream points (Lane *et al.*, 1990; Walters, 1990; Hughes and Sami, 1992; Cataldo *et al.*, 2010; Shanafield and Cook, 2014). The reduction in the flow volume between the upstream and downstream points is attributed to the loss of water through three natural processes i.e. (a) Total evaporation in the riparian zone and open water evaporation from the river channel, (b) evaporation or infiltration of water, stored in channel depressions or the flood plain and (c) the recharge of ground water as water infiltrates the stream channel, its banks or the floodplain (Cataldo *et al.*, 2010).

TL are a significant contributing process to the water balance of river systems, particularly in arid and semi-arid environments (Hughes and Sami, 1992; Lange, 2005; Hughes, 2008; Costelloe *et al.*, 2003; Cataldo *et al.*, 2010; Shanafield and Cook, 2014; Huang *et al.*, 2015). The significance of this process has been well documented for arid and semi-arid environments, yet there remains a paucity of studies on streamflow channel TL in southern Africa (Hughes, 2008).

Hydrological models and their associated tools have commonly been used as decision support systems by water resources managers, practitioners and scientists, to guide and inform water resources strategies, policies and management (van Dijk and Renzullo, 2011; Mengistu *et al.*, 2014). More specifically, these models can and are often used to facilitate the implementation of the ecological reserve, to assist with near real-time management of water resources (Hughes *et al.*, 2008).

However the general dearth of a qualitative and quantitative understanding of TL in southern Africa, at various spatial and temporal scales remains a major limiting factor, to the successful implementation and development of hydrological models, as these models currently possess or will possess a restricted conceptualization of hydrological processes, especially in semi-arid and arid environments.

The failure to address this limitation will pose a significant constraint to the effective management of ecological reserve flows in semi-arid and arid environments in the future, as Kirchner, (2006); Wagener *et al.* (2010) and van Dijk and Renzullo (2011) amongst others, highlight that the successful application of hydrological models as decision support systems is primarily driven, not only by the quality of the data being incorporated into them but by the representation of the system being modelled as well.

The general objective of this study is to reduce the uncertainty associated with the estimation of TL, which includes the riparian total evaporation component of TL. The majority of TL in most ephemeral rivers is a result of infiltration-based losses rather than riparian total evaporation losses (Cataldo *et al.*, 2010). Accordingly, research and TL estimation techniques have tended to focus more on the flow reduction in relation, to infiltration (Cataldo *et al.*, 2010; Shanafield and Cook, 2014).

2.1. Incorporating the Total Evaporation Process into Streamflow Transmission Losses Estimation Procedures

Even though there are various factors which have been identified to have an influence on the TL process, only a select few parameters have been successfully incorporated into TL estimation techniques (Hacker, 2005). Runoff volume and velocity, the river channel geometry and characteristics of the channel bed material are amongst the most commonly utilized factors for TL estimation procedures (Hacker, 2005). Ultimately, the choice of factors used for TL estimation procedures is controlled by the characteristics of the study-site and the availability of data (Cataldo *et al.*, 2004). However, one of the factors which is seldom included or adequately represented in TL estimation procedures is the total evaporation process.

It is often the case that total evaporation is ignored or inadequately represented in the TL estimation procedures, even though it has been identified as a contributing process to TL (Hacker, 2005; Cataldo *et al.*, 2010; Shanafield and Cook, 2014). Research and transmission loss estimation techniques have tended to focus more on the flow reduction in relation, to infiltration (Hacker, 2005; Cataldo *et al.*, 2010; Shanafield and Cook, 2014). This is largely due, to majority of TL in most ephemeral rivers occurring as a result of infiltration-based losses (Cataldo *et al.*, 2010).

Although infiltration-based losses may possess a relatively larger contribution to TL, the absolute losses, resulting from total evaporation cannot be discounted. This is particularly pertinent, to environments where total evaporation is a considerably large component of the water cycle (Everson, 2001; McKenzie, 2001; Hacker, 2005; Shanafield and Cook, 2014). According to Shanafield and Cook (2014), all processes which influence TL need to be quantified in order to fully understand the magnitude and effects of TL.

The accurate quantification of hydrological processes such as the role of riparian total evaporation and open water evaporation must be acknowledged and accounted for to successfully model TL.

2.2. Review of Current Techniques to estimate Total Evaporation based on Satellite Earth Observation Data

The use of satellite earth observation data to estimate total evaporation began approximately four decades ago in the late 1970's. The type of evaporation models incorporating satellite earth observation data to estimate total evaporation gradually evolved over time, becoming more complex in nature in comparison to their predecessors (Jarmain *et al.*, 2009). According to Courault *et al.* (2005), there are four broad classes of techniques, which are based on satellite earth observation used to estimate total evaporation. These include; (i) empirical direct methods, (ii) deterministic methods, (iii) the vegetation index approach and (iv) techniques based on the parameterisation of the energy balance.

i. Empirical direct methods of estimating total evaporation incorporate satellite earth observation data directly into semi-empirical models. (Courault *et al*, 2005). This technique is based on the assumption that the daily total evaporation can be directly related to the instantaneous difference between the air and surface temperature. The surface temperature can be estimated, using thermal infrared measurements from satellite earth observation data for the regional scale (Courault *et al*, 2005). This technique has been widely used to map total evaporation over large geographic areas based on surface temperature measurements (Lagouarde and Brunet, 1991; Courault *et al*, 1994).
ii. Deterministic methods are generally based on complex models such as the Soil-Vegetation-Atmospheric Transfer models which are used to determine the different components of the energy budget (Courault *et al*, 2005). Satellite earth observation data is used in this technique, either as an input parameter to describe various surfaces, or in an assimilation procedure, which aims to attain the necessary parameters required for the total evaporation computation (Courault *et al*, 2005).
iii. Vegetation index methods also known as inference methods utilize satellite earth observation data to compute a reduction factor such as the crop coefficient or the Priestley-Taylor alpha parameters (Courault *et al*, 2005). This is then used in conjunction with the reference evaporation which can be obtained from field measurements, to estimate the total evaporation (Courault *et al*, 2005).
iv. Techniques based on parameterisation of the energy balance combine some empirical relationships with physical modules to determine the total evaporation. Satellite earth observation data as well as meteorological data is used directly in these models to estimate the input parameters, which are required for the total evaporation computation (Courault *et al*, 2005).

The advantages and disadvantages of each of the aforementioned techniques are listed in Table 2.1 and have been discussed in Courault *et al* (2005), Jarmain *et al* (2009) and Timmermans (2014). Taking into consideration the relative strengths and weaknesses associated with each technique, the technique based on, utilizing the parameterisation of the energy balance, to estimate total evaporation was chosen, to be applied in this study, as it can be applied operationally, involves little to no cost and possesses minimal data requirements

Table 2.1 A summary of advantages and disadvantages of the different approaches used to estimate total evaporation from remote sensing data

Summary of advantages and disadvantages of the different approaches used to estimate total evaporation from remote sensing data		
Technique	**Advantages**	**Disadvantages**
Empirical	Operational from local to regional scale	Spatial variations of coefficients
Deterministic	Very detailed in their descriptions	Large number of input parameters, long computation times
Vegetation Index Methods	Simple parameterisation of processes	Only valid for specific conditions, does not account for all surface flux components needed in land surface and climate models
Parameterisation of the energy balance	Operational, low cost, minimal data requirements	Some empirical relationships, dry and wetland requirements to estimate the sensible heat flux

The estimation of total evaporation as a parameterisation of the shortened energy balance is a commonly applied technique for both operational and scientific research purposes (Mu *et al.*, 2007; Senay *et al.*, 2007; Jarmain *et al.*, 2009; Long and Singh, 2012). There are a vast number of total evaporation models which are based on the aforementioned technique. Some of the commonly applied techniques include the Surface Energy Balance Index (SEBI, Menenti and Choudary 1993), the Surface Energy Balance Algorithm for Land (SEBAL, Bastiaansen *et al.*, 1998a), the Mapping Total evaporation at High Resolution with Internalized Calibration (METRIC, Allen *et al*. (2007), and the Surface Energy Balance System (SEBS, Su 2002) and. The advantages and disadvantages of each of the aforementioned techniques are listed in Table 2.2 and have been discussed in Allen *et al*. (2007), Bastiaansen *et al*. (1998a); (2000), Su (2002), Jarmain *et al.* (2009), Li *et al.*, (2009) and Jovanovic and Israel, (2012). Taking into consideration the relative strengths and weaknesses associated with each technique, the SEBS Model was chosen to be applied in this study as it is open source software which can easily be obtained and utilized. The SEBS model is discussed in detail in the following sub-section.

Table 2.2 A limited list of techniques which are based on the parameterisation of the energy balance to estimate total evaporation through the incorporation of satellite earth observation data

Technique	Advantages	Disadvantages
SEBI	Directly relates the effects of temperature and aerodynamic resistance to the latent energy	Requires a lot of field-based measurements, evaporative fraction is assumed to be constant in order to estimate daily total evaporation
SEBAL	Minimal data requirements, physical concept, land use not required, multi-sensor approach	User defined hot and cold pixels, only applicable to flat terrain, evaporative fraction is assumed to be constant in order to estimate daily total evaporation, not open source
METRIC	Similar to SEBAL but surface slope and aspect can be considered	Uncertainty in the determination of hot and cold pixels, up-scaling of instantaneous total evaporation to daily total evaporation based on the ratio of the instantaneous total evaporation and the reference crop evaporation at the time of satellite overpass .
SEBS	No *a priori* knowledge of actual turbulent fluxes needed, computes roughness height of heat transfer instead of using fixed values, open source software available in ILWIS, application of the model is fairly user-friendly, Less assumptions are made then in other techniques and the energy balance is solved with more physical parameterizations in the SEBS formulation.	Dry and wetland requirement to determine the sensible heat flux, combined with Penman-Monteith equation, too many parameters are required, solution to determine turbulent heat flux is fairly complex, evaporative fraction is assumed to be constant in order to estimate daily total evaporation.

2.3. The SEBS Model

The SEBS Model is one of the commonly applied satellite-based techniques utilized to estimate total evaporation and has been applied in a vast array of studies in area of different climate, topography and land uses, including but not limited to; Su (2002), Jin *et al*. (2005), Jarmain *et al.* (2009), Li *et al.* (2009), van de Kwaast et al. (2009), Gibson *et al.* (2011), Ma *et al*. (2011); (2012), Muhammed, (2012), Timmermans *et al*. (2013), Ershadi *et al.* (2014), Ma *et al*. (2014), Matinfar and Soorghali (2014), Mengistu *et al*. (2014), Pardo *et* *al.* (2014). The SEBS Model is easily accessible open source software, which is available in the Integrated Land and Water Information System (ILWIS).

The SEBS Model, developed by Su (2002), is a single-sourced surface energy balance model which can be utilized to estimate turbulent fluxes within the atmosphere or to determine the evaporative fraction through the use of remote sensing and meteorological data at both local and regional scales (Su, 2002). The SEBS model permits the use of data obtained from a variety of satellite sensors, which is available at varying spatial, temporal and spectral resolutions.

A number of tools are presented within the Model, which integrate meteorological data and satellite earth observation data to estimate daily total evaporation (Su, 2002). Su (2002) states that there are three primary sets of data required by SEBS to estimate the daily total evaporation for any region. This data is obtained from two sources i.e. through satellite earth observation systems measuring spectral reflectances and radiances of the land surface and meteorological stations. Satellite earth observation data is used to provide information for a number of land surface parameters required by SEBS, including the land surface albedo, land surface temperature, emissivity, fractional vegetation cover, leaf area index, vegetation roughness height and the normalized difference vegetation index (NDVI) (Su *et al.*, 2001; Su 2002).

Climatic data such as wind speed, air temperature, air pressure at a reference height, humidity and sunshine hours, are obtained from the meteorological stations. Radiation data i.e. the downward short-wave radiation, is also required by SEBS; however, this can be obtained from various sources and is not restricted to one particular source of the two previously described sources (Su *et al.*, 2001; Su, 2002).

The various input data required by SEBS is incorporated into three sub-models, to determine the components of the energy balance, stability factors and the roughness length of heat transfer (Su *et al.*, 2001; Su, 2002). The three sub-models are then used to estimate the evaporative fraction at limiting cases. The evaporative fraction in SEBS is assumed to be constant for the entire day and the daily total evaporation can then be determined from the available latent heat energy (Su *et al.*, 2001; Su, 2002).

The use of remote sensing data within SEBS improves the spatial representation of the estimates, whilst simultaneously accounting for the heterogeneity of the land surface over increasing geographic scales (Su, 2002). In addition to the various SEBS pre-processing functions available in ILWIS, SEBS possesses the added advantage of determining land surface physical parameters such as albedo, fractional vegetation cover and NDVI, amongst others (Su, 2002). The open-source nature of SEBS as well as the previously described advantages make it a promising tool which can be used as a decision support system for water resources research, planning and management.

2.4. Determination of Total Evaporation within SEBS

A number of equations are used to determine the daily total evaporation within SEBS. Satellite data derived from spectral reflectances and radiances of the land surface as well as meteorological data are used to determine the various variables outlined in these equations (Su, 2002). The following equations are used to determine the daily total evaporation in SEBS:

2.4.1. The simplified surface energy balance

The simplified surface energy balance equation is given as (Su, 2002):

$$\mathbf{Rn - G_o - H - \lambda ET = 0} \qquad \textbf{Equation 2-1}$$

Where Rn is net radiation ($W.m^{-2}$); H is sensible heat flux energy ($W.m^{-2}$); G_o is soil heat flux energy ($W.m^{-2}$) and λET is latent heat flux energy ($W.m^{-2}$).

2.4.2. The net radiation

The net radiation equation is given as (Su, 2002):

$$\mathbf{Rn = (1 - \alpha)\, RS_{wd} + \varepsilon . RL_{wd} - \varepsilon . \sigma . T_o^4} \qquad \textbf{Equation 2-2}$$

Where α is land surface albedo; RS_{wd} is incoming solar radiation ($W.m^{-2}$); ε is surface emissivity; is RL_{wd} is incoming long wave radiation ($W.m^{-2}$); σ is Stefan Boltzman constant ($5.67x10^{-8}$ $W.m^{-}2.K^{-4}$) and T_o is the surface temperature (K).

2.4.3. The soil heat flux

Soil heat flux is one of the components of the energy balance equation. This energy flux enters the land surface during the day and exits the land surface at night. Generally, the soil heat flux is assumed to be zero over a 24-hour period (Muhammed, 2012). The soil heat flux equation is given as (Su, 2002):

$$\mathbf{G_o = Rn.[\Gamma_c + (1- f_c).(\Gamma_s - \Gamma_c)]} \qquad \textbf{Equation 2-3}$$

Where Γ_c is the ratio of soil heat flux to net radiation which is assumed to be equal to 0.05 for a fully vegetated canopy (Monteith, 1973) and Γ_s is the ratio of soil heat flux to net radiation which is assumed to be equal to 0.315 for a bare soil surface (Kustas and Daughtry, 1989). The fractional canopy coverage (f_c), which is derived from satellite earth observation, is then used to perform an interpolation between the two limiting cases described above (Su, 2002).

2.4.4. The sensible heat flux

The sensible heat flux is determined by applying the similarity theory and the Monin-Obukhov stability correction procedure (Su, 2002).The equations used to determine wind and temperature profiles in the vertical direction are given in Equations 2.4 and 2.5 as:

$$\mathbf{u = (u^*/k) \times [\ln((z-d_o)/z_{om}) - \psi_m \times ((z-d_o)/L) + \psi_m \times (z_{om}/L)]}$$

Equation 2-4

$$\mathbf{\theta_o-\theta_a = (H/ku^*\rho C_p) \times [\ln((z-d_o)/z_{oh}) - \psi_h \times ((z-d_o)/L) + \psi_h \times (z_{oh}/L)]}$$

Equation 2-5

In Equations 2.4 and 2.5; u and u^* are wind and the friction velocity ($m.s^{-1}$) respectively, z and d_o are reference meteorological height (m) and displacement height respectively (m), ρ is the density of air ($kg.m^{-3}$), C_p is the heat capacity of dry air (Jkg^{-1}), k is von Karman's constant (0.4), z_{om} and z_{oh} are the roughness height for momentum and scalar roughness height for heat transfer respectively (m), θ_o and θ_a are the potential surface temperature and air temperature respectively at height z (K), ψ_m and ψ_h are stability correction factors for momentum and sensible heat transfer respectively and L is the Obhukov length (m) which is calculated as:

$$\mathbf{L = -(\rho C_p u^{*3}\,\theta_v/kgH)} \qquad \textbf{Equation 2-6}$$

Where θv is the virtual temperature near the surface (K) and g is the acceleration due to gravity (ms^{-2}).

In order to estimate the sensible heat flux the roughness length for momentum (z_{om}) and scalar roughness height for heat transfer are required (z_{oh}). The scalar roughness height for heat transfer is estimated as:

$$\mathbf{z_{oh} = z_{om}/\exp(KB^{-1})} \qquad \textbf{Equation 2-7}$$

Where KB^{-1} is the inverse Stanton number which is a dimensionless heat transfer coefficient. In order to estimate the KB^{-1} value an extended model of Su *et al*. (2001) is proposed as:

$$\mathbf{KB^{-1} = [(kC_d/(4C_t) \times (u^*/(u(h))) \times (1-e^{Nec/2}) \times f_c^2] +}$$

$$\mathbf{[(2\, f_c f_s) \times ((k \times (u^*/(u(h))) \times (z_{om}/h)/\, C_t^*)) + (KB^{-1} \times f_s^2)]} \qquad \textbf{Equation 2-8}$$

Where C_d is the drag coefficient of foliage elements assumed to have a value of 0.2, N_{ec} is the within-canopy wind profile extinction coefficient, u(h) is the horizontal wind speed at the top of the canopy, f_c is the fractional vegetation cover and f_s is its complement, C_t is the heat transfer coefficient of the leaf which for most canopies and environmental conditions is bounded between $0.005N \leq C_t \leq 0.075N$ (N is the number of sides of the leaf which is involved in the heat transfer process).

C_t^* is the heat transfer coefficient of the soil given as $C_t^* = Pr^{-2/3} \times R_{e*}^{-1/2}$, where Pr is the Prandtl number and R_{e*} is the roughness Reynolds number which is estimated as $R_{e*} = h_s u_*/v$, where $h_s$is the roughness height of the soil and v is the kinematic viscosity of the air ($v = 1.327 \times 10^{-5} \times (p_o/p) \times (T/T_o)^{1.81}$ where p and T are the ambient pressure and temperature p_o = 101.3 Kpa and T_o = 273.5 K. For bare soils the KB^{-1} value can be estimated as:

$$\mathbf{KB_s^{-1} = 2.46(R_{e*})^{1/4} - \ln(7.4)} \qquad \textbf{Equation 2-9}$$

According to Su (2002) "the actual sensible heat flux is constrained in the range set by the sensible heat flux at the wet limit (H_{wet}) and the sensible heat flux at the dry limit (H_{dry})".

At, the dry limit, the latent heat is zero and the sensible heat flux possesses its maximum value due to, the limitation of soil moisture. The sensible heat flux under the dry limit is given as (Su, 2002):

$$\mathbf{H_{dry} = Rn - G_o} \qquad \textbf{Equation 2-10}$$

At, the wet limit, the sensible heat flux possesses its minimum value as evaporation can take place at near potential rates. The sensible heat flux at the wet limit is given as (Su, 2002):

$$\mathbf{H_{wet} = Rn - G_o - \lambda E_{wet}} \qquad \textbf{Equation 2-11}$$

2.4.5. The relative evaporation

The relative evaporation is given as (Su, 2002):

$$\mathbf{\Lambda r = \lambda E/\lambda E_{wet}}$$

$$\mathbf{= 1 - (\lambda E_{wet} - \lambda E/\ \lambda E_{wet})} \qquad \textbf{Equation 2-12}$$

Where Λr is the relative evaporation; λE is the latent heat at the dry limit and λE_{wet} is the latent heat at the wet limit

Su (2002) then incorporates Equations 2.1, 2.10, and 2.11 into Equation 2.6 to represent the relative evaporation as:

$$\mathbf{\Lambda r = 1 - [(H - H_{wet})/\ (H_{dry} - H_{wet})} \qquad \textbf{Equation 2-13}$$

2.4.6. The evaporative fraction

In order to, determine the evaporative fraction; Su (2002) combined Equation 2.11 and a combination equation similar to the Penman combination equation. According to Menenti, (1984) when the resistance terms are grouped into internal and external bulk surface resistances, the combination equation to determine the latent heat energy can be given as follows:

$$\mathbf{\lambda E = [\Delta \times r_e \times (Rn - G_o) + pc_p(e_s - e_a)] / [r_e(\gamma + \Delta) + \gamma \times r_i]}$$

Equation 2-14

Where Δ is the rate of change of saturated vapour pressure with temperature ($hPaK^{-1}$); r_e is aerodynamic resistance ($s.m^{-1}$); e_s is saturated vapour pressure (hPa); e_a is actual vapour pressure (hPa); γ is the psychometric constant(hPa.K^{-1}) and r_i is the bulk surface internal resistance (s.m^{-1}).

In Equation 2.14, it is assumed that the roughness length for heat transfer and vapour transfer are equal (Brutsaert, 1982). The Penman-Monteith equation only holds true for a vegetated canopy, however Equation 2.8 is valid for both a vegetated canopy and a soil surface with defined bulk surface internal resistance (Su, 2002).

The use of Equation 2.14 to determine the latent heat energy can be seen as problematic due to the difficulty in determining the bulk surface internal resistance, as this is regulated by the availability of soil moisture (Su, 2002).

Su (2002) proposes a solution to this problem by circumventing the use of the bulk surface internal resistance in the estimation of the latent heat energy. According to definition, the internal bulk surface resistance at the wet limit is equal to zero. Incorporating this value into Equation 2.14 and altering the variables to reflect wet limit conditions, the sensible heat flux is given as (Su, 2002):

$$\mathbf{H_{wet} = [(Rn - Go) - (pc_p/r_{ew})((e_s - e_a)/\gamma)] / ((1 + \Delta)/\gamma)}$$

Equation 2-15

The external resistance (r_{ew}) is a function of the Obukhov length, which sequentially is a function of the sensible heat flux and the friction velocity (Su, 2002) Equations 2.4 - 2.6. The friction velocity and the Obukhov length which have been determined previously can then be used to estimate the external resistance from Equation 2.5.

$$\mathbf{r_e = (1/ku^*) \times [\ln((z-d_o)/z_{oh}) - \psi_h \times ((z-d_o)/L) + \psi_h \times (z_{oh}/L)]}$$

Equation 2-16

Similarly the external resistance at the wet limit can be determined as:

$$\mathbf{r_{ew} = (1/ku^*) \times [\ln((z-d_o)/z_{oh}) - \psi_h \times ((z-d_o)/L_w) + \psi_h \times (z_{oh}/L_w)]}$$

Equation 2-17

The stability length at the wet limit can be determined as:

$$\mathbf{L_w = \rho u^{*3}/(k \times g \times 0.61 \times (Rn - G_o)/ \lambda)}$$

Equation 2-18

The evaporative fraction can then be determined and is given as follows (Su, 2002):

$$\mathbf{\Lambda = \lambda E/(Rn - G)}$$

$$\mathbf{= \Lambda r.\lambda E_{wet}/(Rn - G)}$$

Equation 2-19

2.4.7. Daily total evaporation

If the evaporative fraction is assumed to be constant throughout the day, the daily actual ET can then be estimated as (Su, 2002):

$$\mathbf{E_{daily} = 8.64x10^{7} \times \Lambda_o^{24} \times ((Rn_{24} - G_o)/ \lambda\rho_w)} \qquad \textbf{Equation 2-20}$$

Where E_{daily} is daily total evaporation (mm/day); Λ_o^{24} is the daily evaporative fraction; Rn_{24} is the daily net radiation which is measured *in situ* ($W.m^{-2}$); ρ_w is density of water ($kg.m^{-3}$) and λ is the latent heat of vaporization ($2.501-0.00237x\ T_{air})x10^{6}$ ($J.kg^{-1}$).

2.5. Limitations Associated with the use of the Pre-Packaged Version of SEBS and Satellite Earth Observation in The Estimation of Total Evaporation

The benefits of employing satellite-based evaporation estimation techniques can be invaluable to improve water resources management; however, it is important to note that these techniques do possess limitations, some of which are shared by all satellite earth observation techniques, whilst some limitations are technique specific. It is often difficult to obtain continuous total evaporation data series using satellite earth observation techniques due to the effects of cloud cover as well as the revisit and repeat cycle of any given satellite (Jarmain *et al.*, 2009; Mertz, 2010). Cloud coverage has a strong influence on the amount of reflected radiation, which can be measured from the earth's surface for both the optical and thermal wavelengths (Jarmain *et al.*, 2009; Timmermans, 2012).

The amount of images which can be processed is therefore dependent on the amount of cloud free images available. The availability of an image for a particular region is also influenced by the satellite revisit and repeat cycle. The revisit and repeat cycles vary, depending on the satellite sensor which is being used.

In addition to the aforementioned limitations, the resolution of the satellite sensor influences the accuracy of the daily total evaporation estimate which is obtained. An image obtained using a coarse resolution sensor will not be able to accurately account for the spatial heterogeneity of the land surface which is being captured (McCabe and Wood, 2006; Li *et al.*, 2008; Jarmain, 2009).

With regards to SEBS, the model is highly sensitive to the following four parameters i.e. the gradient between the land surface temperature and air temperature (Su, 2002), the fractional vegetation cover formula (Lin, 2006; Badola, 2009; van de Kwast *et al.*, 2009), the displacement height and the height of wind speed measurements (Timmermans *et al.*, 2005; van de Kwast *et al.*, 2009) and the spatial heterogeneity of the study area (McCabe, and Wood, 2006; Li *et al.*, 2008). A detailed description of the aforementioned sensitive parameters is presented in Gibson *et al.* (2011).

Within the SEBS Model, instantaneous total evaporation values are extrapolated to daily total evaporation values by assuming that the evaporative fraction remains constant throughout the day (Su, 2002). Research undertaken by Stewart (1996); Lhomme and Elguerro (1998); Gentine *et al.* (2007); (2011) and Mkhwanazi and Chavez (2013), indicate that assuming the evaporative fraction to be constant throughout the day may lead to the generation of erroneous daily total evaporation estimates, especially during advective conditions (Gentine *et al.*, 2007; Mkhwanazi and Chavez, 2013).

2.6. Case studies: Application of the SEBS Model

A vast array of studies exist which utilize the SEBS Model to estimate total evaporation, however, only a few select case studies will be discussed in this section. A brief description of these studies is presented below. The key findings for each of these studies are presented in Table 2.3.

Su (2002), proposed SEBS to estimate turbulent fluxes and the evaporative fraction, using satellite earth observation data. Three field data sets obtained from flux stations and one remote sensing data set obtained from the Thematic Mapper Simulator was used as inputs for the SEBS model. Four experimental data sets were then used to test the reliability of SEBS in this study.

Jarmain *et al*. (2009) conducted a study, to review techniques available to determine total evaporation utilizing satellite earth observation data and to recommend a technique that could be potentially applied in South Africa, in order to assist total evaporation estimation and water resources management. The SEBS model was one of the numerous techniques which were reviewed and applied. The SEBS model was applied to three study sites in South Africa i.e. Seven Oaks, St Lucia and Kirkwood. The simulated results were compared with a Kipp and Zonen Large Aperture Scintillometer, Surface Renewal and Eddy Covariance for each of the study sites, respectively.

Yang *et al*. (2010) applied the SEBS Model, to determine the water consumption of maize/wheat in the Northern China Plain. MODIS Level 1_B images from the period 2006 to 2008 and meteorological data obtained from a field-based flux tower were used as inputs to the SEBS model. The simulated total evaporation estimates were validated against the field-based measurements of the energy fluxes and total evaporation estimates obtained from an eddy covariance system.

Elhag *et al*. (2011) applied the SEBS model over the Nile delta, to estimate daily total evaporation. AATSR and MERIS Level 1_B data were used as inputs to SEBS, in conjunction with meteorological data obtained from six *in situ* meteorological stations. The simulated daily total evaporation estimates were compared against actual ground truth data taken from ninety-two points uniformly distributed over the study area.

Gibson *et al.* (2011) conducted a study in the Piketberg region in the Western Cape Province of South Africa, to investigate the uncertainties associated with the application of the pre-packaged version of SEBS in ILWIS. MODIS Level1_B, Advanced Spaceborne Thermal Emission and Reflection Radiometer (ASTER) Level 1_B and ASTER Level 2 data, as well as meteorological data obtained from an automatic weather station located in the study area were used in this study.

Rwasoka *et al.* (2011) applied the SEBS model, to determine the total evaporation of the Upper Manyame Catchment in Zimbabwe. Nine clear sky MODIS Level 1_B images and field-based meteorological data were used as inputs to SEBS to generate total evaporation estimates, which corresponded to the time of the satellite overpass. Two study sites were selected i.e. the Harare Kutsage Station and the Grasslands Station. The simulated total evaporation estimates were evaluated for physical/logical consistency, by comparing total evaporation estimates against reference evaporation, spatial variation of total evaporation and understanding the total evaporation of different land types.

Muhammed (2012) conducted a study to investigate the use of satellite earth observation data in a hydrological model. The SEBS Model was used to estimate daily total evaporation, which was one of the inputs required by the TOP model to simulate streamflow for the Upper Gilgal Abbay Basin. Streamflow volume estimates obtained, using SEBS estimates of total evaporation were compared against the streamflow volume estimates which were obtained by using the TOP Model total evaporation estimates.

Ma *et al*. (2014) applied the SEBS model, to determine the regional distribution of total evaporation over the NamCo region in the Tibetan Plateau, situated in the northwest of China. Two scenes of ASTER data for the 11th June 2006 and 25th February 2008 were used as inputs, to the SEBS Model, to estimate total evaporation. The simulated total evaporation estimates were validated against the field-based measurements of the energy fluxes and total evaporation estimates obtained from an eddy covariance system

Mengistu *et al*. (2014) applied the SEBS Model, to derive spatially representative total evaporation for the Baynesfield Estate in KwaZulu Natal South Africa, which would be used to assist in the calibration of hydro-meteorological models. MODIS Terra images and Landsat 7 EM+ were used as inputs to the SEBS Model for the estimation of total evaporation. The SEBS daily total evaporation estimates obtained using the MODIS Terra images and the Landsat 7 EM+ images were compared with Eddy covariance daily total evaporation measurements.

Table 2.3 Summary of key findings for limited list of case studies

STUDY	MAIN OBJECTIVE	SUMMARY OF KEY FINDINGS
Su, 2002	Assess the reliability of SEBS to estimate total evaporation	• SEBS can provide reliable estimates of H. • Errors in the estimation of H due to uncertainties in roughness height for heat transfer equations. • Stability corrections available at the time were inadequate.
Jarmain *et al.*, 2009	Review satellite based total evaporation techniques	• For two of the three sites SEBS estimates of R_n compared favourably with field observations. • SEBS failed to accurately simulate G for all three study sites it was applied to. • SEBS estimates of the sensible heat flux and the evaporative fraction were in good agreement with field observations for two of the three study sites.
Yang *et al.*, 2010	Determine the water consumption of maize/wheat in the Northern China Plain	• SEBS performed better during the wheat growing season than during the maize growing season. • The relative error in the estimation of LE was within 20% either within the wheat growing or maize growing season.
Elhag *et al.*, 2011	Determine total evaporation using SEBS	• SEBS total evaporation estimates were in good agreement with field based measurements. • The ability of the model to utilize satellite earth observation data with a high temporal resolution will assist decision makers to take into account the different plant growth phases and improve their real time water management strategies
Gibson *et al.*, 2011	Investigation of uncertainties associated with the pre-packaged version of SEBS in ILWIS	• The use of a coarse spatial resolution sensor is appropriate for catchment scale operations however at the field scale high spatial resolution imagery is required. • The pre-packaged version of SEBS in ILWIS was found to be most sensitive to; the land surface and air temperature gradient, choice of fractional vegetation cover formula, displacement height and height at which wind speed is measured, and the heterogeneity of the study area.

STUDY	MAIN OBJECTIVE	SUMMARY OF KEY FINDINGS
Rwasoka *et al.*, 2011	Determine total evaporation using SEBS	• On average SEBS performed well for the plausibility and consistency check. • SEBS performed well for the Harare-Kutsage station and poorly for the Grassland station, this was attributed to spatial variability of temperature, heterogeneity of the land surface and roughness parameterization. • Overall the model was found to be a useful tool to estimate spatial total evaporation.
Muhammed, 2012	Application of satellite based total evaporation estimates in a hydrological model	• SEBS total evaporation estimates were found to be realistic when related to the seasonal conditions of the study area. • The comparison between streamflow volume estimates obtained using SEBS estimates of total evaporation and streamflow volume estimates obtained using the TOP model total evaporation estimates, produced satisfactory results with a Nash-Sutcliffe efficiency of 0.78 and a relative volume error of 0.59
Ma *et al.*, 2014	Determine the regional distribution of total evaporation in the NamCo region in the Tibetan Plateau	• The SEBS model over-estimated the total evaporation for by 39.50% and 38.90% for 11th June 2006 and 25th February 2008, respectively, when compared with eddy covariance measurements. • The comparison between the observed data and the SEBS estimates yielded, a root mean square error value of 0.7mm/day.
Mengistu *et al.*, 2014	Provide accurate field and satellite estimates of total evaporation for the calibration of hydro-meteorological models	• The SEBS daily total evaporation estimates using MODIS Terra images, as well as, Landsat 7 EM+ were higher than Eddy covariance daily total evaporation estimates for the corresponding days. • The SEBS Model over-estimated the daily total evaporation by approximately 15% for these days.

3. Determining the Distribution of Vegetation Density and Identifying Land Uses

A vegetation/vegetative index can be used to quantify the plant vigour within a pixel of a satellite image. The index may be computed utilizing various satellite reflectance bands, which are sensitive to biomass and plant vigour. One of the most commonly applied vegetation indices is the normalized difference vegetation index (NDVI) (Ramsey *et al*., 2004).

The NDVI has been adopted to analyse satellite earth observation data *viz.* to assess if the region/feature which is being observed contains actively growing vegetation or not (Ghorbani *et al*., 2012). The behaviour of plant species across the electromagnetic spectrum is fairly well understood. As a result, NDVI information can be derived from satellite earth observation data, by analysing the satellite bands which highlight the greatest responses between vegetation and radiation. The satellite bands which are most responsive to the interactions between vegetation and radiation are the red and near infra-red bands of the electromagnetic spectrum (Ghorbani *et al*., 2012).

The reflectance of radiation in the visible portion of the electromagnetic spectrum (400-700nm) is low, due to the absorption of light energy by chlorophyll in actively growing green vegetation. Whereas, the reflectance of radiation in the NIR portion of the electromagnetic spectrum is high, due to the multiple scattering of light by plant leaf tissues (Zhang *et al*., 2011).

The algorithm used to derive the NDVI is given in Equation 3.1 as:

NDVI = (NIR Band – Red Band)/(NIR Band + Red Band) **Equation 3-1**

The difference between the red and NIR bands provides an indication of the amount of vegetation present in the region/feature being observed. The greater the difference between the red and NIR bands, the greater the amount of vegetation present and *vice versa* (Ghorbani *et al*., 2012).

Numerous vegetation studies have utilized the NDVI for wide ranging applications inter alia; estimating crop yields, pasture performance, vegetation health and biomass (Petorelli *et al*., 2005; Muskova et al., 2008). Furthermore, the NDVI technique generally allows for the identification of various features within a satellite image such as, areas which possess dense vegetation or no vegetation coverage (bare soil and rock), water bodies and ice.

The identification of a feature is based upon the NDVI value it possesses, within the range of -1 to 1 (Holme *et al*., 1987). Table 3.1 provides a general representation of the features which may be identified in an image based upon their respective NDVI values.

Table 3.1 Identification of features within a satellite image based upon their respective NDVI values (Simonetti *et al.*, 2014)

NDVI Value	**Feature**
NDVI < 0	Water Body
0.1 < NDVI < 0.2	Bare Soil
0.2 < NDVI < 0.3	Sparse vegetation cover
0.3 < NDVI < 0.5	Moderate vegetation Cover
NDVI > 0.6-0.8	Dense vegetation cover

The NDVI was calculated for the region between Mahale and Letaba Ranch Weirs utilizing the red and NIR bands of a Landsat 8 image obtained for the 21st June 2015. These values were then used in conjunction with the projects' knowledge of the study area, to identify the density distribution of vegetation and to broadly classify land use. These are represented in Figure 3.1. It should be noted that this classification is a very simplistic representation of the land uses which are present in the study area.

Although Landsat 8 data is provided at a spatial resolution of 30m, classifying land use and land cover at this resolution may be too broad, as it can be difficult to determine the distribution of individual species without detailed *a priori* knowledge on the location and distribution of individual plant species, observed in the satellite image. Furthermore the presence of cloud within Figure 3-1 may have contributed to an incorrect identification of features.

It is therefore recommended that cloud-free imagery at a potentially finer spatial resolution should be incorporated into a more well established land cover classification technique to estimate the distribution of land use and land cover.

The land uses represented in Figure 3-1 were broadly classified into five categories, these include; (i) Water Bodies, (ii) Bare soil, (iii) Sparse vegetation cover consisting of shrubs, thicket, reeds and grassland, (iv) Moderate vegetation cover consisting of shrubs, thicket, reeds, croplands, grassland and trees and (v) Dense vegetation cover consisting of shrubs, thicket, reeds, croplands, grassland and trees.

Each component of the total evaporation process i.e. evaporation of intercepted water, soil water evaporation and transpiration is either directly or indirectly affected by the type, distribution and density of vegetation in a specified area. Therefore, the classification of vegetation species and distribution facilitates an improved understanding of total evaporation estimates and may hold added significance when other factors which influence total evaporation are relatively stable.

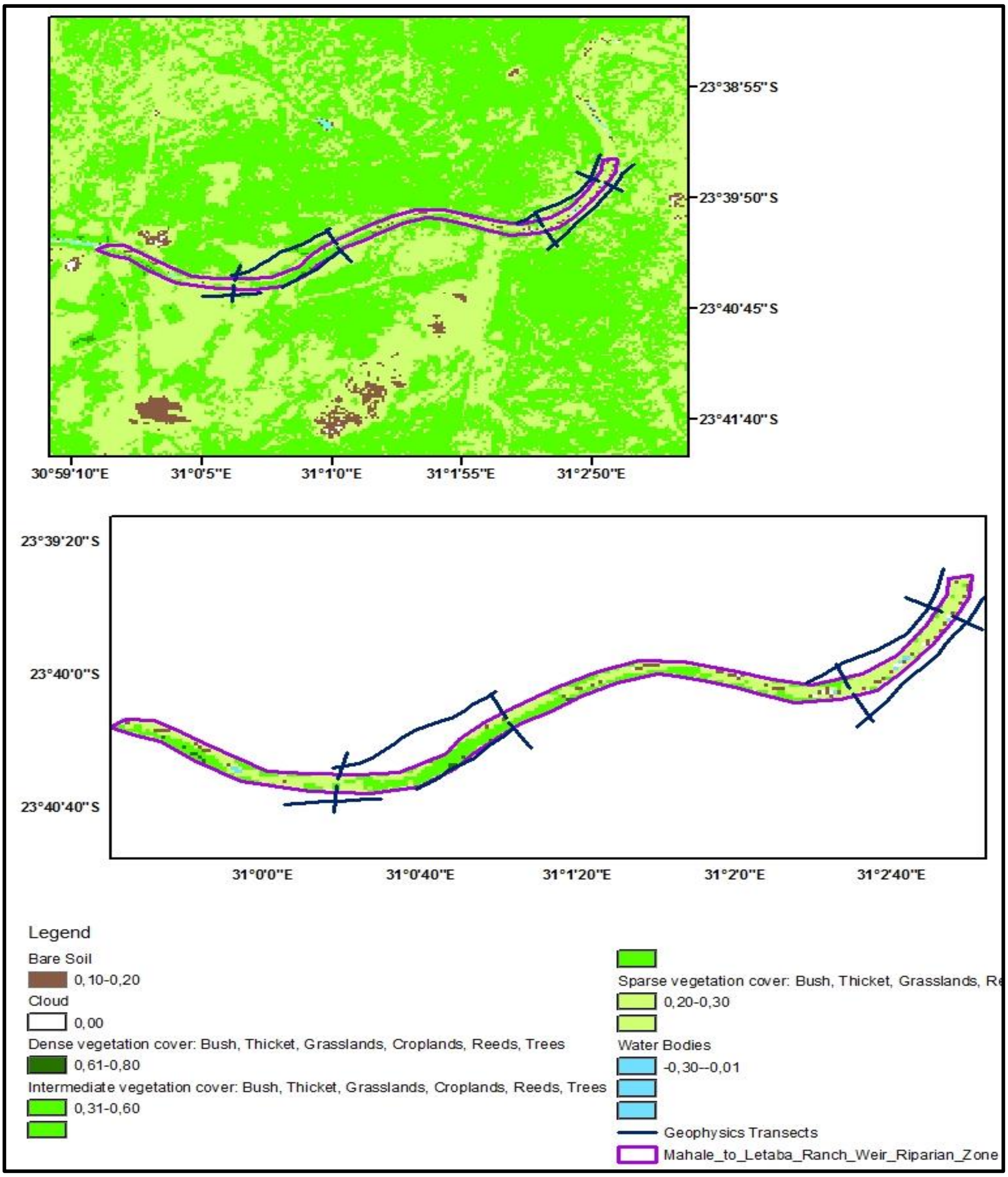

Figure 3-1 An illustration of the distribution of vegetation density and classification of land uses based upon NDVI, for the region between Mahale and Letaba Ranch Weirs on the 21st of June 2015.

4. Surface Energy Balance System (SEBS) analysis

4.1. Determination of river reach Total Evaporation between Mahale and Letaba Ranch using SEBS (Landsat 8)

Landsat 8 images were used as inputs to SEBS to estimate total evaporation. There are two sensors on-board Landsat 8, these are the Operation Land Imager (OLI) and the Thermal Infra-Red Sensor (TIRS). The images are available at a temporal resolution of 16 days, whilst the spatial resolution of the bands varies between 15 m, 30 m or 100 m depending on the sensor. Table 4.1 provides a description of the spatial resolution of each of the bands.

Table 4.1 Landsat 8 OLI and TIRS Spectral Bands

Landsat 8 OLI and TIRS Bands (µm)		
30m Coastal/Aerosol	0.435 - 0.451	Band 1
30m Blue	0.452 - 0.512	Band 2
30m Green	0.513 - 0.590	Band 3
30m Red	0.636 - 0.673	Band 4
30m NIR	0.851 - 0.879	Band 5
30m SWIR-1	1.566 - 1.651	Band 6
100m TIR-1	10.60 - 11.90	Band 10
100m TIR-2	11.50 - 12.51	Band 11
30m SWIR-2	2.107 - 2.294	Band 7
15m Pan	0.503 - 0.676	Band 8
30m Cirrus	1.363 - 1.384	Band 9

The images were selected for the period 28th May 2015 to 07th July 2015. Due to the short study period images which possessed variable cloud coverage over the study site were not excluded. However it should be noted that this could possibly introduce errors to the SEBS total evaporation estimate. It is therefore recommended that for longer study periods, images containing a high percentage of cloud coverage should be excluded and only those which possess little to no cloud cover should be used.

Landsat 8 Bands 2-7 and Bands 10-11 were imported into the Integrated Land and Water Information System (ILWIS), using the Geospatial Data Abstraction Layer (GDAL). The bands which were imported into ILWIS were given as a simplified integer number and therefore had to be converted into reflectances and radiances.

The procedures outlined in USGS (2008) were used to process the bands into a usable format, which could then be used to generate input maps required by SEBS. The corrected reflectance and radiance bands were then used in five processing phases in ILWIS to generate raster maps required as inputs to SEBS, these include; (i) computing the brightness temperature, (ii) land surface albedo computation, (iii) land surface emissivity computation, (iv) NDVI computation and (v) the land surface temperature computation.

Meteorological data inputs collected at the study site; such, as the air temperature, mean daily air temperature, mean daily wind speed, surface pressure and pressure at a reference height were used in conjunction with the above-mentioned satellite-derived raster maps to estimate daily total evaporation based on the algorithm derived by Su (2002). Figure 4-1 to Figure 4-4 illustrate the SEBS total evaporation obtained for specific dates in the period 28th May 2015 to 07th July 2015.

Analysis of the SEBS total evaporation maps and the distribution of vegetation biomass and classification of land use map indicates that areas which were classified as dense vegetation cover and moderately dense vegetation cover were generally associated with higher degrees of total evaporation. Sparse vegetation cover and bare soil was generally associated with lower degrees of total evaporation.

Areas classified as open water did not possess any total evaporation data. This however, was expected as the pre-packaged version of SEBS in ILWIS has rarely been applied and validated for the estimation of open water evaporation (Abdelrady, 2013). In order to estimate open water evaporation using satellite earth observation data, an adaptation of the SEBS model is required (Su *et al.*, 2001).

Although the general trends in the SEBS total evaporation appear to correlate with Figure 3-1, there are various instances in which the need for a more detailed finer spatial resolution land use classification is highlighted. For example, in some areas classified as moderately dense vegetation cover, the SEBS total evaporation exceeds that of areas classified as dense vegetation cover.

This can be expected as classifying an area according to density and not according to the actual cover present can be misleading. If there is a moderate coverage of tree species, a higher total evaporation can be expected as opposed to an area which has a dense coverage of grasslands, therefore although Figure 3-1 can assist with understanding the general trends in the SEBS total evaporation, a more detailed representation will be required to better understand the vegetation species specific contribution to total evaporation.

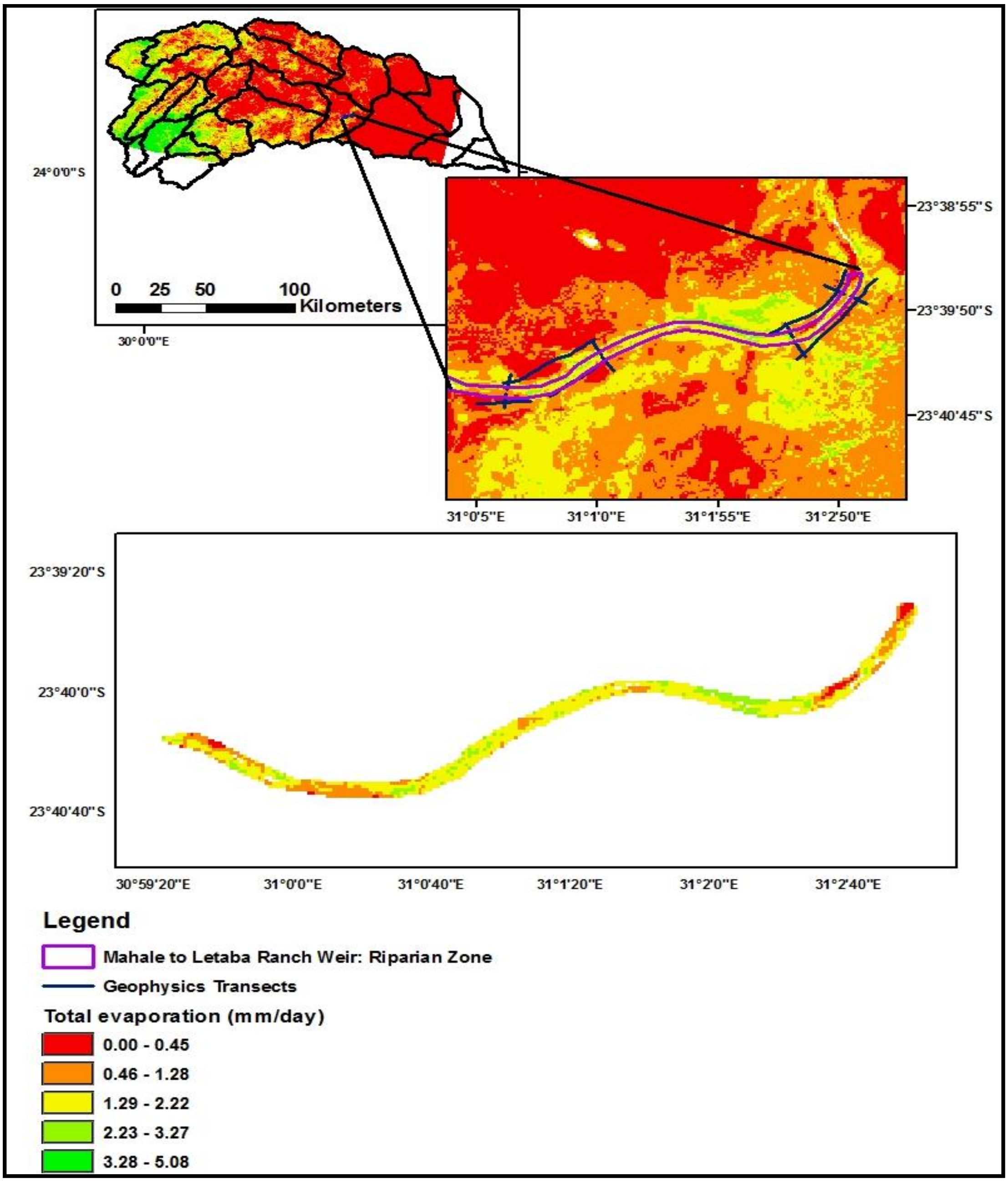

Figure 4-1 Variation of SEBS total evaporation between the Mahale and Letaba weirs for the 20th May 2015, during clear sky conditions.

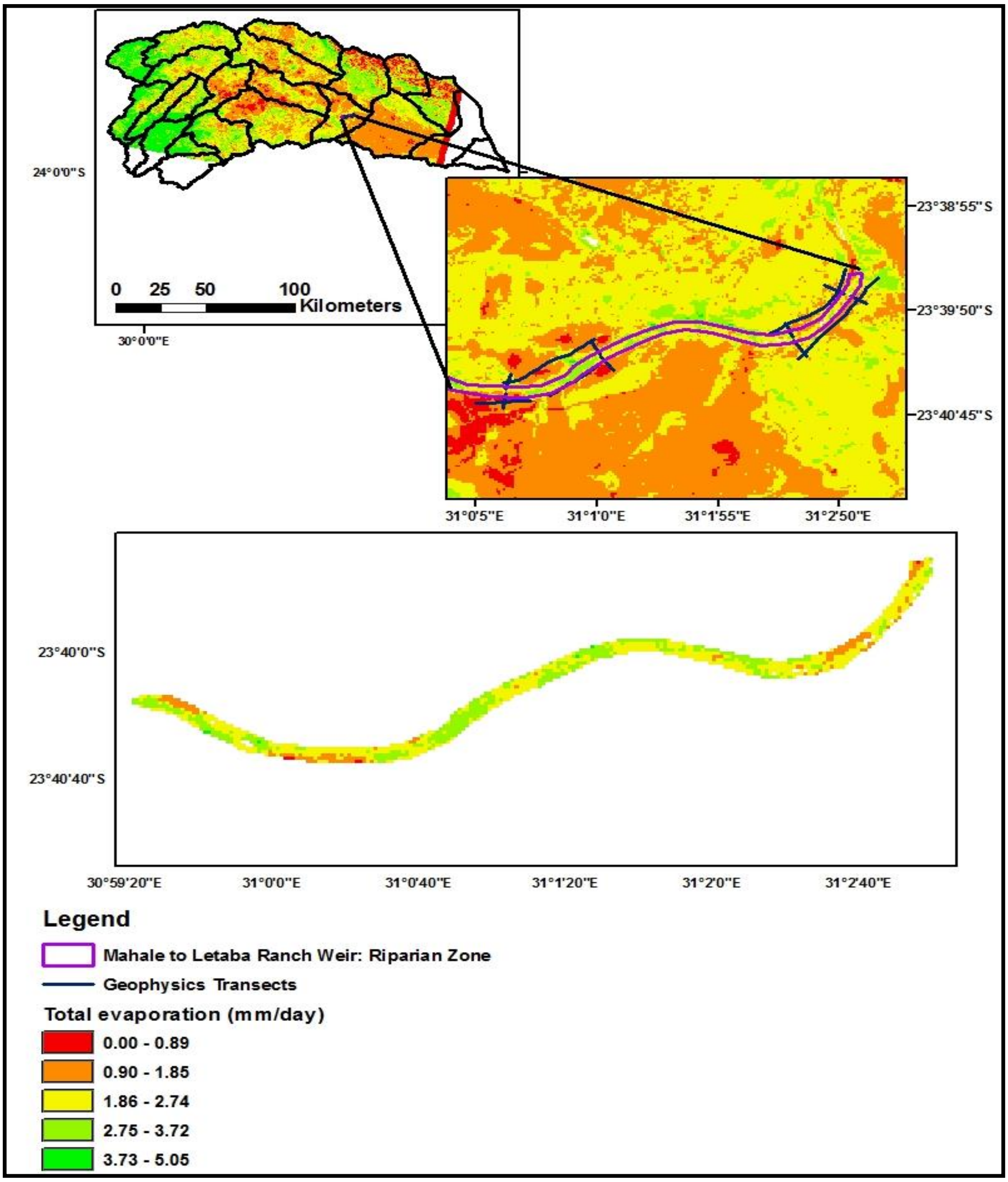

Figure 4-2 Variation of SEBS total evaporation for cloud free conditions, between the Mahale and Letaba weirs for the 05th June 2015.

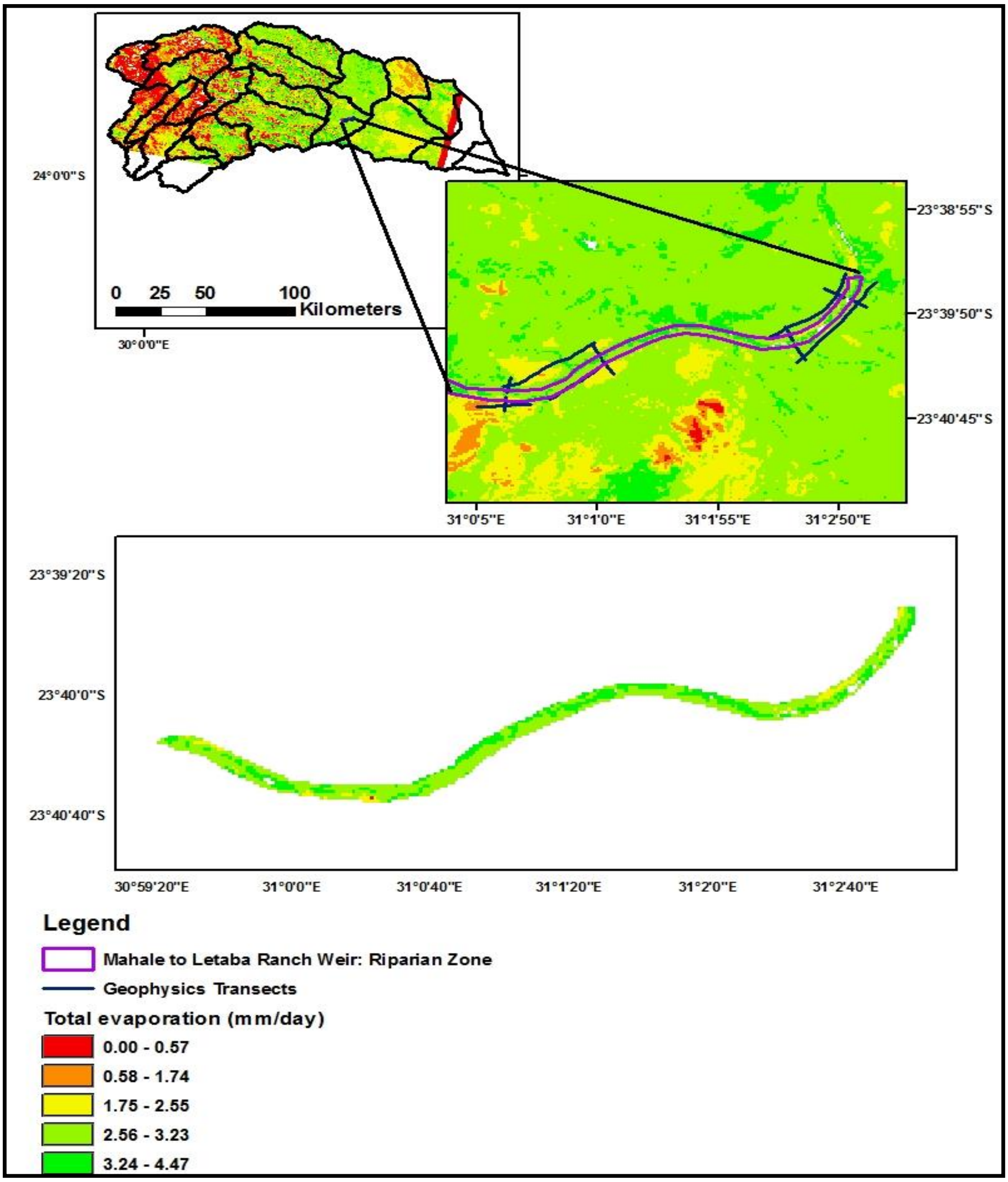

Figure 4-3 Variation of SEBS total evaporation for cloud free conditions between the Mahale and Letaba weirs for the 21st June 2015

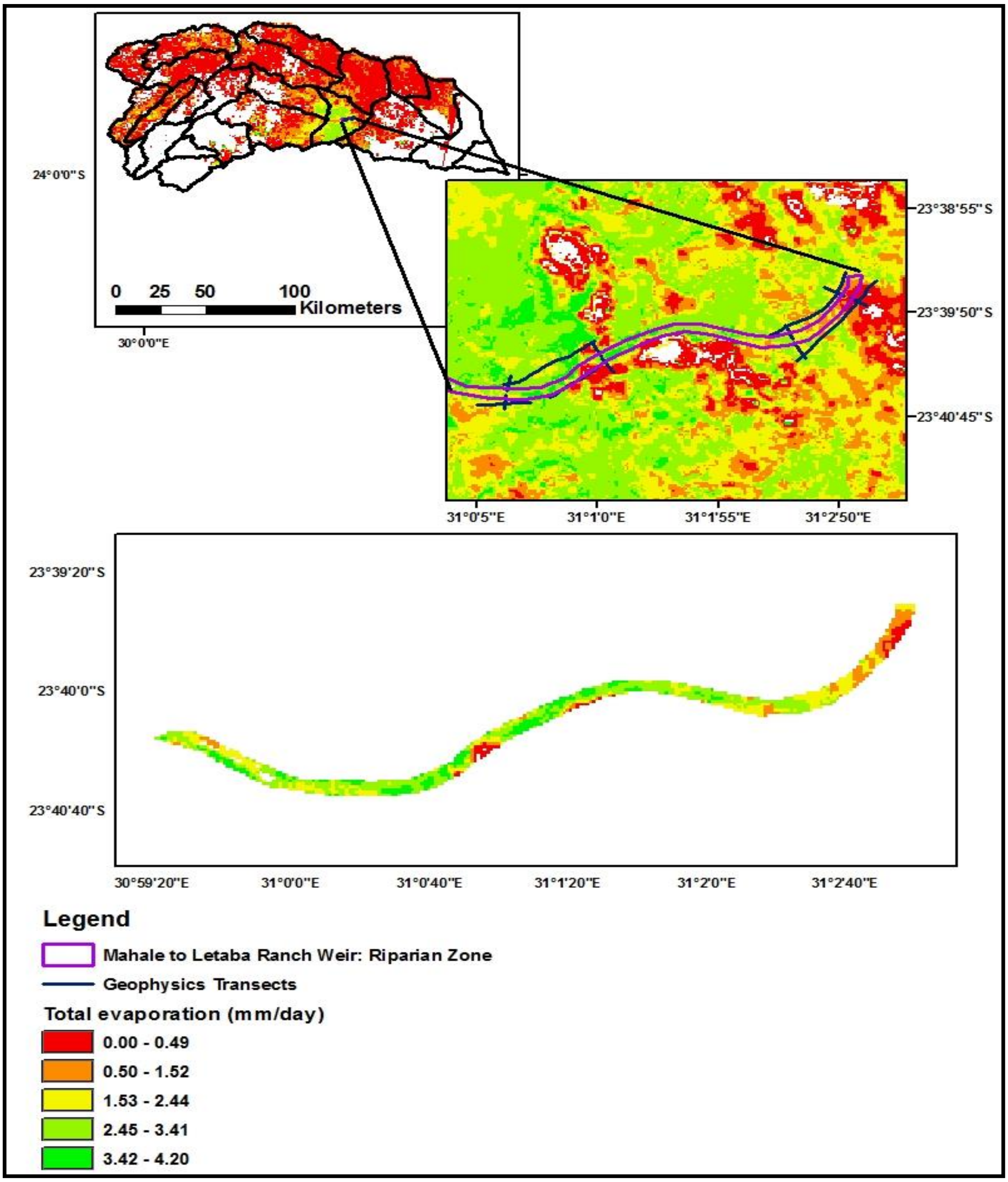

Figure 4-4 Variation of SEBS total evaporation for variable cloud coverage, between the Mahale and Letaba weirs for the 07th July 2015

An additional observation was the SEBS total evaporation associated with areas classified as bare soils. Generally the total evaporation observed in these areas was found to be low. However in some instances these values were in the same order of magnitude of the total evaporation associated with moderate and dense vegetation coverage. These bare soil regions were generally found to be situated within or close to the river.

The water table in this region is expected to be closer to the surface as compared to areas further away from the river system, as a result water can evaporate relatively easily from the soil surface, hence the higher rates of total evaporation.

Table 4.2 provides a summary of the SEBS total evaporation data obtained for specific dates in the period 28th May 2015 to 07th July 2015. The mean total evaporation between the Mahale and Letaba Ranch Weirs for the selected dates, indicates that on average there is 2.44 mm of daily total evaporation along the transect.

Table 4.2 Summary of SEBS (Landsat8) total evaporation statistics for selected days, along the transect between Mahale and Letaba Ranch weirs in mm/day.

	Date	MIN	MAX	RANGE	MEAN	VAR	STD
Mahale to Letaba Ranch Transect	20-May-15	0.00*	3.19	3.19	1.62	0.33	0.58
	5-Jun-15	0.47	4.03	3.55	2.46	0.28	0.53
	21-Jun-15	1.76	3.77	2.01	3.07	0.15	0.39
	7-Jul-15	0.00*	4.29	5.05	2.50	0.85	0.92

* Some cloud contamination in the images resulted in areas being classified as possessing a total evaporation value of 0 mm when the statistical analysis was performed.

5. Eddy Covariance ET

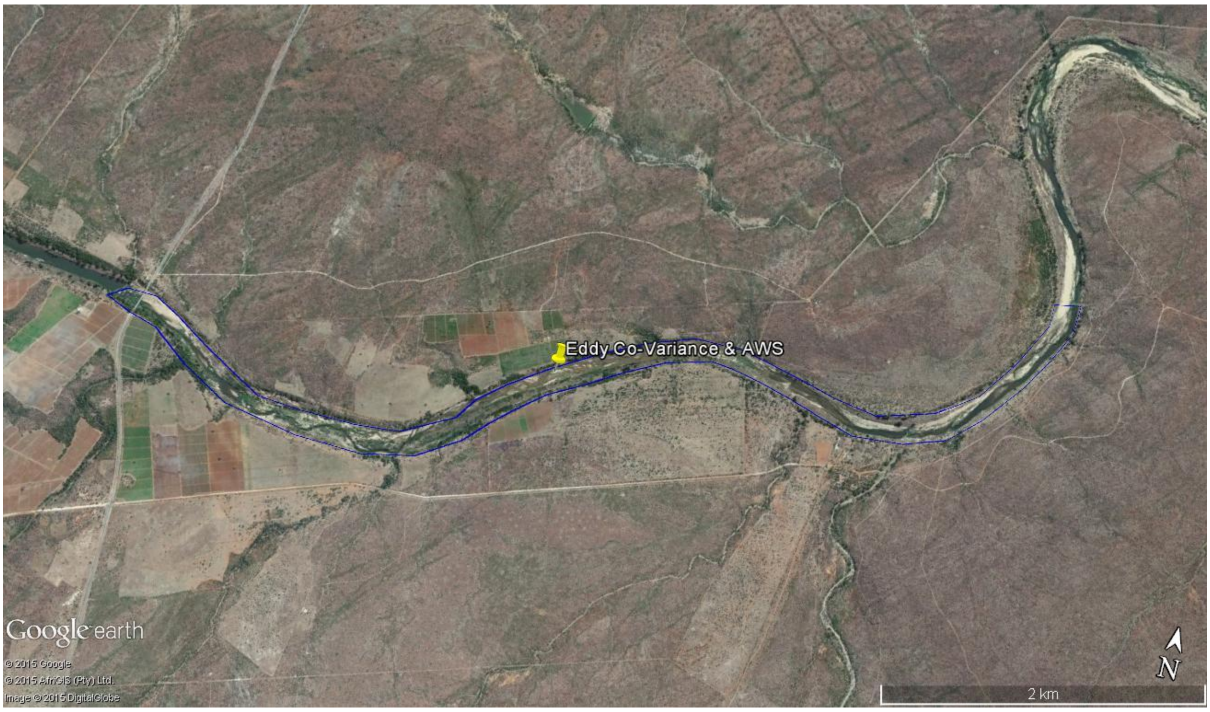

Figure 5-1 Location of Eddy covariance system, energy balance sensors and Automatic Weather Station between Mahale and Letaba Ranch for the period May – July 2015

A complete Automatic Weather Station (AWS), attached with energy balance sensors and a sonic anemometer was installed within the river channel along the transect between Mahale and Letaba Ranch Weirs to estimate total evaporation using the eddy covariance technique (Figure 5-1). The energy balance sensors consisted of soil heat flux plates and net radiometers to determine the net radiation and soil heat flux components of the shortened energy balance equation. Concurrent estimates of sensible heat flux were derived using data captured by the sonic anemometer and ancillary meteorological data. The net radiation, soil heat flux and sensible heat flux were used for the estimation of Latent heat flux at various time steps, as a residual of the shortened energy balance equation.

The measurements of the various components of the shortened energy balance, with noticeably low net radiation, obtained for the period 18^{th} June to 14^{th} July 2015 are represented graphically in **Figure 5-2**. The low net radiation which is observed can be attributed to the portioning of energy to the soil heat flux.

Soil heat flux values during this period were noticeably high, further highlighting the need to accurately quantify the coverage between the dominant land covers present in the system *viz.* sand, phragmites and water. Figure 5-3 illustrates the comparison of soil heat flux (for different land use components) to net radiation. The trends identified in Figure 5-3 further serve to confirm the prominent role which the soil heat flux plays in this environment.

Total evaporation values were estimated by weighting the contribution of the components of the energy balance according to their coverage across the area in which the system was situated. The weighting was done as follows; (i) 20% water contribution, (ii) 40% for bare soil and (iii) 40% for phragmites. The preliminary estimates of total evaporation, utilizing the eddy covariance technique are illustrated in Figure 5-4. The large percentage contribution of bare soil to the total evaporation estimate strongly influences the occurrence of the low total evaporation which is observed. This is largely due to the high reflectivity associated with the bare soil.

The eddy covariance system was installed in the inner channel of the river system. Therefore the preliminary total evaporation results are only representative of one typical vegetation, water and sand composition. Future measurements will involve moving the system along different positions across the transect, to understand the contribution of the channel fringe vegetation to the total evaporation estimate.

The preliminary findings are expected to be improved upon, through supplementary investigations, which will be conducted to quantify all the contributing processes of total evaporation i.e. soil water evaporation, transpiration, and open water evaporation. These measurements and a detailed vegetation/land use composition analysis will be used to up-scale the measurements of total evaporation for the river reach, which can then be compared to the satellite-derived estimates of total evaporation.

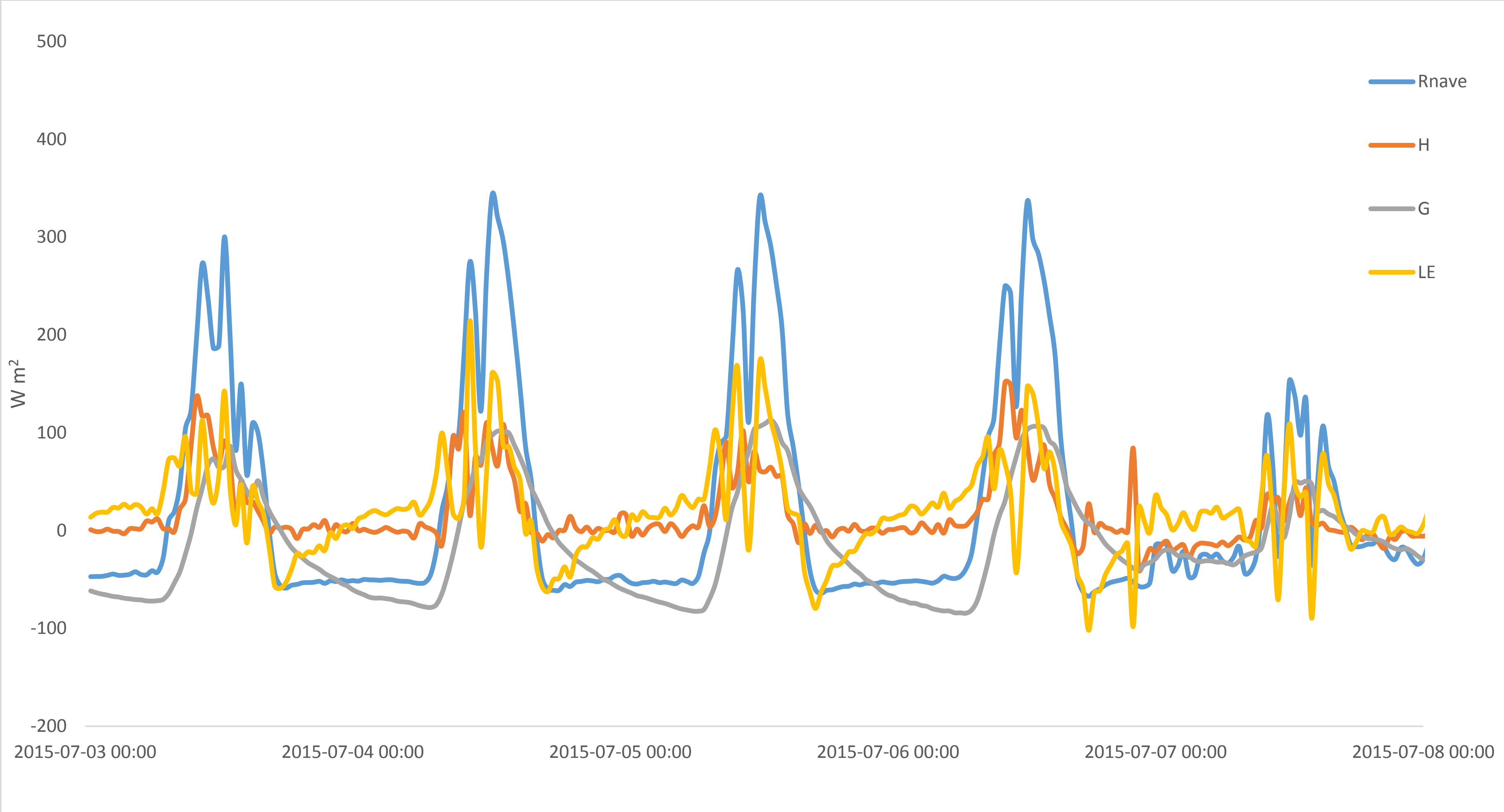

Figure 5-2 Components of the shortened energy balance measured at a point within the river channel along the transect between Mahale and Letaba Ranch Weirs

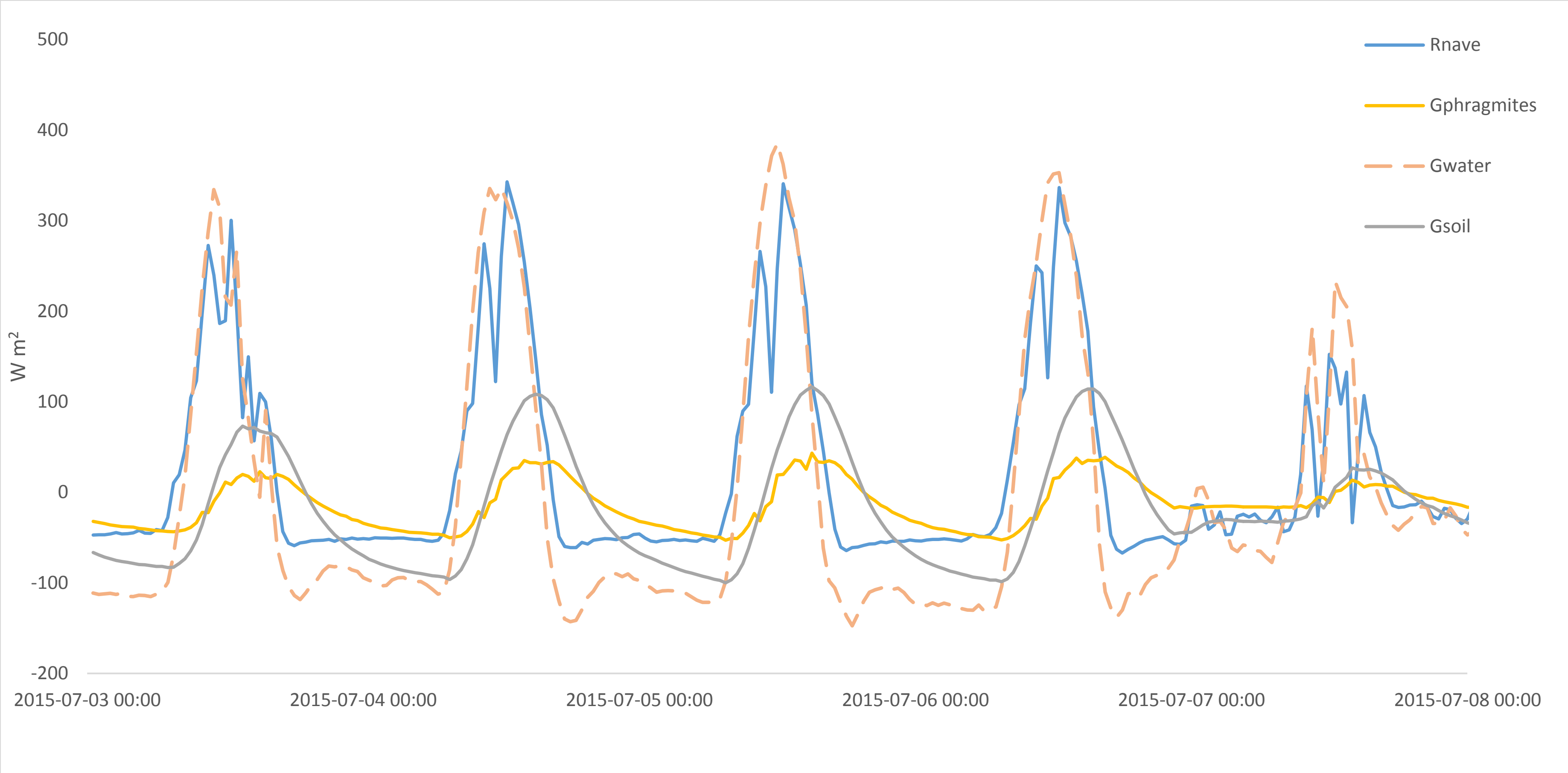

Figure 5-3 Soil heat flux comparisons (for different land use components) to net radiation at a point within the river channel along the transect between Mahale and Letaba Ranch Weirs

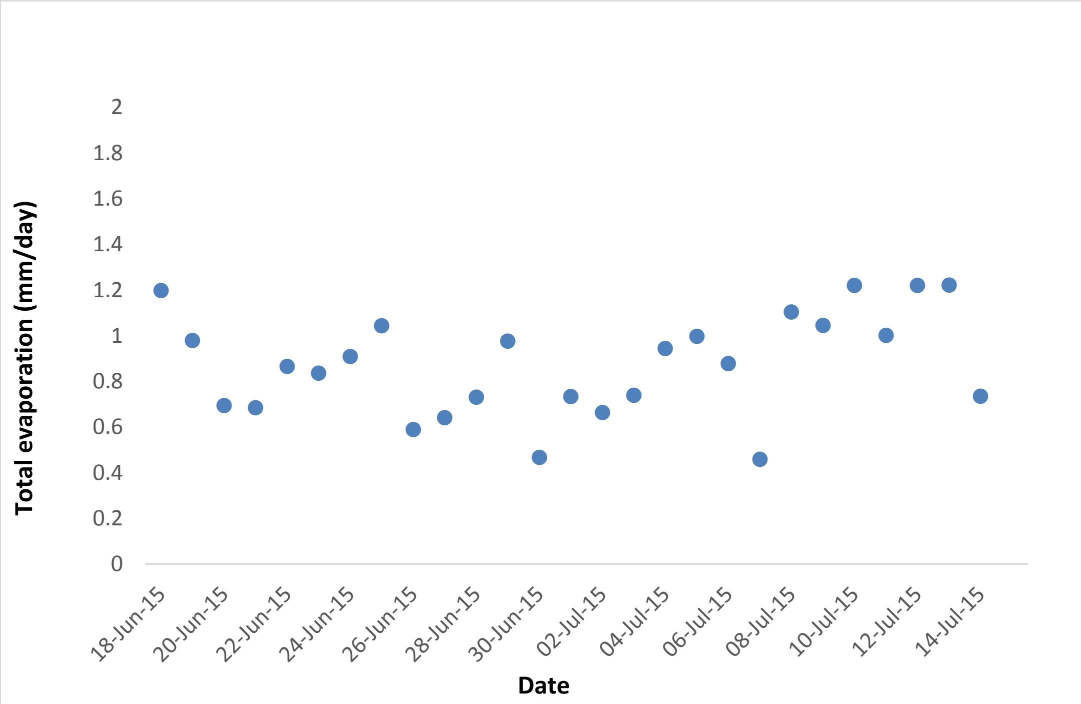

Figure 5-4 Preliminary estimates of total evaporation utilizing the eddy covariance technique at a point within the river channel along the transect between Mahale and Letaba Ranch Weirs (see Appendix II)

6. Mass Balance Approach to Infer ET and GW-SW processes

6.1. Introduction

The purpose of this chapter is to present the first order attempt to quantify transmission losses between two weirs at the study site; these are the upstream Mahale weir and downstream Letaba Ranch weir (Figure 6-1). It is important to note that these data here are preliminary and these methods will see continuous improvements during the course of the study based on revising the weir ratings, groundwater borehole characterisation, and continuous hydro-census (river abstractions and borehole pumping).

The principle of this method is to determine the difference in flow between the two weirs, taking account of any artificial abstractions from or discharges to the resource, and then attributing the difference to either a loss or gain of water to the system. This required first downloading the flow data at Letaba Ranch[1] and then determining the flow at Mahale weir as this is a defunct weir. The Mahale weir required the stage to be determined by a Solinst™ Junior Level logger installed on the upstream side of the weir wall and a hydraulic rating of the weir and upstream flow conducted following the methods described in Dingman (2009).

Figure 6-1 Location of the Mahale Weir (B8H007) and Letaba Ranch Weirs (B8H008) which are used in the mass balance approach to determine Transmission Losses at the study site.

For the purposes of this report data is presented following the installation of the Eddy Co-variance system (Chapter 5) with a focus on the true low flow period in June-July 2015. Flows at Mahale weir are then limited to its low flow discharge pipes (rather than also over

[1] http://www.dwaf.gov.za/Hydrology/RTGraphImage.aspx?Station=B8H008FW&Type=Flow&Rain=Y

topping the weir whose rating is still to be precisely determined at time of writing). Calculation of the low flow values are presented in Table 6.1 and the differences in flow between the two gauges in Figure 6-2. What is noticeable from this is that there is a slight gain in flow from upstream to downstream suggesting a sustained groundwater inflow to the main channel (see Chapter 8) assuming no other discharge to the resources. *Updating the Mahale weir rating and calculating the routing lag time between the two weirs will confirm this in subsequent deliverables*.

Table 6.1 Low flow discharges determined at Mahale Weir

Flow pipes (m/s)		Pipe diameter (m)	Discharge (m^3/s)	Total Discharge (m^3/s)
Pipe 1	3.4	0.3	0.240	0.502
Pipe 2	3.7	0.3	0.261	

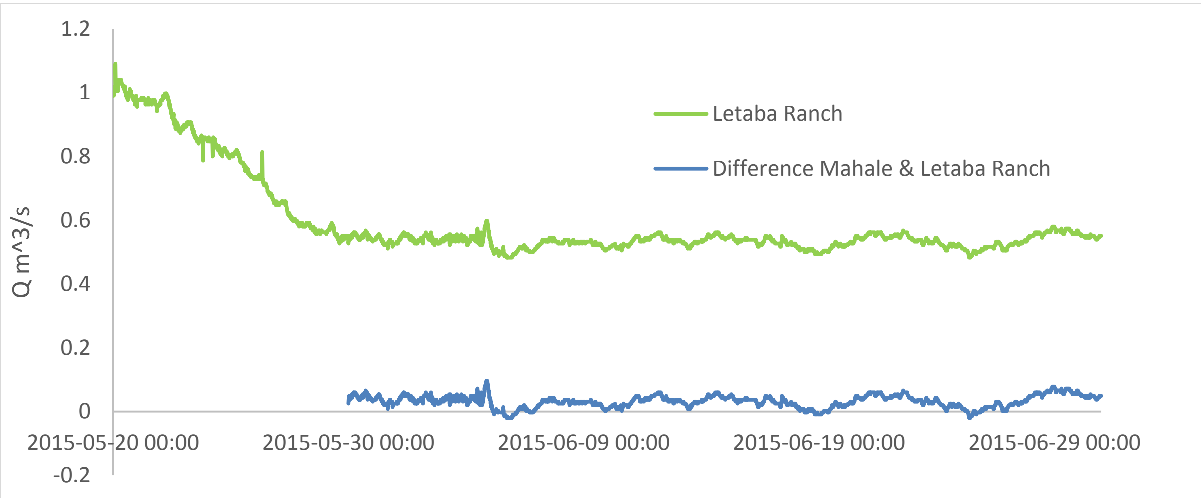

Figure 6-2 Low flows at the Letaba Transmission Losses site with differences between the upstream and downstream gauges (note stable low flows at Letaba Ranch from end of May 2015).

6.2. Base flow ET estimation

Based on the assumption of stable low flows as depicted in the previous section a subset of this data was used to estimate the daily total evaporation losses from the river reach between the two weirs based on the method described by Meyboom (1965, as cited in Gribovski et al, 2010). This focused on data between 27 June and 17 July 2015. This method depicted in Figure 6-3 calculates the water volume of streamflow as used by ET as a difference between the maximum streamflow rates in a 24-hour period (i.e. Max Stream) and the actual diurnal stream flow hydrograph.

In this the instantaneous total evaporation losses are calculated as the difference between the interpolated hydrograph between the Max Stream points (Q_{max}) and the observed hydrograph (Q). The daily total evaporation losses are then simply calculated as the product of these values over time (t) to give a daily volume (m^3), which divided by an inferred riparian zone area (A which is 1 702192 m^2, see riparian zone clip in Chapter 4), gives the total evaporative flux (ETa) from the river reach.

$$ETa = \frac{\sum(Q_{max} - Q)\Delta t}{A}$$

Equation 6-1

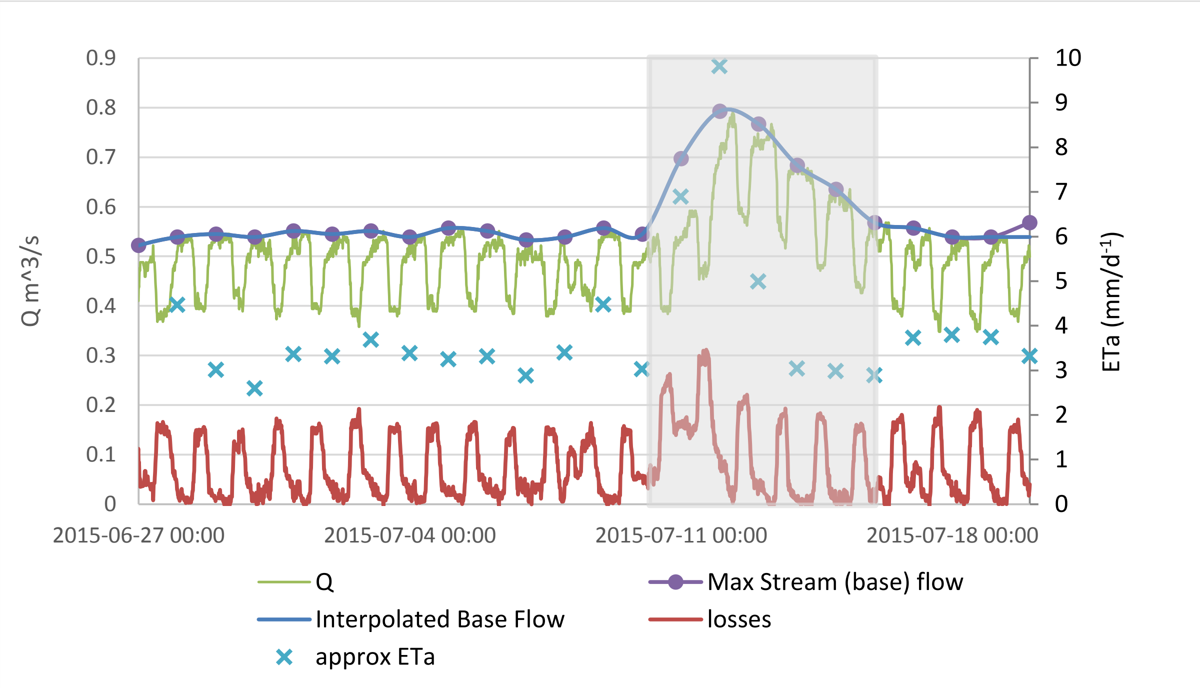

Figure 6-3 Flows at Letaba Ranch (B8H008) end of June to mid July 2015 with ET estimated according the method of Meyboom (1965) (Greyed-out area represents data over a weekend where flows increased from upstream likely due to reduced irrigation abstractions)

This method then also allows one to estimate on a first order basis the groundwater contributions to stream discharge, or otherwise losses from the stream to groundwater by simply deducting the known stable flow from Mahale weir (Table 6.1) from the interpolated Qmax at Letaba Ranch weir (Figure 6-3). The estimated groundwater contributions to the river reach between Mahale weir and Letaba Ranch are depicted in Figure 6-4, showing typically a positive time-series, suggesting that at the time of analysis (the start of the low flow season) in 2015 that this reach of the Groot Letaba river is receiving groundwater inflows from the aquifer in the surrounding landscape.

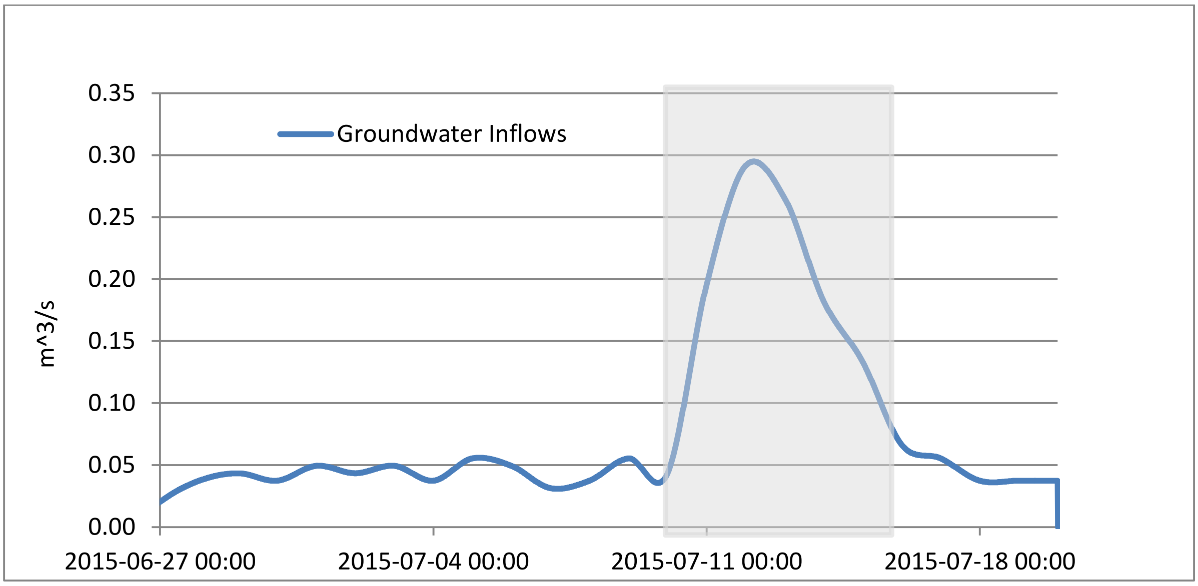

Figure 6-4 Estimated groundwater contributions to the river reach between the Mahale and Letaba ranch weirs (Greyed-out area represents data over a weekend where flows increased from upstream likely due to reduced irrigation abstractions)

6.3. Riparian zone ET from borehole data

Using one of the recently drilled riparian zone boreholes which had equilibrated and been installed with a Solinst™ Level logger it was possible to use the White (1932) method to estimate ETa at a point. This method will be refined during the course of the study and is presented here as an initial estimate of ET at the point. The White Method assumes that during the night ET becomes negligible especially during the predawn hours. There is then a further assumption that the rate of the observed groundwater-level increase is directly proportional to the rate groundwater is supplied to the riparian zone from the aquifer.

This method is calculated as (see Figure 6-5):

$$ET = S_y\,(24r \pm s) \qquad \text{Equation 6-2}$$

Where S_y is the specific yield of the aquifer; the slope, r is derived from the tangential line drawn to the groundwater level curve in these sections (from midnight to 4 a.m.), the product of which represents the rate of water supply to a unit area. 24r is then calculated by extending the tangential line over 24 hours and subtracting the difference in groundwater levels. This then allows one to estimate of the total water supply to the unit area over a day, which must be modified by the starting and ending difference in actual observed water levels, s.

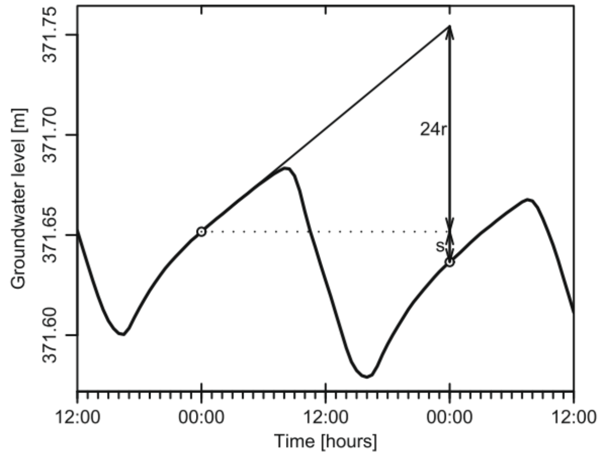

Figure 6-5 Basic principle of the White Method (after Gribovski et al, 2010)

In the example calculated at LR005A (Figure 6-6) a clear diurnal change in groundwater level is observed during June 2015 lending itself nicely to test the White method. The ETa is calculated here using preliminary data[2], which includes an assumed S_y of 0.09 for granitoid rocks (Heath, 1993).

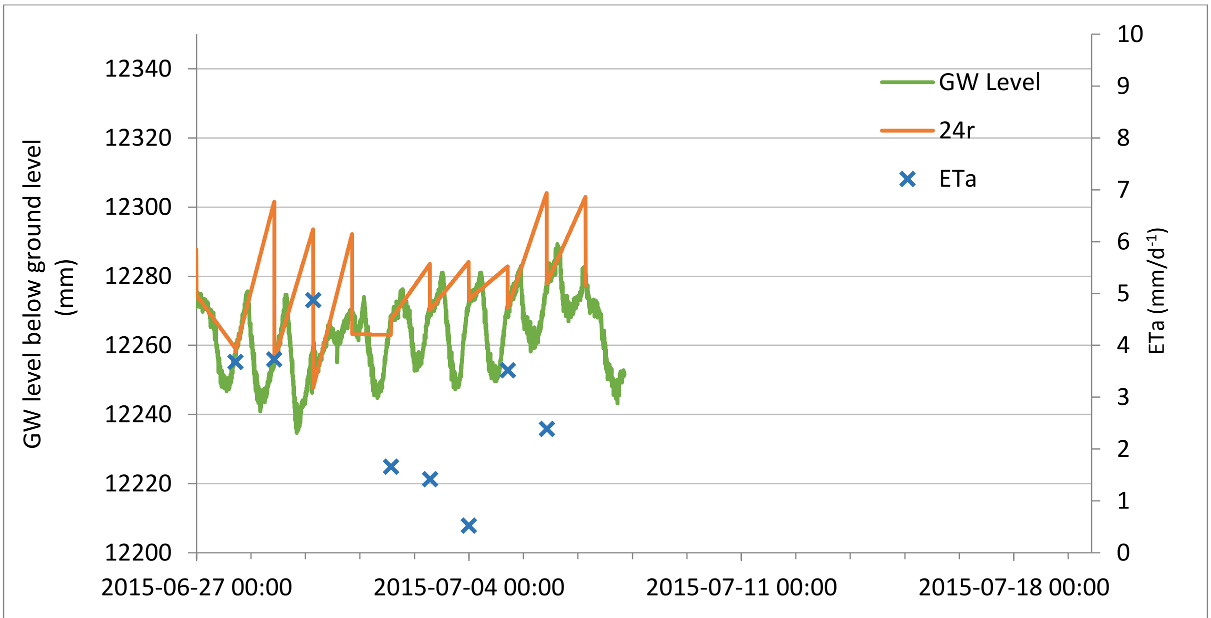

Figure 6-6 ETa estimate using the White (1932) Method at borehole LF005A (see Figure 7-2)

[2] Until hydraulic characterisation of the boreholes has been completed

7. Site borehole drilling report

The riparian groundwater piezometer network drilling commenced in May 2015 after some unfortunate delays at the Limpopo drilling office of the Department of Water & Sanitation. To date 11 holes of 26 have been drilled according the piezometric design depicted in Figure 7-1 to differentiate groundwater hydrodynamics in the unconsolidated and hard rock zones. The locations of these boreholes are shown in Figure 7-2, with the initial drilling logs for the completed boreholes captured in the subsequent pages of this chapter (full details in Appendix III).

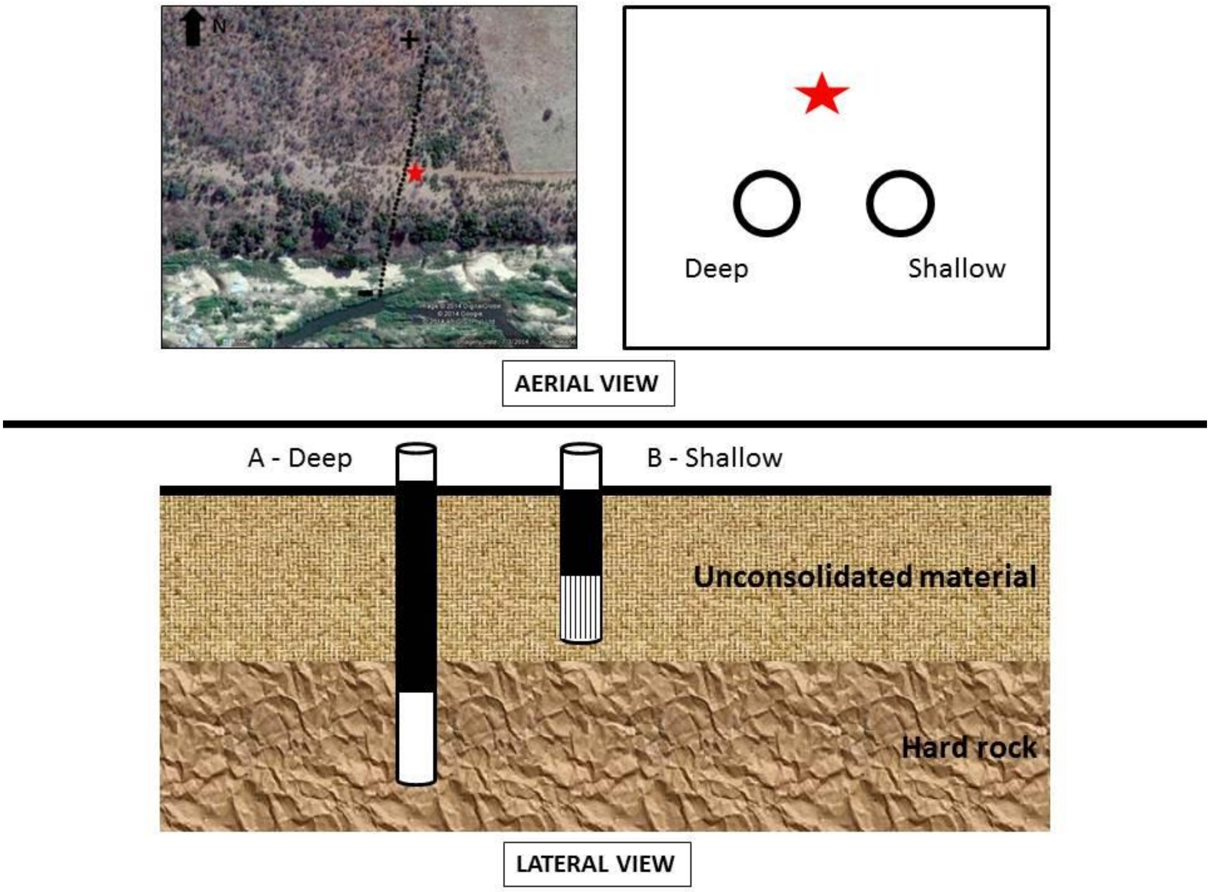

Figure 7-1 Piezometric Borehole network design at the study site.

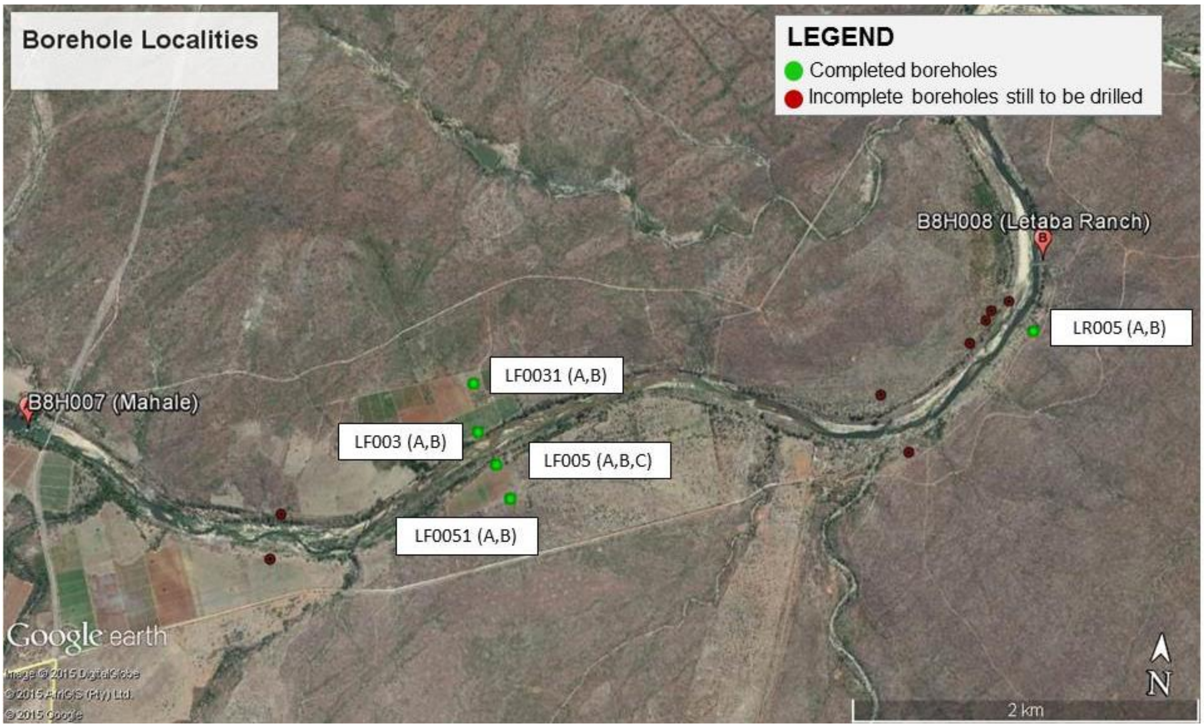

Figure 7-2 Completed and planned piezometric boreholes locations at the study site

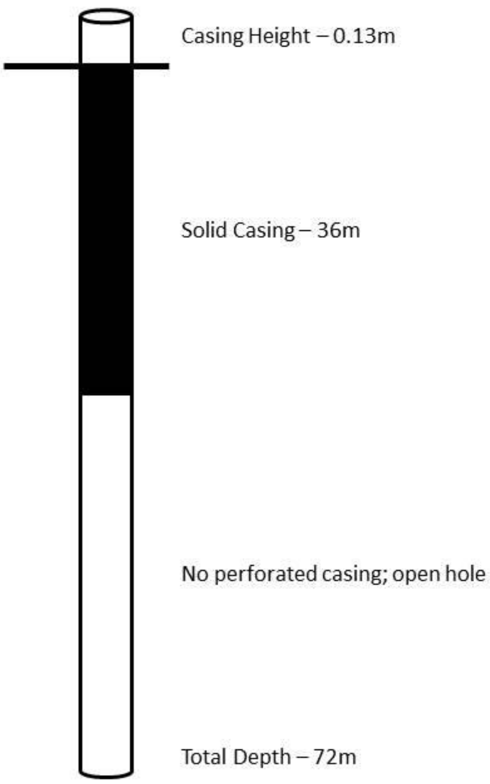

BOREHOLE NAME: LF003A

Date Completed:	25/05/2015
GPS Co-ordinates:	S 23.66953° E 31.01664°
Site:	Maliesa's Farm
Borehole Depth:	72m
Water Strike:	15m
Estimated Yield:	0.3 l/s

Date	Observed Water Levels (m)
11/06/2015	10.97
15/06/2015	10.96
10/07/2015	10.58
21/07/2015	10.95

Date	EC	Temp
21/07/2015	1740 uS/cm	26.1 °C

NOTES: Generally, static water level of about 10.96, except for 10/07/2015 when water level was 10.58m.

BOREHOLE NAME: LF0031A

Date Completed:	25/05/2015
GPS Co-ordinates:	S 23.66703° E 31.01624°
Site:	Maliesa's Farm
Borehole Depth:	30m
Water Strike:	21m
Estimated Yield:	3 l/s

Date	Observed Water Levels (m)
11/06/2015	12.95
15/06/2015	12.91
10/07/2015	12.96
21/07/2015	12.97

Date	EC	Temp
10/07/2015	1589 uS/cm	26 °C
21/07/2015	1518 uS/cm	26.1 °C

NOTES: Boreholes to be repaired in due time.
Sited without the use of geophysics; based purely on visual evidence of a structure (change in soils)

BOREHOLE NAME: LF003B

Date Completed:	01/06/2015
GPS Co-ordinates:	S 23.66953° E 31.01664°
Site:	Maliesa's Farm
Borehole Depth:	20m
Water Strike:	12m
Estimated Yield:	< 0.5 l/s

Date	Observed Water Levels (m)
11/06/2015	10.76
15/06/2015	10.75
10/07/2015	10.85
21/07/2015	10.83

Date	EC	Temp
10/07/2015	1614 uS/cm	26 °C
21/07/2015	1446 uS/cm	26.2 °C

NOTES: Log analysis shows iron-staining on chips collected at 12m where there was a water strike. Evidence of water located at 12m

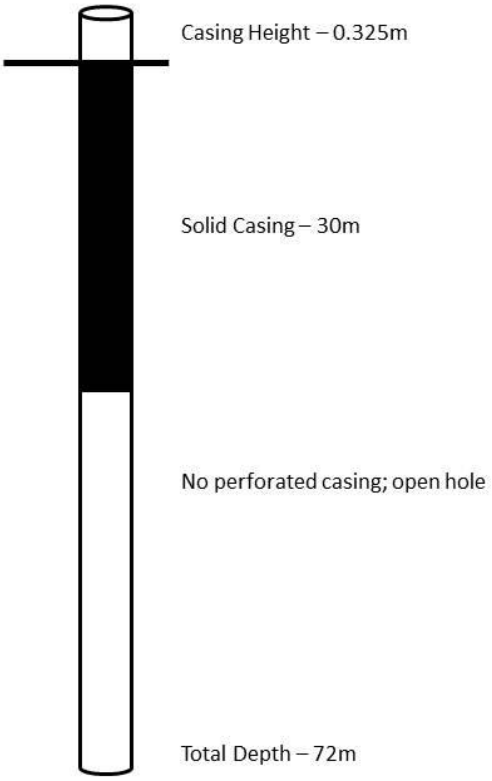

BOREHOLE NAME: LF005A

Date Completed:	04/06/2015
Date Corrected:	21/07/2015
GPS Co-ordinates:	S 23.671324° E 31.017835°
Site:	Bongele's Farm
Borehole Depth:	72m
Water Strike:	32m
Estimated Yield:	0.5 l/s (measured)

Date	Observed Water Levels (m)
11/06/2015	12.33
15/06/2015	12.33
10/07/2015	12.34
15/07/2015	12.35

Date	EC	Temp
15/07/2015	2800 uS/cm	26.1 °C

NOTES: Initial solid casing depth was too shallow, thus was re-cased to 30m (21/07/2015). Found iron-stained calcrete (chalk) at 12-18m during the casing repair.

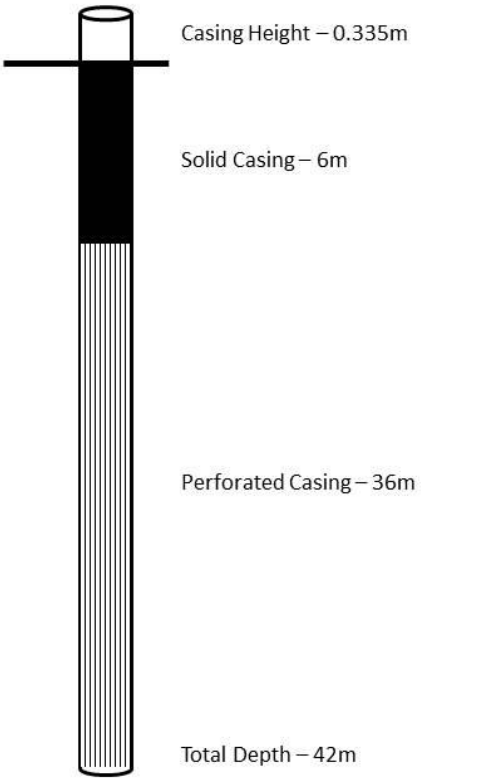

BOREHOLE NAME: LF005B

Date Completed:	09/06/2015
GPS Co-ordinates:	S 23.671324° E 31.017835°
Site:	Bongele's Farm
Borehole Depth:	42m
Water Strike:	13m
Estimated Yield:	< 0.5 l/s

Date	Observed Water Levels (m)
11/06/2015	18.34 (recovering)
15/06/2015	12.15
10/07/2015	12.12
21/07/2015	12.21(repair to nearby borehole)

Date	EC	Temp
10/07/2015	2963 uS/cm	26.1 °C
21/07/2015	3354 uS/cm	26.2 °C

NOTES: This borehole is too deep and drilled beyond the unconsolidated material, therefore a shallower 18m borehole was drilled alongside LF005A and LF005B (21/07/2015).

BOREHOLE NAME: LF0051A

Date Completed:	11/06/2015
Date Corrected:	13/07/2015
GPS Co-ordinates:	S 23.67303° E 31.01884°
Site:	Bongele's Farm
Borehole Depth:	54m
Water Strike:	25m & 40m
Estimated Yield:	1.5 l/s

Date	Observed Water Levels (m)
15/06/2015	14.29
10/07/2015	14.22
21/07/2015	15.05 (new, higher casing)

Date	EC	Temp
21/07/2015	1446 uS/cm	27.2 °C

NOTES: Originally, this borehole was cased only 6m with solid casing. On 13/07/2015, solid casing was extended to a depth of 36m. Casing is now higher than before, and hole was blowned, thus water levels are deeper than before.

BOREHOLE NAME: LF0051B

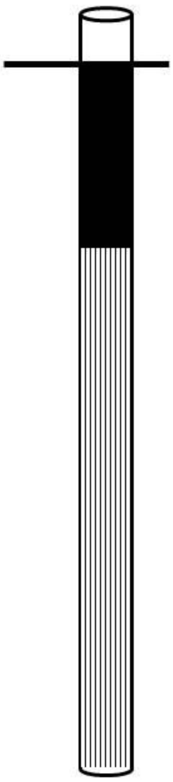

Date Completed:	25/06/2015
GPS Co-ordinates:	S 23.67303° E 31.01884°
Site:	Bongele's Farm
Borehole Depth:	30m
Water Strike:	16m
Estimated Yield:	1 l/s

Date	Observed Water Levels (m)
10/07/2015	14.26
21/07/2015	15.31 (repair to nearby borehole)

Date	EC	Temp
21/07/2015	1393 uS/cm	27.2 °C

NOTES:Deeper water level measured on 21/07/2015 due to repair to nearby LF0051A and borehole blown.

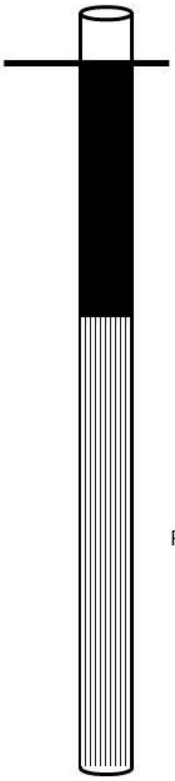

BOREHOLE NAME: LF0031B

Date Completed:	26/06/2015
GPS Co-ordinates:	S 23.66703° E 31.01624°
Site:	Maliesa's Farm
Borehole Depth:	20m
Water Strike:	19m
Estimated Yield:	1 l/s

Date	Observed Water Levels (m)
10/07/2015	12.68
21/07/2015	12.68

Date	EC	Temp
10/07/2015	2897 uS/cm	26.1 °C
21/07/2015	2535 uS/cm	26.1 °C

NOTES: Boreholes to be repaired in due time.
Sited without the use of geophysics; based purely on visual evidence of a structure (change in soils)

BOREHOLE NAME: LR005A

Date Completed:	09/07/2015
GPS Co-ordinates:	S 23.66224° E 31.04954°
Site:	Letaba Ranch
Borehole Depth:	60m
Water Strike:	25m; 38m; 50m
Estimated Yield:	5.7 l/s (measured)

Date	Observed Water Levels (m)
21/07/2015	8.95

Date	EC	Temp
21/07/2015	1740 uS/cm	27.1 °C

NOTES: Sited without the use of geophysics; based purely on visual evidence of a structure (change in soils)

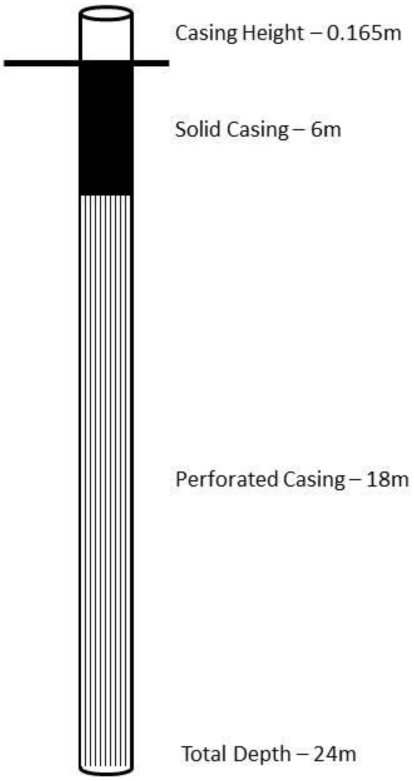

BOREHOLE NAME: LR005B

Date Completed:	13/07/2015
GPS Co-ordinates:	S 23.66222° E 31.04958°
Site:	Letaba Ranch
Borehole Depth:	24m
Water Strike:	19m
Estimated Yield:	1.8 l/s (measured)

Date	Observed Water Levels (m)
21/07/2015	8.94

Date	EC	Temp
21/07/2015	1580 uS/cm	27.1 °C

NOTES: Similar structures to LR005A but more water between 18-24m. Most soil at 9m and 13-15m.

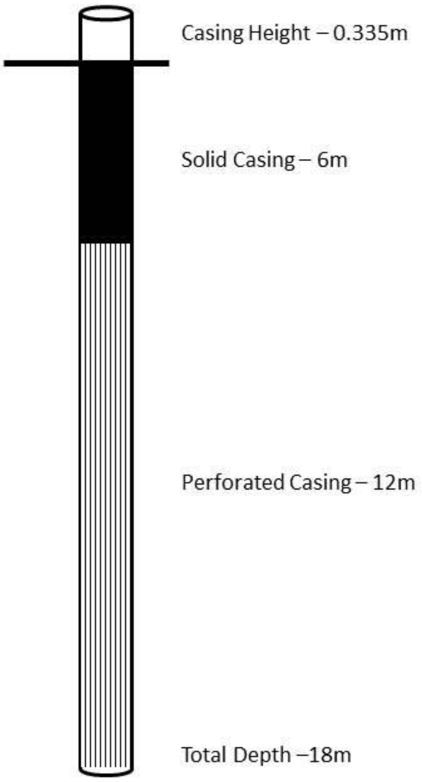

BOREHOLE NAME: LF005B

Date Completed:	14/07/2015
GPS Co-ordinates:	S 23.671324° E 31.017835°
Site:	Bongele's Farm
Borehole Depth:	18m
Water Strike:	13m
Estimated Yield:	0.5 l/s (measured)

Date	Observed Water Levels (m)
21/07/2015	10.97

Date	EC	Temp
21/07/2015	3074 uS/cm	24.9 °C

NOTES: The initial *shallow* borehole was too deep (42m) and drilled beyond the unconsolidated material, therefore this shallower 18m borehole was drilled alongside LF005A and LF005B.

8. Update of the Site Conceptual Model

In addition to the data presented in previous chapters a number of other activities have taken place in order to continually refine the conceptual model for the study site between Mahale weir and Letaba Ranch. These are outlined in the following chapter with brief descriptions and interpretations used to augment our understanding of the site from a geohydrological perspective.

8.1. Magnetic Survey and Updated Interpretation of Geophysics Surveys

8.1.1. Magnetic Surveys

Magnetic surveys are applied in many fields, such as geological mapping and geohydrological surveys. During a field campaign conducted in June 2015, magnetic surveys were used to characterise and confirm the presence of structural intrusions (or magnetic dykes) along the Letaba River. Geophysics transects conducted in 2014 using Electrical Resistivity Tomography (ERT) were resurveyed using a Geotron Proton Magnetometer (G5 Model) (Figure 8-1). The magnetic survey data was coupled and overlaid with the geophysics survey data in order to verify the presence of possible dyke intrusions which were recorded during the ERT surveys (Figure 8-2 to Figure 8-14).

Figure 8-1 A Geotron Proton Magnetometer (G5 model) which was used during the magnetic surveys conducted in June 2015.

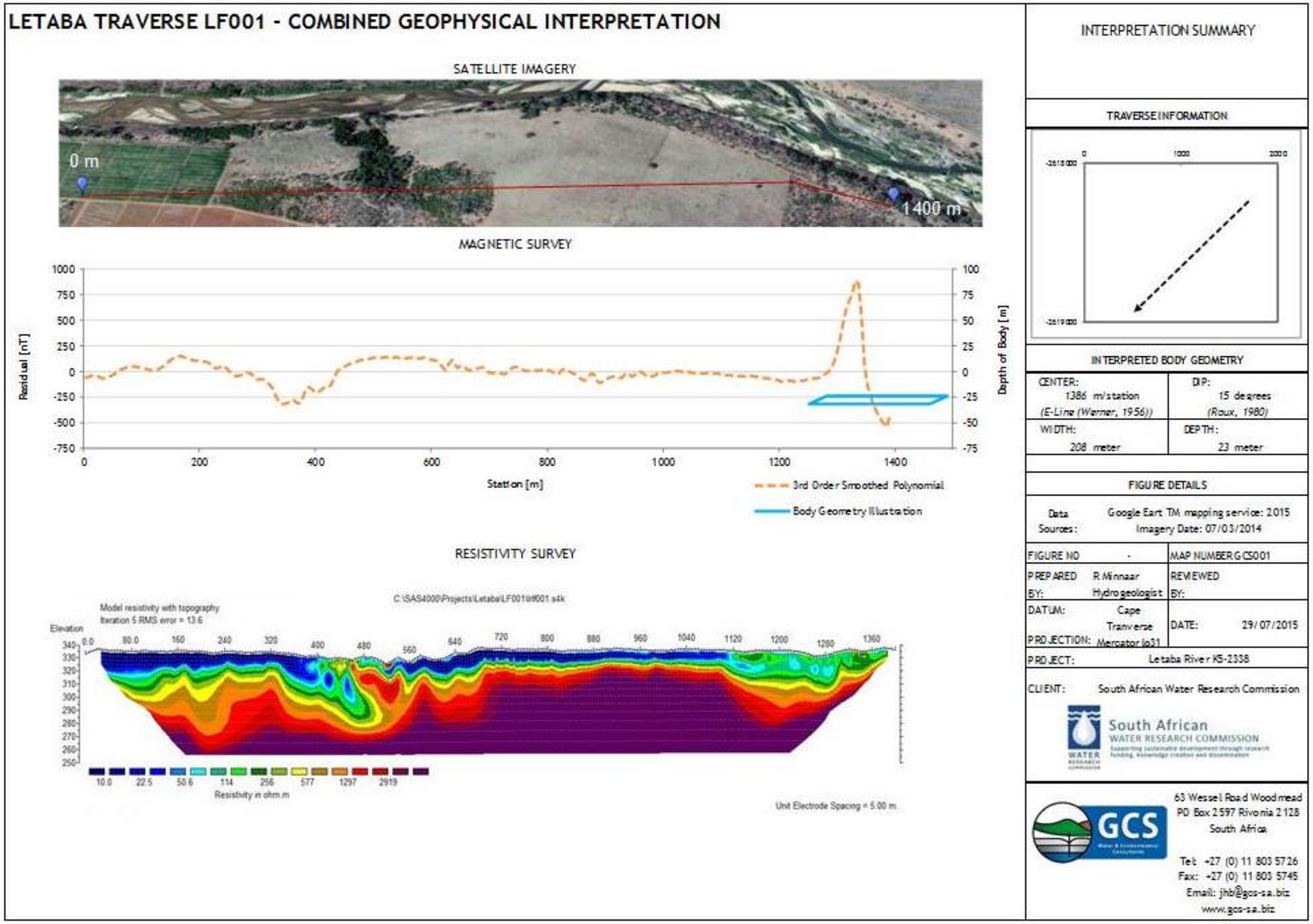

- Traverse runs from NE to SW
- Type-curves identified possible magnetic structure between 1200-1400m
- Structure located at change in shallow depth resistivity between 1200-1400m

Figure 8-2 Combined Geophysical Interpretation LF001

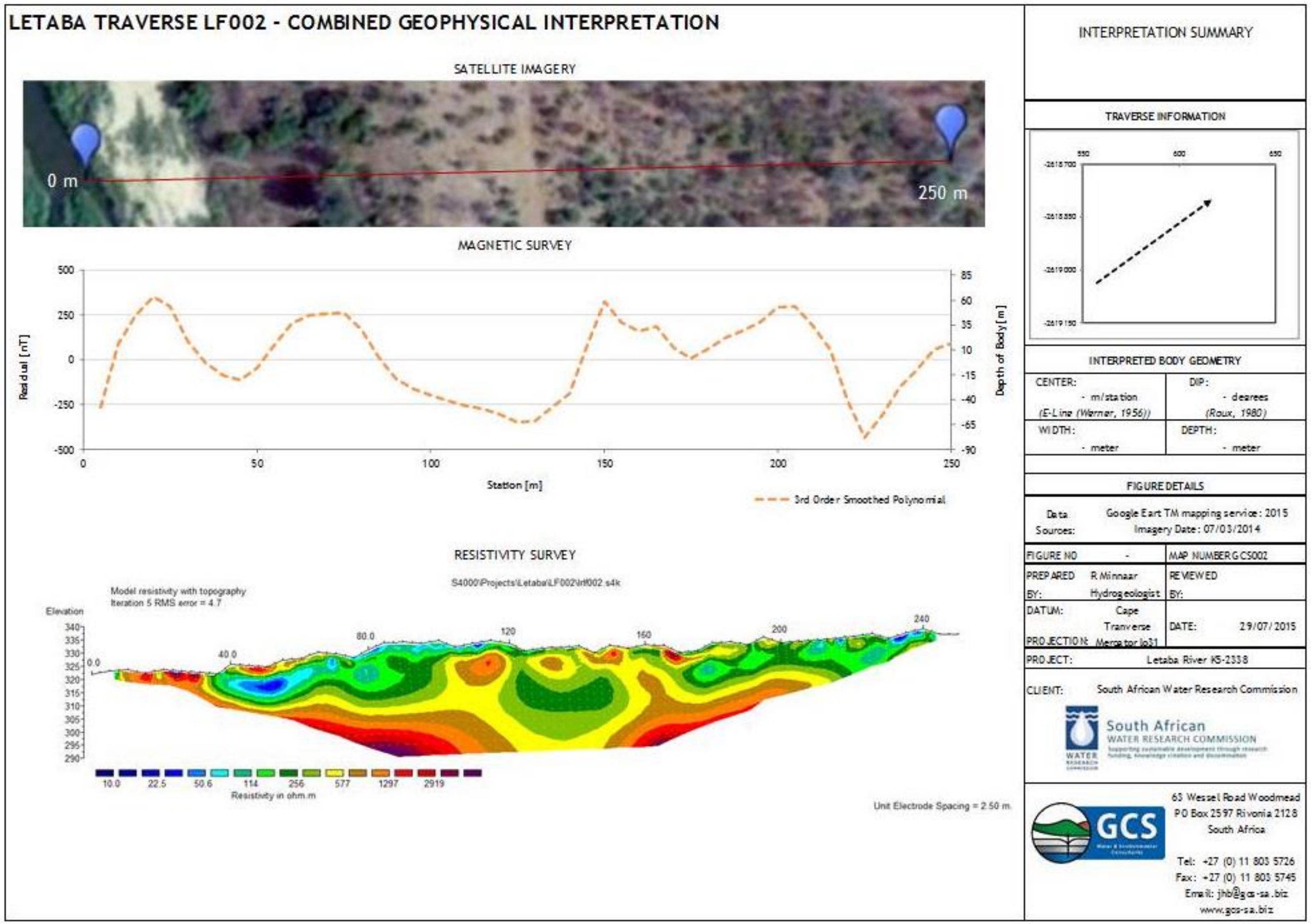

- Traverse runs from S to N
- Type-curves identified no clear structure
- Raw magnetic data was relatively higher than the background magnetic levels, possibly indicating the presence of a structure over the entire traverse length

Figure 8-3 Combined Geophysical Interpretation LF002

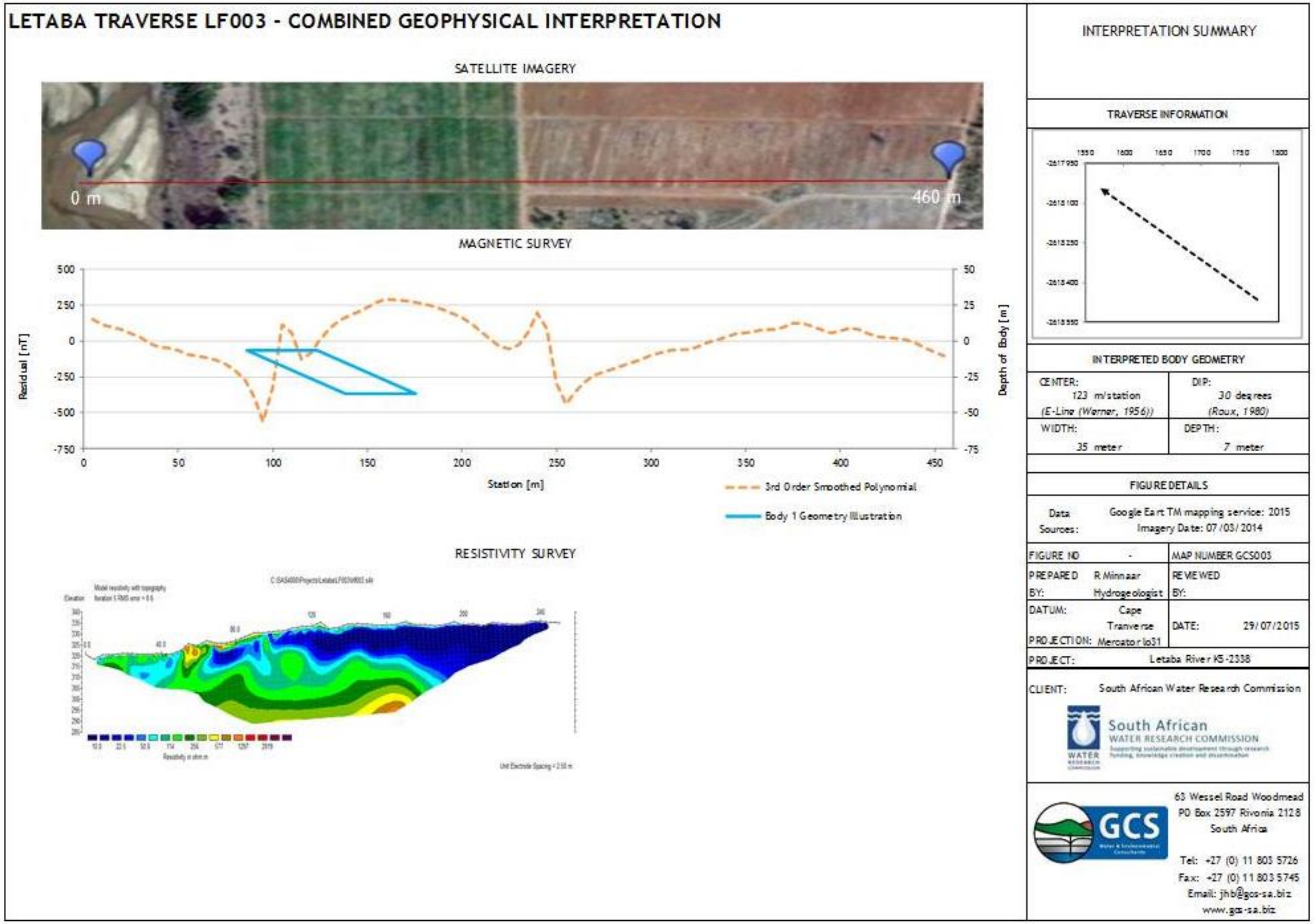

- Traverse runs from S to N
- Type-curves identified possible magnetic structure between 100-150m
- Structure location correlates to relatively higher resistivity values at shallower and deeper depths at ~100m

Figure 8-4 Combined Geophysical Interpretation LF003

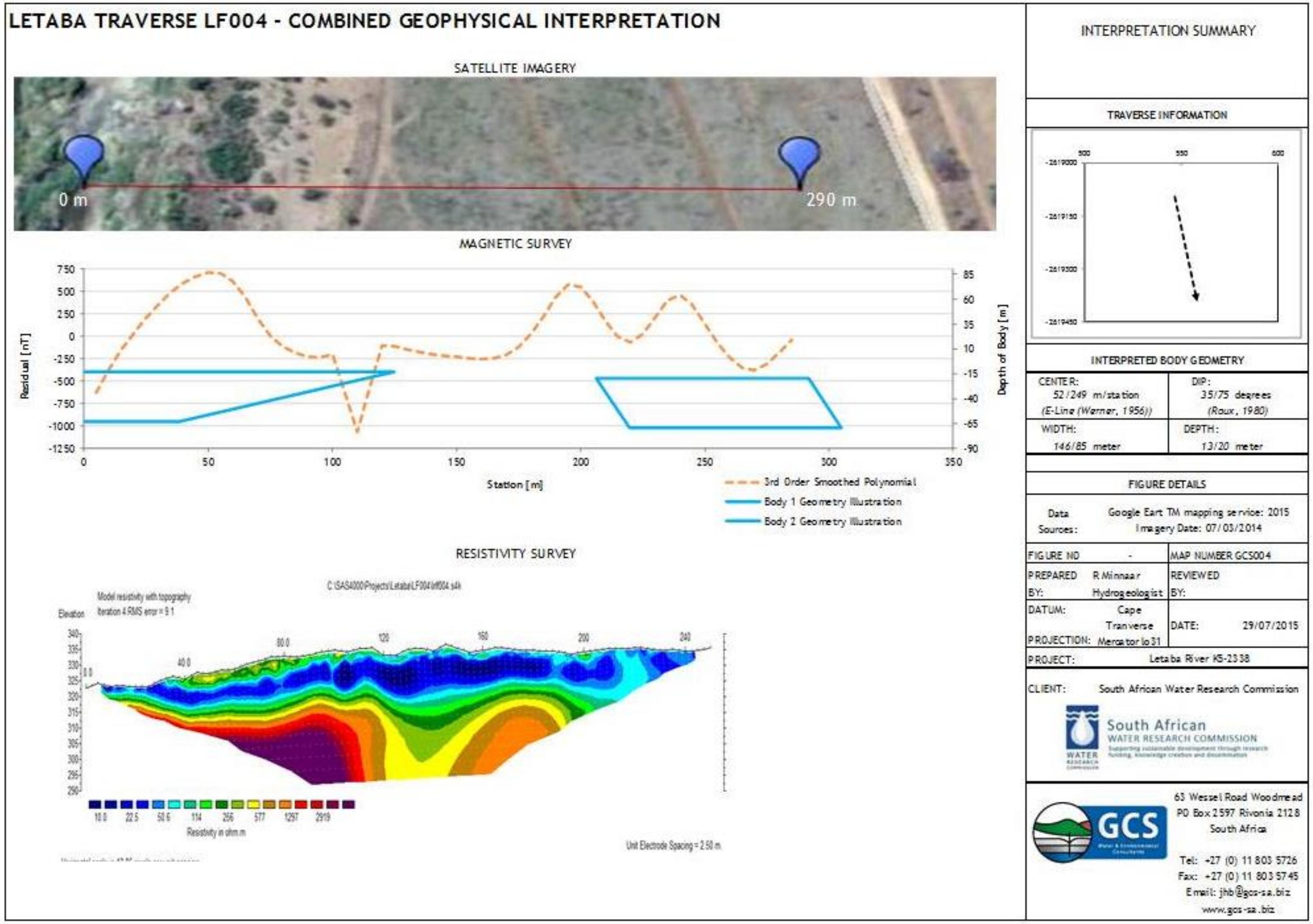

- Traverse runs from N to S
- Type-curves identified possible magnetic structure at approximately 50m and 250m
- Structure located at relatively higher resistivity values at depth

Figure 8-5 Combined Geophysical Interpretation LF004

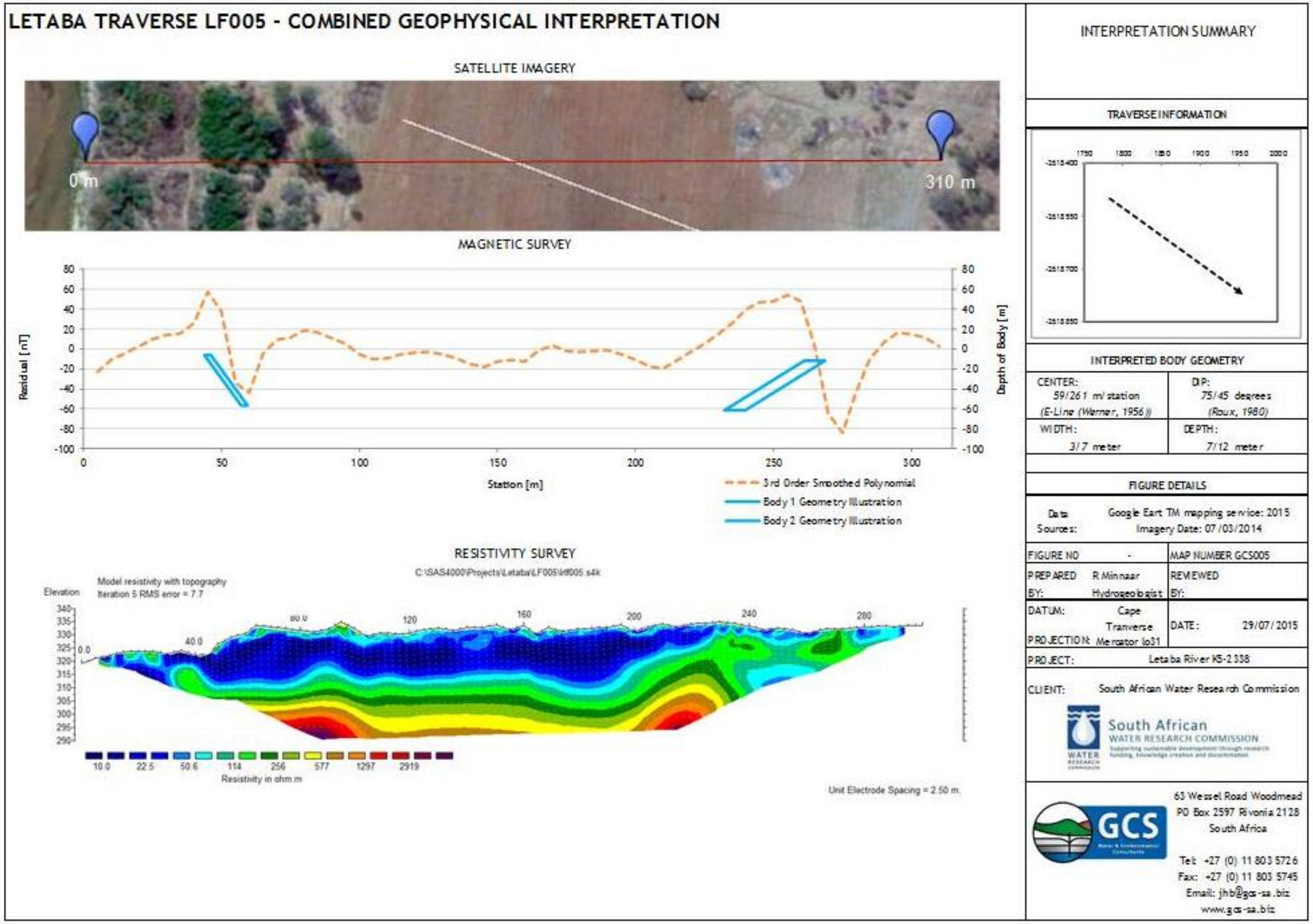

- Traverse runs from N to S
- Type-curves identified possible magnetic structure at 50 and 250m
- Location of possible structures correlates to relatively higher resistivity values

Figure 8-6 Combined Geophysical Interpretation LF005

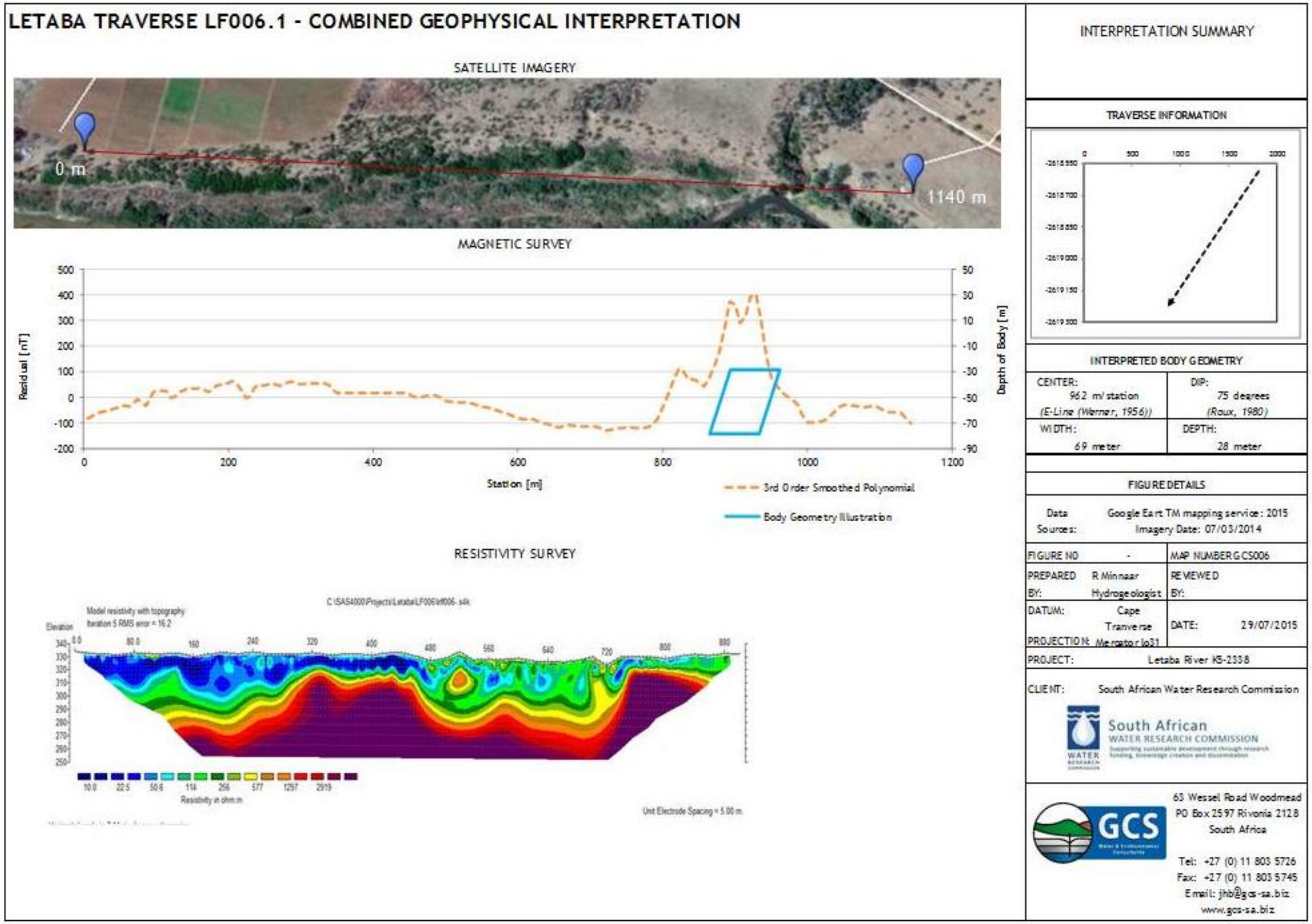

- Traverse runs from NE to SW
- Type-curves identified possible magnetic structure at 900m
- Structure located outside of original resistivity traverse

Figure 8-7 Combined Geophysical Interpretation LF006.1

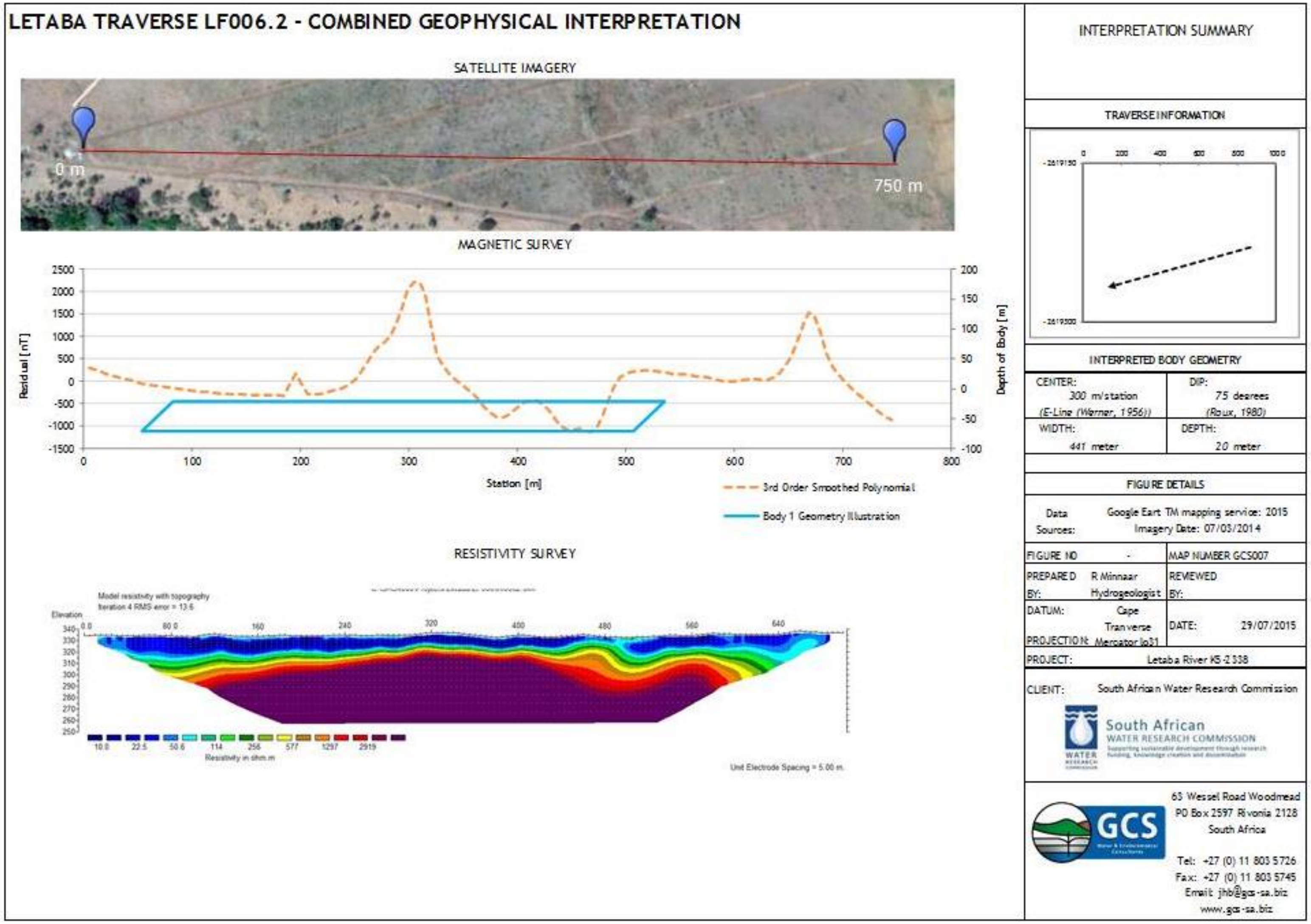

- Traverse runs from E to W
- Type-curves identified possible magnetic structure at 300m
- Structure location correlates to high resistivity values

Farms Area Summary:

- Generally NE/SW striking structures
- A possible East/West striking structure at LF004 and LF006.2 running parallel to Letaba River

Figure 8-8 Combined Geophysical Interpretation LF006.2

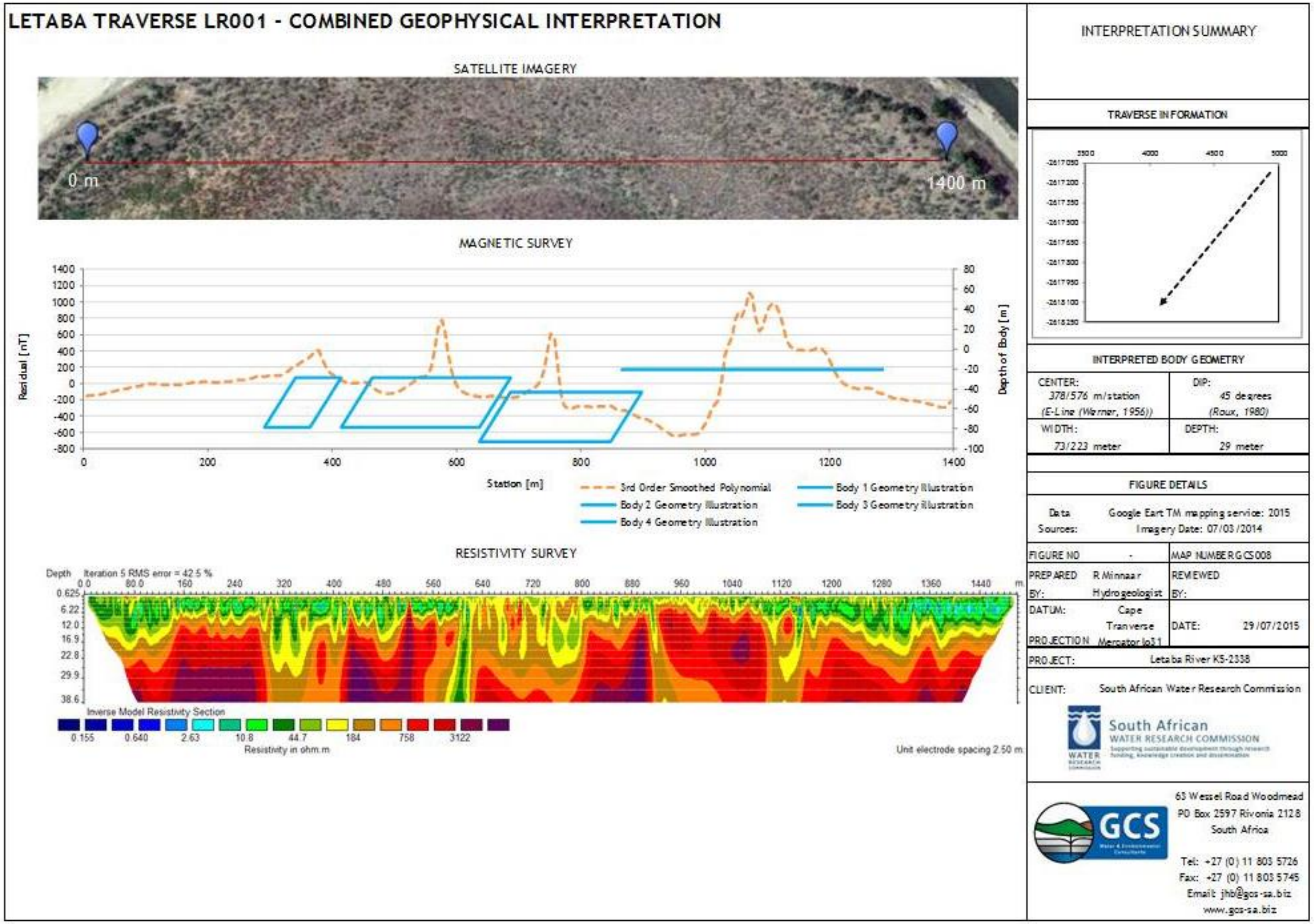

- Traverse runs from NE to SW
- Type-curves identified several possible magnetic structures at 300, 500, 750 and 1100m
- Deeper located dyke structures at 300, 500 and 750m
- Possible sill structure at 1100m

Figure 8-9 Combined Geophysical Interpretation LR001

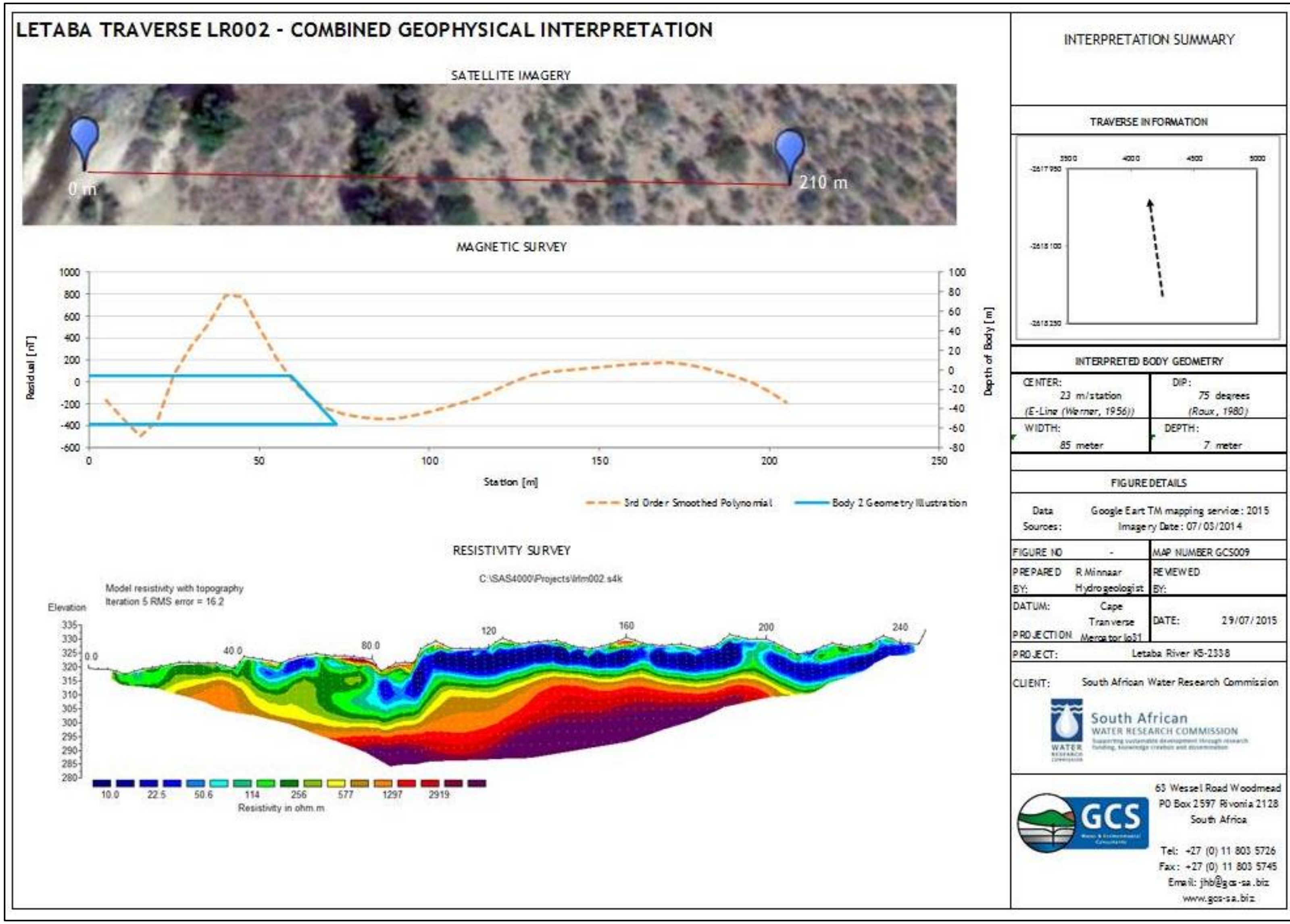

- Traverse runs from SE to NW
- Type-curves identified possible magnetic structure at 50m at ~ end of river bank

Figure 8-10 Combined Geophysical Interpretation LR002

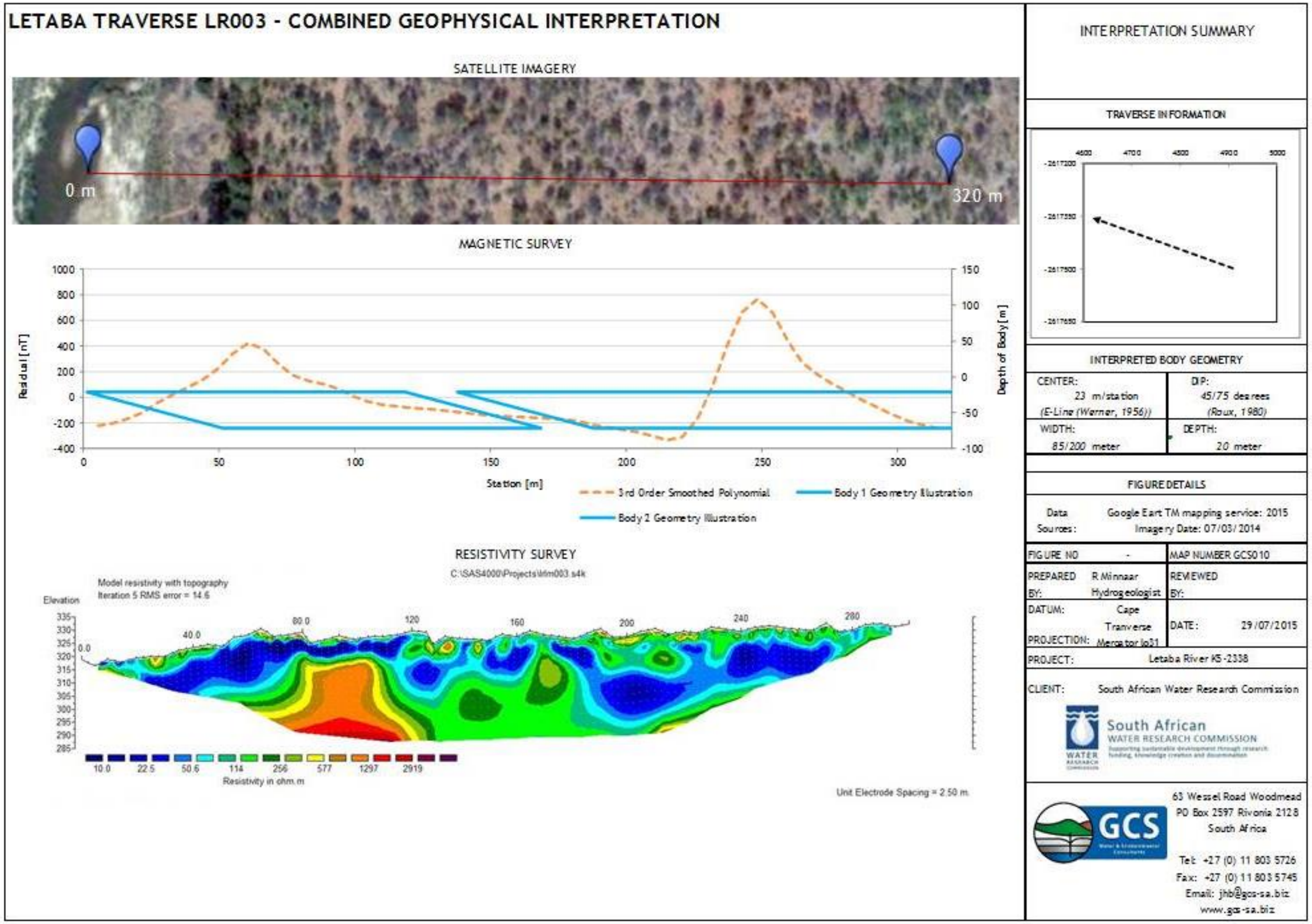

- Traverse runs from SE to NW
- Type-curves identified possible magnetic structures at 100 and 250m, which seem to be extensive in area along traverse direction
- Structures possibly running parallel to river

Figure 8-11 Combined Geophysical Interpretation LR003

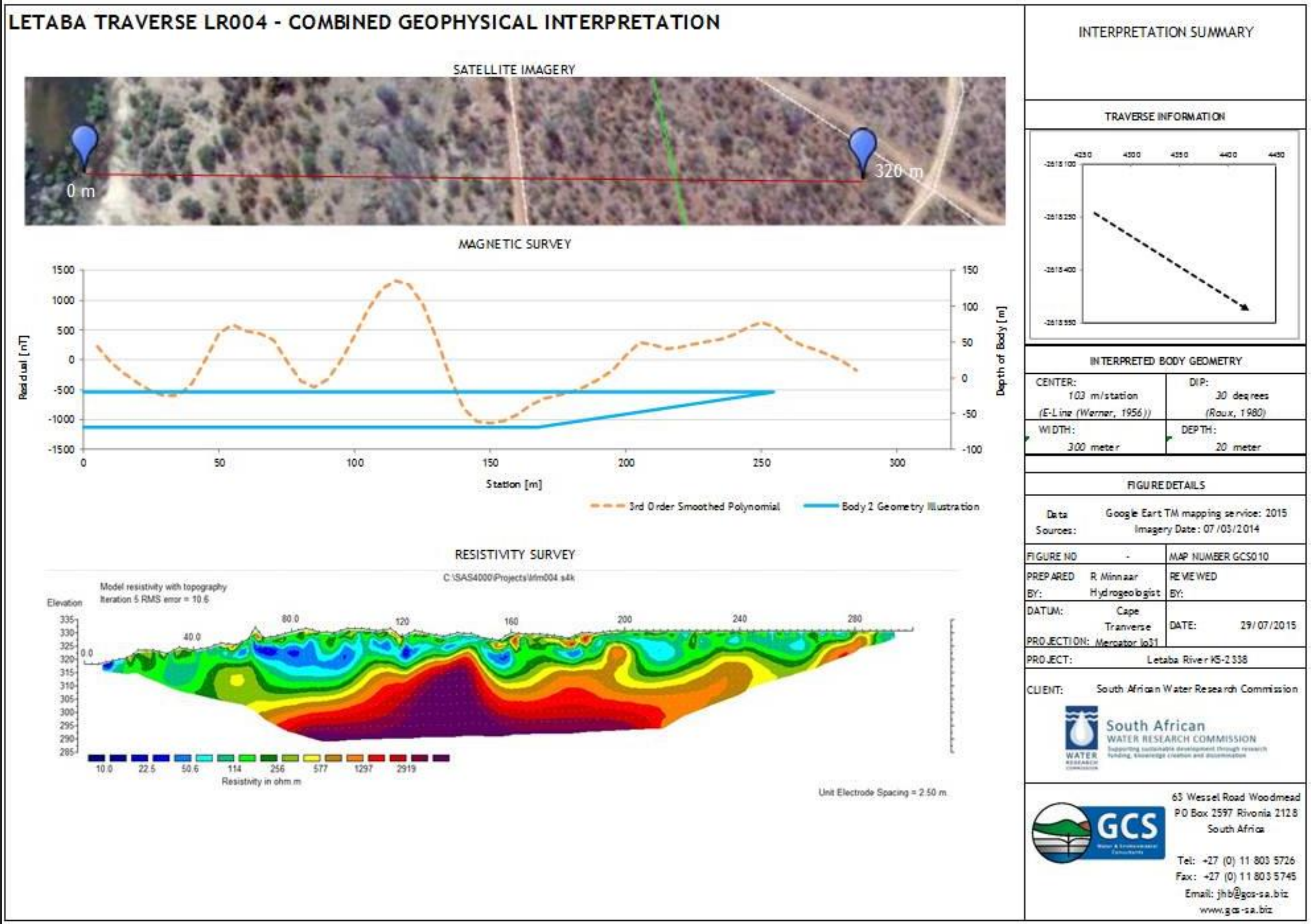

- Traverse runs from NW to SE
- Type-curves identified possible magnetic structure at 100m
- Structure location correlates to high resistivity values
- Structure possibly running parallel to river and plunging towards the river

Figure 8-12 Combined Geophysical Interpretation LR004

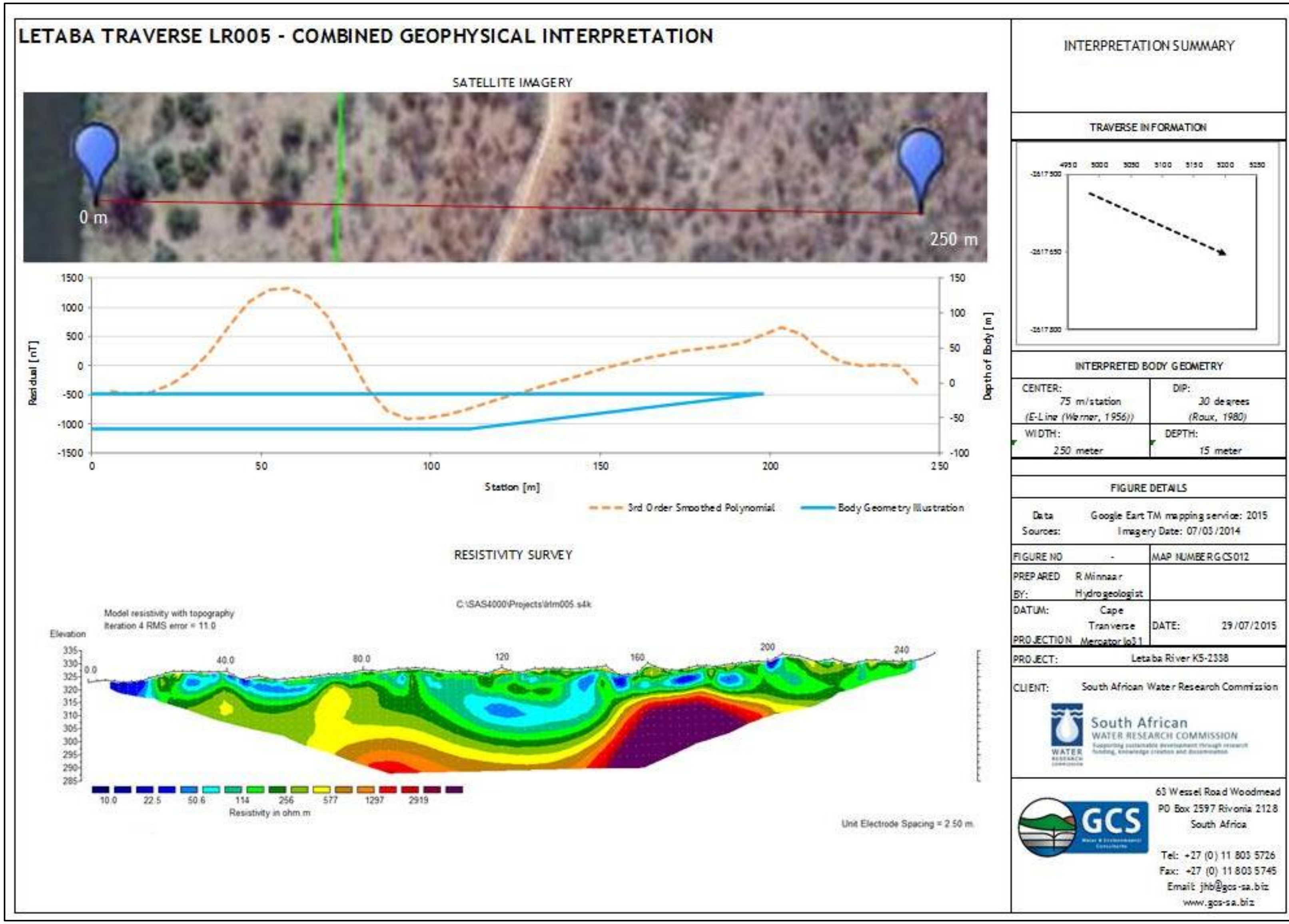

- Traverse runs from NW to SE
- Type-curves identified possible magnetic structure at 50m
- Structure location approximately at higher resistivity values
- Structure possibly striking parallel to river

Figure 8-13 Combined Geophysical Interpretation LR005

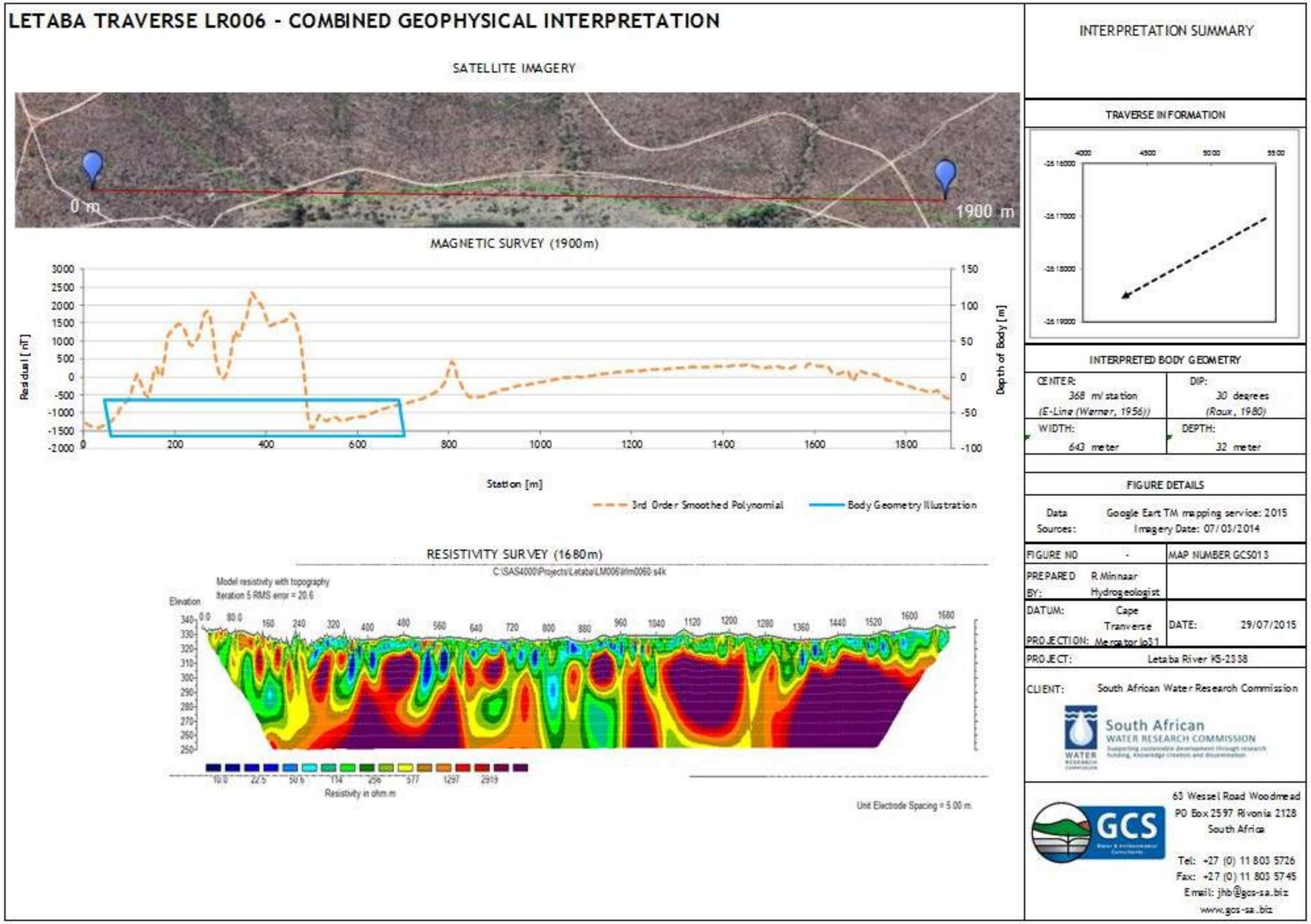

- Traverse runs from NE to SW
- Type-curves identified possible magnetic structure at 400m
- Structure location seems to not correlate to resistivity data along traverse direction
- Traverse was extended ~400m in a North-eastern direction, as relatively high magnetic recordings were noted at start of original resistivity traverse

Figure 8-14 Combined Geophysical Interpretation LR006

In summary, the results obtained from the magnetic surveys correlated well with the ERT geophysics survey data. In most cases the same intrusions identified during the geophysics surveys were observed in the magnetic surveys as well as additional details regarding structure width, depth, direction and dip. In general, several structures were identified that struck parallel to the Letaba River with a general strike direction of NE/SW.

Initial field observations, geophysics and Google Earth imagery alluded to a higher density of dyke intrusions downstream in the protected areas compared to the farming areas. This has been confirmed by the magnetic surveys which recorded at least two NE/SW striking structures running parallel to river located NW of Letaba River and at least one NE/SW striking structure running parallel to river located SE of Letaba River.

8.1.2. Updated Geophysics Interpretation

The initial interpretation of the geophysics surveys were updated based on findings drawn during the drilling process of 4 sets of boreholes. These piezometric boreholes were drilled along resistivity transects LF003, LF005 and LR005. This provided the opportunity to confirm the predicted water levels, estimated weathering depth and presence of alluvial deposits on old floodplains. The updated geophysics conceptual understanding now is displayed in Figure 8-15 to Figure 8-17.

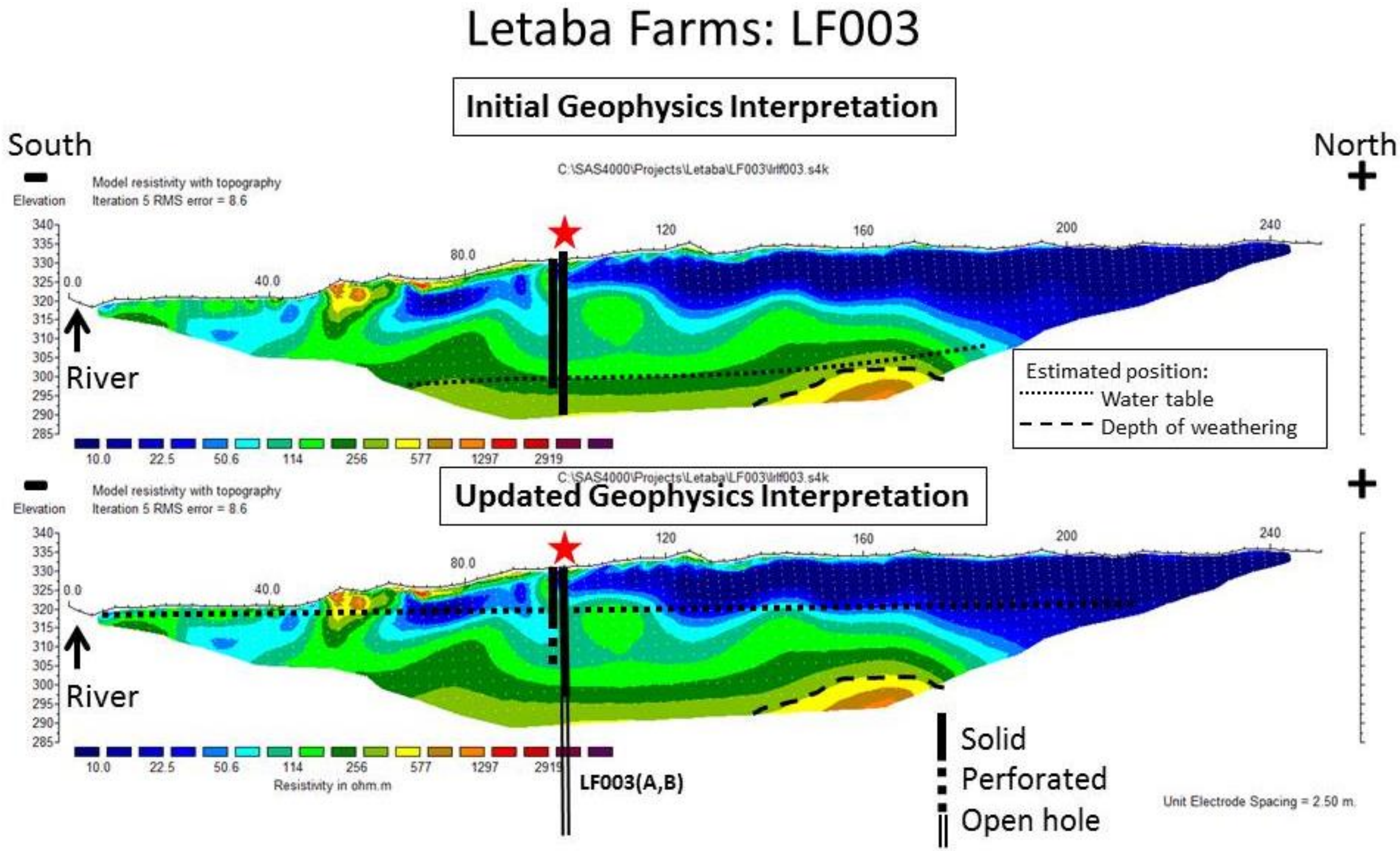

Initially it was assumed that there was a deep water table at around 30m. However, since the boreholes have been drilled it has been verified that it was in fact a shallow water table at around 11m which happens to be the level of the water in the adjacent Letaba River about 100m away.

Figure 8-15 Updated Geophysical Interpretation of Transect LF003

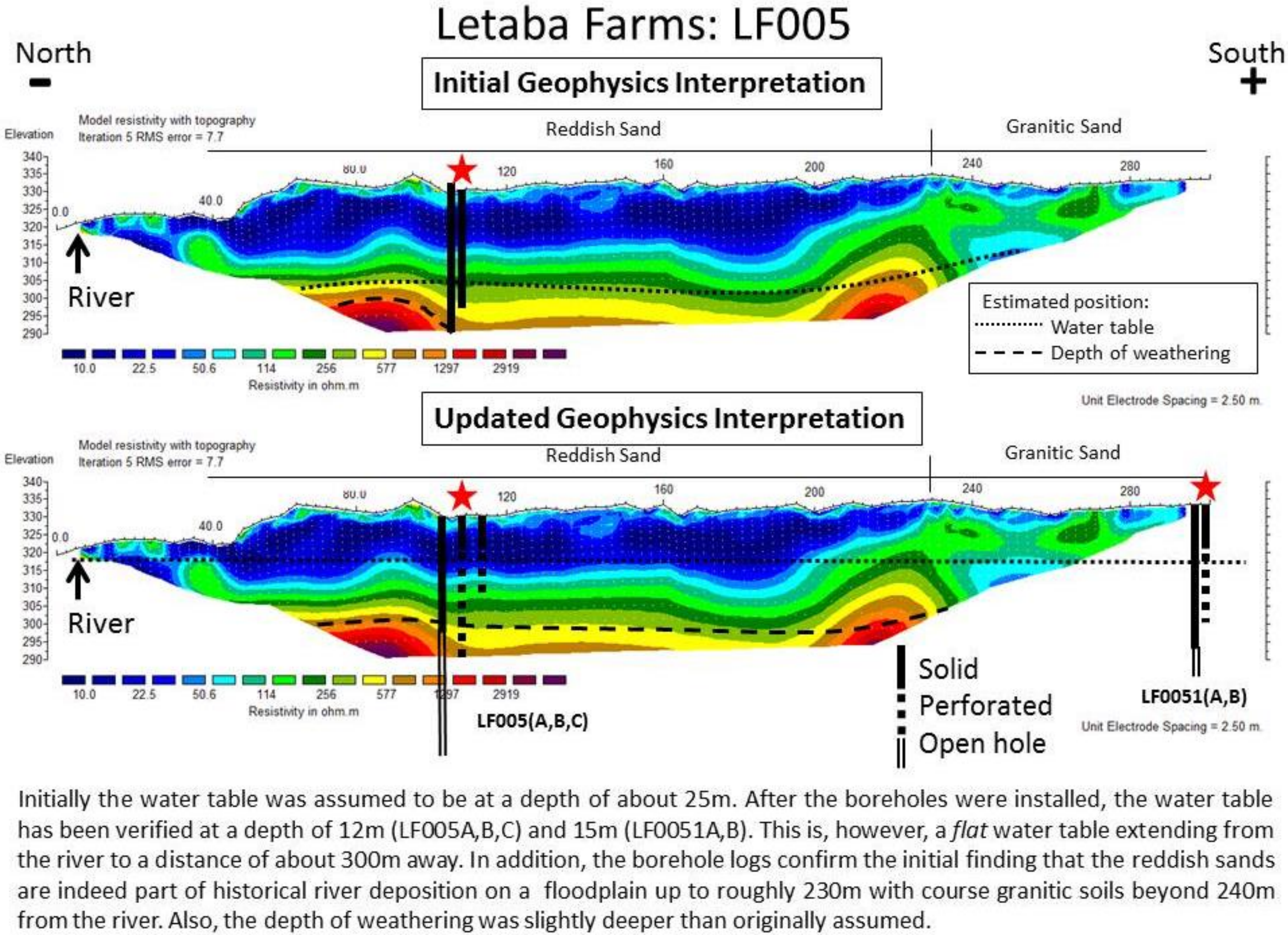

Initially the water table was assumed to be at a depth of about 25m. After the boreholes were installed, the water table has been verified at a depth of 12m (LF005A,B,C) and 15m (LF0051A,B). This is, however, a *flat* water table extending from the river to a distance of about 300m away. In addition, the borehole logs confirm the initial finding that the reddish sands are indeed part of historical river deposition on a floodplain up to roughly 230m with course granitic soils beyond 240m from the river. Also, the depth of weathering was slightly deeper than originally assumed.

Figure 8-16 Updated Geophysical Interpretation of Transect LF005

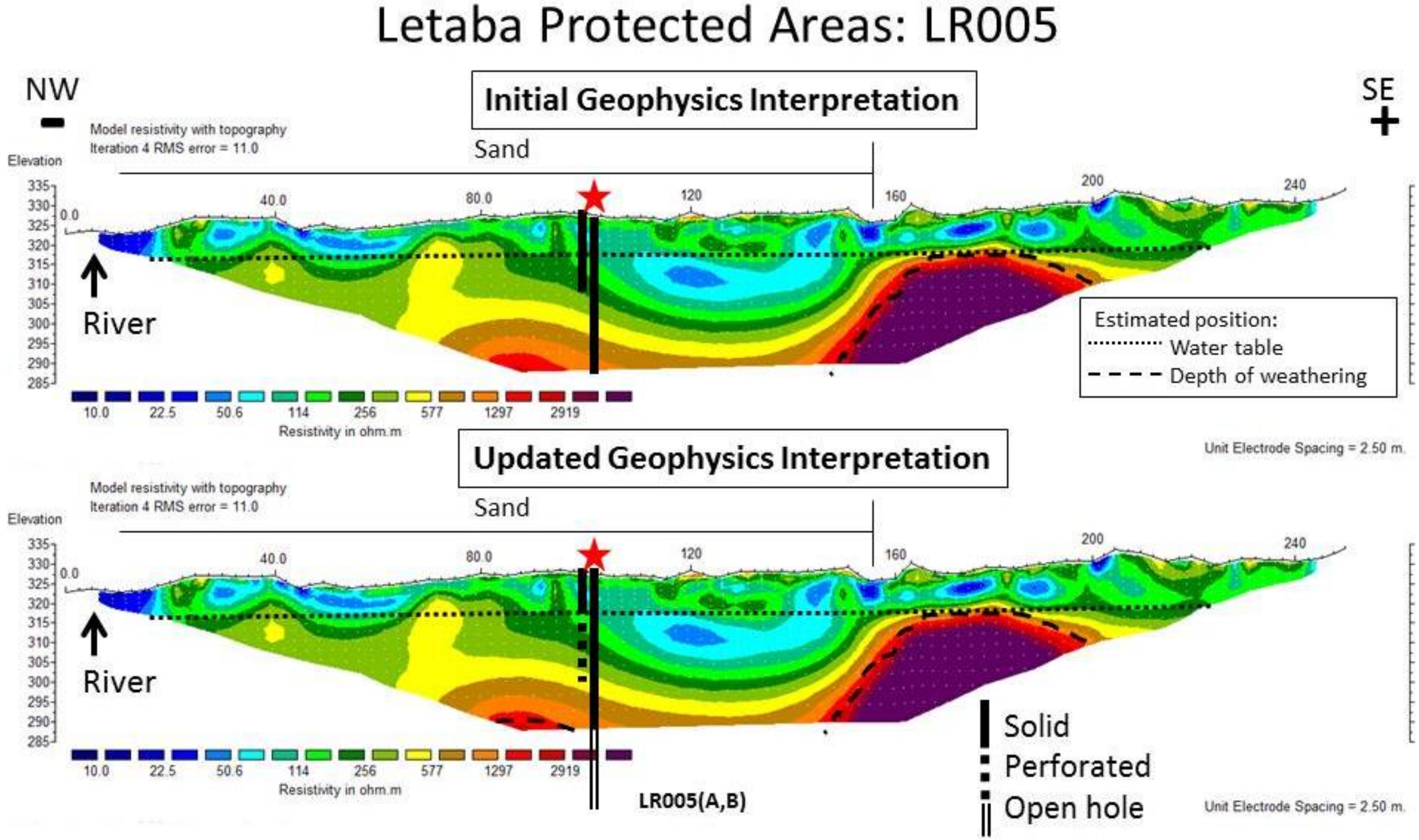

After drilling boreholes LR005 (A,B), the water table was confirmed to be at roughly the same depth as estimated from the initial geophysics surveys. Likewise, weathering was confirmed at a depth of around 38m where the boreholes were installed. Initial interpretation of the resistivity profiles concluded the presence of deep sands close to river which was thought to be part of an alluvial aquifer. This has been confirmed by the borehole logs with the presence of coarse sands till a depth of about 20m.

Figure 8-17 Updated Geophysical Interpretation of Transect LR005

8.1.3. Updated conceptual model: groundwater-surface water interaction

Based on data collected during geophysics surveys, magnetic surveys, aerial imagery, geological maps and borehole drilling logs, the conceptual understanding of the geohydrological processes have been updated. Figure 8-18 below displays the current conceptual model in three dimensions, i.e. river cross-section over both land-uses and aerial view. Currently, the conceptual understanding of the geohydrological system and the relationship between groundwater and surface water during the dry season takes into consideration the following aspects:

* Irrigators in the farming area abstract water directly out of the Letaba River while no water is directly abstracted in the protected areas. Thus, water is removed from the surface water body.

* There is evidence of old floodplains due to the presence of deep deposition of fine alluvial material. This has been confirmed by both the geophysics surveys and borehole drilling logs. These floodplains could aid efficient bank storage during high flows and sustain base flow during low flow months.

* In the protected areas, there is a higher density of dyke intrusions than in the farming area. The majority of these major structures run in a NE/SW direction which in some areas run parallel to the river and in other areas, traverse the river. In addition, a number of dykes have been visually observed to traverse the river within the protected areas. Therefore, it is assumed that these dykes (or the interface with surrounding geology) are acting as conduits for groundwater flow into the Letaba River. This idea is further supported by the results of the mass balance (Chapter 6) which showed that there is presently a groundwater contribution to increase the discharge along the river. Furthermore, a longitudinal hydro-chemistry survey conducted in November 2014 (Figure 8-19) also alluded to the likelihood of groundwater discharge into the river as Electricity Conductivity of the river freshened out further downstream into the protected areas.

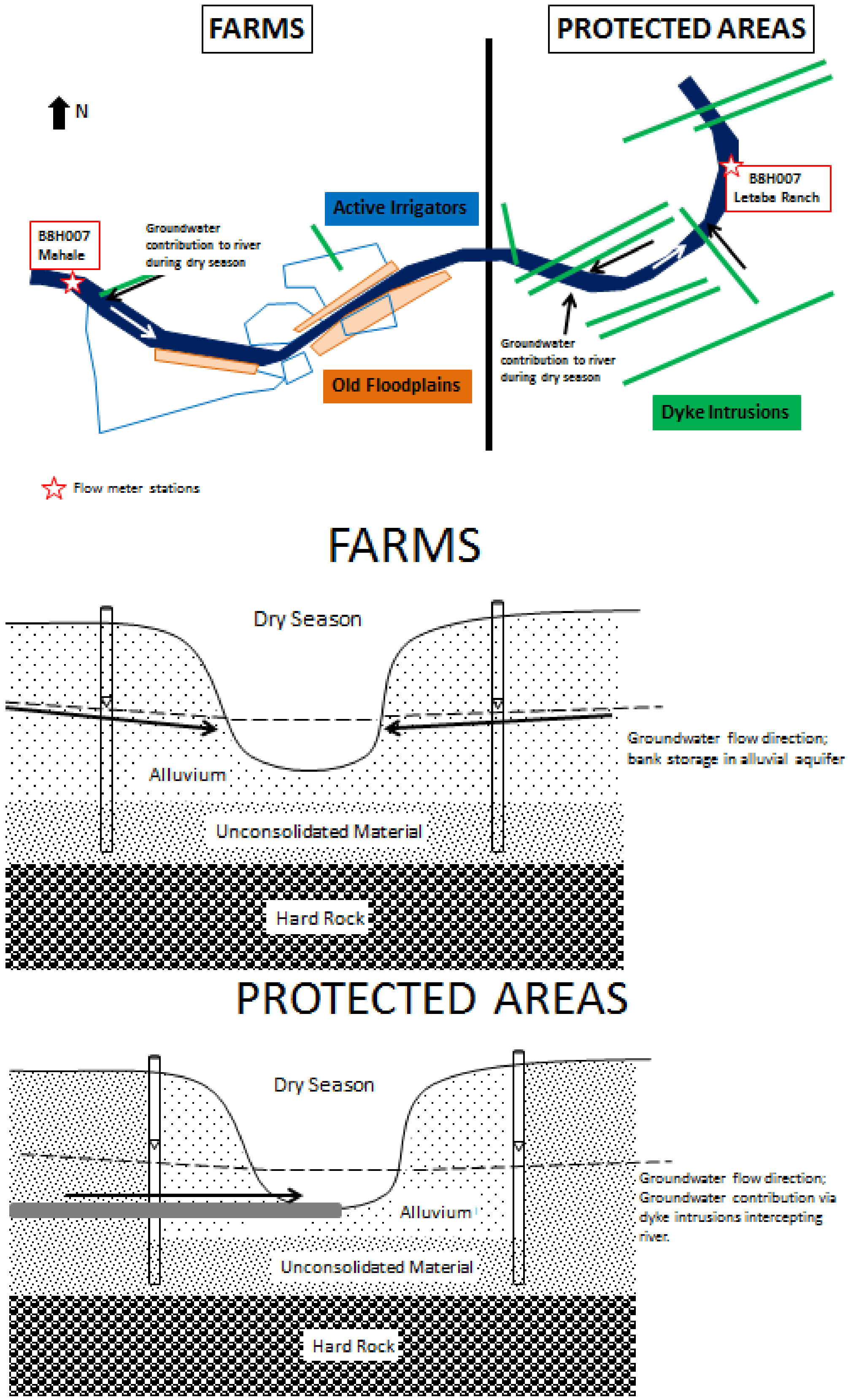

Figure 8-18 Updated geohydrological conceptual model of the study site

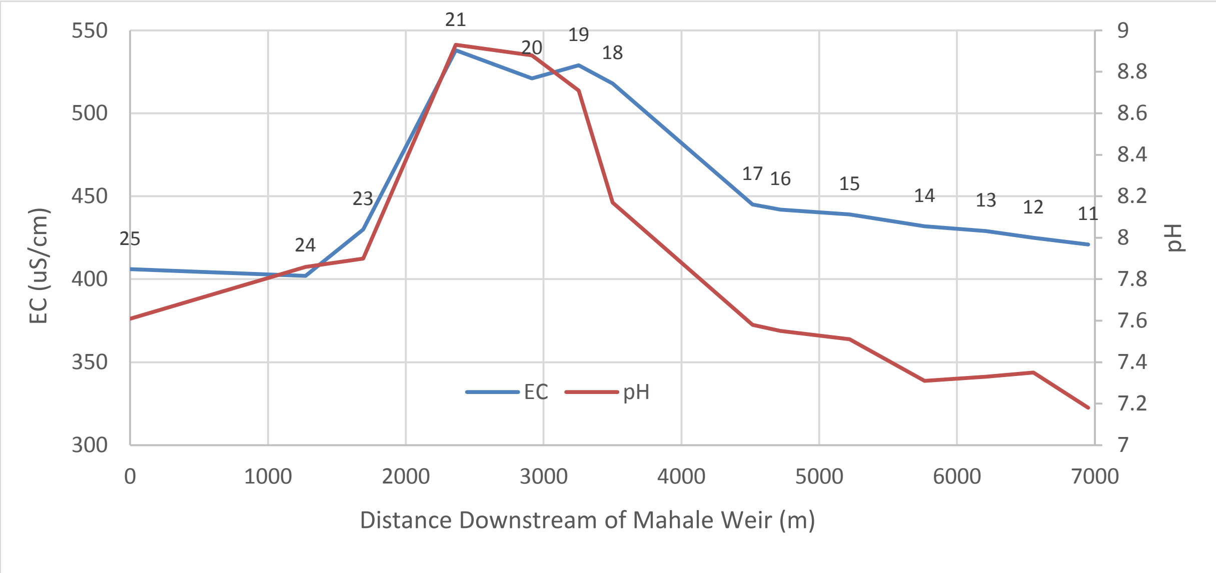

Figure 8-19 Results of longitudinal hydro-chemical snap-shot survey of the Letaba river between Mahale and Letaba Ranch on 24 November 2014

9. Concluding Comments and Workplan

Despite some delays which were outside of the projects control, the project is now in full operational mode. The data presented in the previous chapters has demonstrated the interesting processes and controls that may contribute (or not) to transmission loss of river hydrology in the lower Letaba, such as: the slight gain in streamflow between Mahale weir and Letaba Ranch. It will be interesting to determine whether this remains throughout the low-flow season and continues inter-annually as the region moves out of a wet cycle and into a potential dry cycle; furthermore the mechanisms for this streamflow gain perhaps via preferential freshwater inputs along the dyke intrusions will need to be explored through hydrochemistry and modelling. Over the next few months from July 2015, there will be a focus on the full integration of the riparian zone ET components which will allow us to determine whether this is a net loss of streamflow to ET over and above any potential groundwater contribution. In order to achieve this there will be a focus on the following:

- Work will continue in order to complete the borehole piezometric network. Work will then commence to hydraulically characterise the boreholes.

- Hydrochemistry and isotopic signatures of the river and surrounding groundwater will be monitored.

- Continuous mass balance analysis with further determinations of ET at the point scale in relation to borehole locations and a precise differential rating of the Mahale weir will be conducted.

- The Eddy Co-variance system will continue to collect data at the study site, although this is likely to be repositioned in order to account for the large variation in in-stream ETa. Meanwhile this data will be augmented by installing small lysimeter systems that will be replicated spatially in order to further quantify the spatial components of total evaporation between Mahale weir and Letaba Ranch. Furthermore Heat Pulse Velocity options will be explored to determine species specific water use in the riparian zone.

- Based on this SEBS data acquisition for spatial ET will continue and methods to develop an interpolated ET time series will be developed based on field collected data.

References

Abdelrady, RA. 2013. Evaporation over fresh and saline waters using SEBS, Unpublished Msc Thesis, Geo-Information Science and Earth Observation, University of Twente, The Netherlands.

Allen, RG, Pereira, LS, Raes, D and Smith, M.1998. Crop Evapotranspiration: Guidelines for Computing Crop Water Requirements, FAO Irrigation and Drainage Paper 56, FAO, Rome, 300.

Badola, A. 2009. Validation of Surface Energy Balance System (SEBS) over forest land cover and sensitivity analysis of the model, Unpublished Msc Thesis, International Institute for Geo-Information Science and Earth Observation, Enschede, The Netherlands.

Bastiaansen, WGM, Menenti, M, Feddes, RA, Holtslag, AAM. 1998a. A remote sensing surface energy budget algorithm for land (SEBAL). 1. Formulation. Journal of Hydrology 212-213(1-4): 213.Bastiaansen, WGM. 2000. SEBAL – based sensible and latent heat fluxes in the irrigated Gediz Basin, Turkey. Journal of Hydrology 229: 87-100.

Costa, AC, Foerster, S, de Araujo, JC and Bronstert, A. 2013. Analysis of channel transmission losses in a dryland river reach in north-eastern Brazil using streamflow series, groundwater level series and multi-temporal satellite data. *Hydrological Processe*s 27: 1046–1060.

Costelloe, JF, Grayson, RB, Argent, RM, and McMahon, TA. 2003. Modelling the flow regime of an arid zone floodplain river, Diamantina River, Australia. *Environmental Modelling & Software* 18: 693–703.

Cataldo, J, Behr, C, Montalto, F and Pierce RJ. 2004. A Summary of Published Reports of Transmission Losses in Ephemeral Streams in the U.S. *A Report to the National Center for Housing and the Environment*, August 5, 2004.

Cataldo, J, Behr, C, Montalto, F and Pierce, RJ. 2010. Prediction of Transmission Losses in Ephemeral Streams, Western U.S.A. *The Open Hydrology Journal* 4: 19-34.

Courault, D, Clastre, P, Guinot, JP and Seguin, B. 1994. Analyse des s´echeresses de 1988 `a 1990 en France `a partir de l'analyse combin´ee de donn´ees satellitaires NOAA-AVHRR et d'un mod`ele agrom´et´eorologique. Agronomie 14: 41–56.

Courault, D, Seguin, B and Olioso, A. 2005. Review on estimation of ET from remote sensing data: From empirical to numerical modelling approaches, *Irrigation and drainage sytems* 19: 223-249.

Dingman, SL. 2009. Fluvial Hydraulics. Oxford University Press pp570

Elhag, M, Psilovikos, A, Manakos, Iand Perakis, K. 2011. Application of the Sebs Water Balance Model in Estimating Daily Evapotranspiration and Evaporative Fraction from Remote Sensing Data Over the Nile Delta. *Water Resources Management* 25: 2731–2742.

Ershadi, A, McCabe, MF, Evans, JP, Walker, JP and Pipunic, R. 2011. Estimation of evaporation using the surface energy balance system (SEBS) and numerical models, *3rd International Symposium on Remote Sensing of Environment, Sydney, Australia, 10-15 April.*

Everson, CS, Burger, C, Olbrich, BW and Gush, MB. 2001. Verification of estimates of water use from riverine vegetation on the Sabie River in the Kruger National Park. WRC Report 877/1/01.

Gibson, LA, M¨unch, Z and Engelbrecht, J. 2011. Particular uncertainties encountered in using a pre-packaged SEBS model to derive evapotranspiration in a heterogeneous study area in South Africa. *Hydrol Earth Syst Sci* 15: 295–310.

Gentine, P, Entekhabi, D and Polcher, J. 2011. The Diurnal Behavior of Evaporative Fraction in the Soil-Vegetation-Atmospheric Boundary Layer Continuum. *Journal of Hydrometeorology* 12:1530-1546.

Ghorbani, A, Mossivand, MA and Ouri, AE. 2012. Utility of the Normalised Difference Vegetation Index (NDVI) for land/canopy cover mapping in Khalkhal County (Iran). *Annals of Biological Research* 3(12):5494-5503.

Gribovszki, Z., Szilágyi, J., & Kalicz, P. 2010. Diurnal fluctuations in shallow groundwater levels and streamflow rates and their interpretation - A review. *Journal of Hydrology*, *385*(1-4), 371–383.

Hacker, F. 2005. Model for Water Availability in Semi-Arid Environments (WASA): Estimation of transmission losses by infiltration at rivers in the semi-arid Federal State of Ceara (Brazil). MSc Thesis, University of Potsdam, Germany

Heath, RC. 1993. Basics of Groundwater Hydrology. US Geological Survey Water Supply Paper 2220, USGS p91

Holme, A, Burnside, DG and Mitchell, AA. (1987). The development of a system for monitoring trend in range condition in the arid shrublands of Western Australia. *Australian Rangeland Journal* 9:14-20.

Huang, Y, Chen, X, Chen X and Ou, G. 2015. Transmission losses during two flood events in the Platte River, south-central Nebraska. *Journal of Hydrology* 520: 244–253.

Hughes, DA and Sami, K. 1992. Transmission losses to alluvium and associated moisture dynamics in a semi-arid ephemeral channel system in southern Africa. *Hydrological Processes* 6: 45-53.

Hughes, DA. 2008. Modelling semi-arid and arid hydrology and water resources the Southern African experience. gwadi.org/sites/gwadi.org/files/hughes_L5.pdf‎ Hughes, DA, Mallory, SJL and Louw D. 2008. Methods and software for the real-time implementation of the ecological reserve-explanations and user manual. *WRC Report 1582/1/08*.

Jarmain, C, Bastiaansen, W, Mengistu, MG and Kongo, V. 2009. A Methodology for Near-Real TimeSpatial Estimation of Evaporation, *WRC Report No. 1751/1/09*, ISBN 978-1-77005-725-8.

Jin, X, Wan, L and Su, Z, 2005. Research on evaporation of Taiyuan basin area by using remote sensing Hydrol Earth Syst Sci 2: 209–227.

Jovanovic, N and Israel, S. 2012. Critical Review of Methods for the Estimation of Actual Evapotranspiration in Hydrological Models, *Council for Scientific and Industrial Research, Stellenbosch, South Africa.*

Kirchner, JW. 2006. Getting the right answers for the right reasons: Linking measurements, analyses, and models to advance the science of hydrology. Water Resources Research 42, W03S94, doi: 10.1029/2005WR004362.

Lagouarde, JP and Brunet, Y. 1991. Suivi de l'´evapotranspiration r´eelle journali`ere `a partir des donn´ees NOAA-AVHRR lors de la campagne HAPEX-MOBILHY. 5`eme coll.int."Mesures physiques et signatures en t´el´ed´etection". *Courchevel* 319: 569–572.

Lane, LJ. 1990. Transmission losses, flood peaks and groundwater recharge. *Hydraulics/hydrology of arid lands (H2AL): proceedings of the International Society of Civil Engineers, Hydraulics Division 1990*.

Lange, J. 2005. Dynamics of transmission losses in a large arid stream channel. *Journal of Hydrology* 306: 112–126.

Lhomme, JP and Elguero, E. 1998. Examination of evaporative fraction diurnal behaviour using a soil-vegetation model coupled with a mixed-layer model. *Hydrology and Earth System Sciences* 3(2): 259- 270.

Li F, Kustas WP, Anderson MC, Prueger, JH and Scott, R.L. 2008. Effect of remote sensing spatial resolution on interpreting tower-based flux observations. *Remote Sens Environ* 112: 337–349.

Li, Z, Tang, R, Wan, Z, Bi, Y, Zhou, C, Tang, B, Yan, G and Zhang, X. 2009. A Review of Current Methodologies for Regional Evapotranspiration Estimation from Remotely Sensed Data. *Sensors* 9(5): 3801-3853.

Lin, W. 2006. Satellite based regional scale evapotranspiration in the Hebei Plain, Northeastern China, Msc Thesis, International Institute for Geo-information Science and Earth Observation, The Netherlands.

Long, D and Singh, VP. 2012. A modified surface energy balance algorithm for land (M-SEBAL) based on a trapezoidal framework *Water Resour Res* 48, W02528, doi:10.1029/2011WR010607.

McKenzie, RS and Craig, AR. 2001. Evaluation of river losses from the Orange River using hydraulic modelling. *Journal of Hydrology* 241: 62–69.

Kustas, WP and Daughtry, CST. 1989. Estimation of the soil heat flux/net radiation ratio from spectral data. *Agr Forest Meteorol* 49: 205–223.

Ma, W, Ma, Y, Hu, Z, Su, Z, Wang, J and Ishikawa, H. 2011. Estimating surface fluxes over middle and upper streams of the Heihe River Basin with ASTER imagery. *Hydrol Earth Syst Sci* 15: 1403–1413.

Ma, W, Ma, Y and Ishikawa, H. 2014. Evaluation of the SEBS for upscaling the evapotranspiration based on in-situ observations over the Tibetan Plateau. *Atmospheric Research* 138: 91-97.

Matinfar, RH and Soorghali, M. 2014. Estimate evapotranspiration (ET) using SEBS Model based on Landsat 5 (TM) thermal data and GIS. *Indian Journal of Fundamental and Applied Life Sciences* 4(3): 30-34.

McCabe, MF and Wood, EF. 2006. Scale influences on the remote estimation of evapotranspiration using multiple satellite sensors. *Remote Sens Environ* 105: 271–285.

McMahon, TA. 1979. Hydrological characteristics of arid zones. Symposium on the hydrology of areas of low precipitation, IAHS Publ. No 128. Proc. Canberra Symposium, Dec. 1979: 105-123.

Menenti, M and Choudhury, B. 1993. Parameterization of land surface evaporation by means of location dependent potential evaporation and surface temperature range. Proceedings of IAHS conference on Land Surface Processes. *IAHS Publ* 212: 561-568.

Mengistu, MG, Everson, CS, Moyo, NC and Savage, MJ. 2014. The validation of the variables (evaporation and soil moisture) in hydrometeorological models. *WRC Report No. 2066/1/13*, ISBN 978-1-4312-0514-1.

Mertz, SK. 2010. Evapotranspiration measurement: *informing water management in Australia*, Waterlines Report Series Number 35.

Mkhwanazi, MM and Chavez, JL. 2013. Mapping evapotranspiration with the remote sensing Et algorithms METRIC and SEBAL under advective and non-advective conditions: accuracy determination with weighing lysimeters. *Hydrology Days 2013.*

Monteith, JL. 1973. *Principles of environmental physics*. Edward Arnold Press. 241 pp.

Mu, Q, FA, Heinsch, Zhao, M and Running, SW. 2007. Development of a global evapotranspiration algorithm based on MODIS and global meteorology data. *Remote Sensing Environ* 11:519–536.

Muhammad, AH. 2012. Satellite based evapotranspiration estimation and runoff simulation: A top model application to the Gilgel Abay Catchment, Ethiopia, Msc Thesis, Enschede, The Netherlands, 2012.

Pardo, N, Sanchez, LM, Timmermans, J, Su, Z, Perez, IA and Garcia, MA. 2014. SEBS validation in a Spanish rotating crop. *Agricultural and Forest Meteorology* 195-196: 132-142.

Petorreli, N, Vik, JO, Mysterud, A, Gaillard, JM, Tucker, CJ and Stenseth, NC. 2005. Using the satellite-derived NDVI to assess ecological responses to environmental change. *Trends in Ecology and Evolution* 20:503-510.

Rwasoka *et al.* (2011)

Ramsey, RD, Wright Jr, DL and McGinty C. 2004. Enhanced Thematic Mapper to Monitor Vegetation Cover in Shrub-Steppe Environments. *Geocarto International* 19(2): 39-47.

Senay, GB, Budde, M, Verdin, JP and Melesse, AM. 2007. A coupled remote sensing and simplified surface energy balance approach to estimate actual evapotranspiration from irrigated fields. *Sensors* 7(6): 979–1000.

Shanafield, M and Cook, PG. 2014. Transmission losses, infiltration and groundwater recharge through ephemeral and intermittent streambeds: A review of applied methods. *Journal of Hydrology* 511: 518–529.

Simonetti, E, Simonetti, D and Preatoni, D. 2014. Phenology-based land cover classification using Landsat 8 time series. *JRC Technical Reports*, ISBN 978-92-79-40844-1, doi: 10.2788/15561, Luxembourg: Publications Office of the European Union.

Stewart, JB. 1996. Extrapolation of evaporation at time of satellite overpass to daily totals, In: J.B. Stewart *et al.* (editors) *Scaling up in Hydrology using Remote Sensing*. Wiley, Chichester, UK.

Su, Z, Schmugge, T, Kustas, WP and Massman, WJ. 2001. An evaluation of two models for estimation of the roughness height for heat transfer between the land surface and the atmosphere. *Journal of Appl Meteorol* 40(10): 1933-1951.

Su, Z. 2002. The Surface Balance Energy System (SEBS) for estimating turbulent heat fluxes. *Hydrology and Earth System Sciences*, 6(1): 85-99.

Timmermans, J. 2014. Personal communication. International Institute of Geo-information sciences and Earth Observation (ITC), Pietermaritzburg, South Africa, 23/09/2014.

Van der Kwaast, J, Timmermans, W, Gieske, A, Su, Z, Olioso, A, Jia, L, Elbers, J, Karssenberg, D and de Jong, S. 2009. Evaluation of the Surface Energy Balance System (SEBS) applied to Aster imagery with flux-measurements at the SPARC 2004 site (Barrax, Spain). *Hydrology and Earth System Sciences* 13(7): 1337-1347.

Van Dijk, AI and Renzullo, LJ. 2011. Water resource monitoring systems and the role of satellite observations. *Hydrology and Earth System Science* 15: 39–55.

Wagener, T, Sivapalan, M, Troch, PA, McGlynn, BL, Harman, CJ, Gupta, HV, Kumar, P Rao, CS, Basu, NB, and Wilson, JS. 2010. The future of hydrology: An evolving science for a changing world, *Water Resources Research*, 46.

Walters, MO 1990. Transmission losses in arid regions. *Journal of Hydraulic Engineering ASCE* 116:129-38.

Timmermans, J, Su, Z, van der Tol, C, Verhoef, A and Verhoef, W. 2013. Quantifying the uncertainty in estimates of surface-atmosphere fluxes through joint evaluation of the SEBS and SCOPE models. Hydrological Earth Systems Science. 17: 1561–1573.

Timmermans, J. 2012. Personal communication. International Institute of Geo-information sciences and Earth Observation (ITC), Pietermaritzburg, South Africa, 06/2012.

Yang, D, Chen, H and Lei, H. 2010. Estimation of evapotranspiration using a remote sensing model over agricultural land in the North China Plain. *International Journal of Remote Sensing* 31(14): 3783–3798.

Zhang, H, Lan, Y, Lacey, R, Hoffman, WC and Westbrook, JK. Spatial analysis of NDVI readings with different sampling densities. *American Society of Agricultural and Biological Engineers* 54(1): 349-354.

Appendix I SEBS data - Letaba at Secondary to Quaternary Catchment Scale

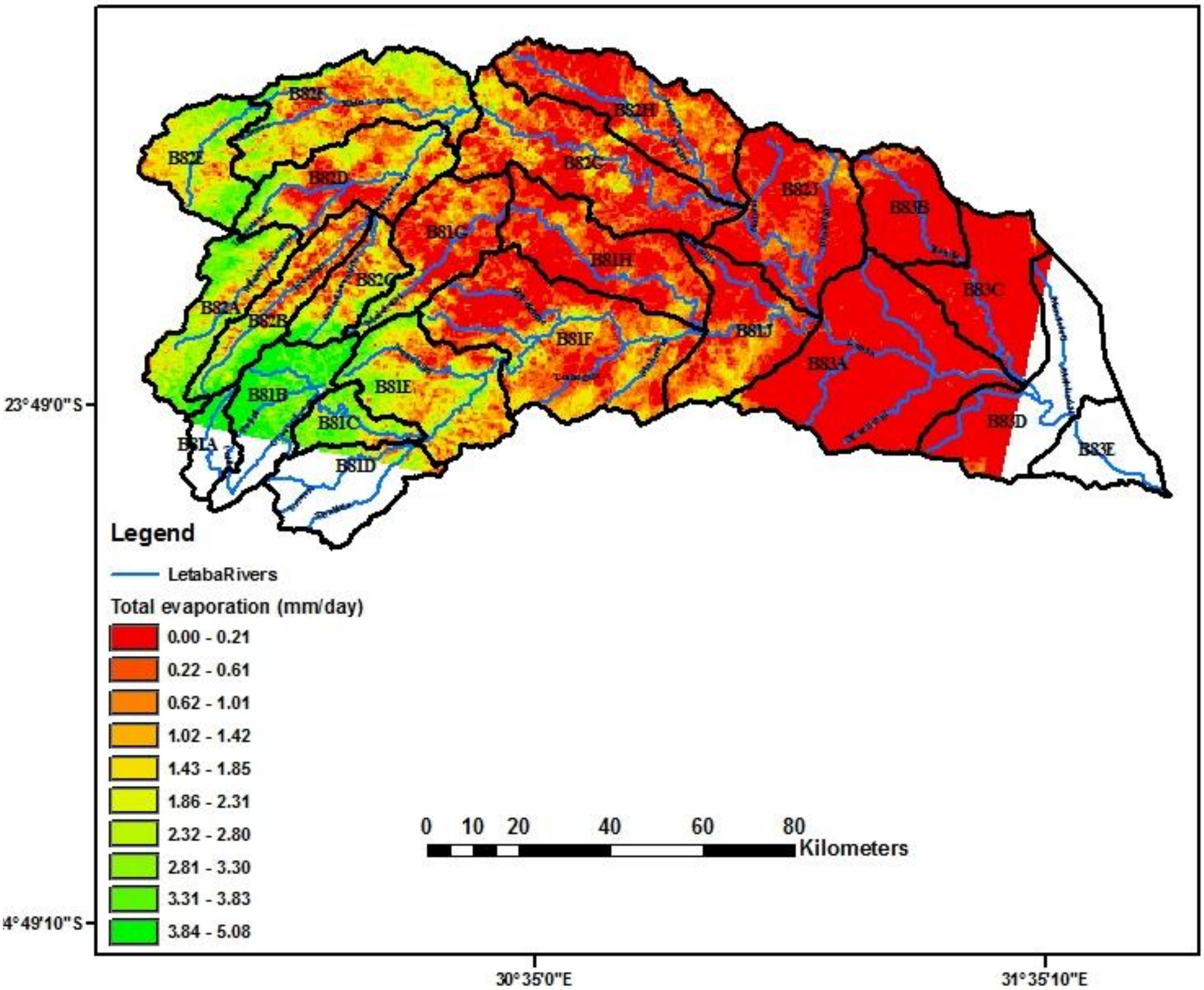

Figure A1.I: Variation of SEBS total evaporation over the Letaba catchment for the 20th May 2015

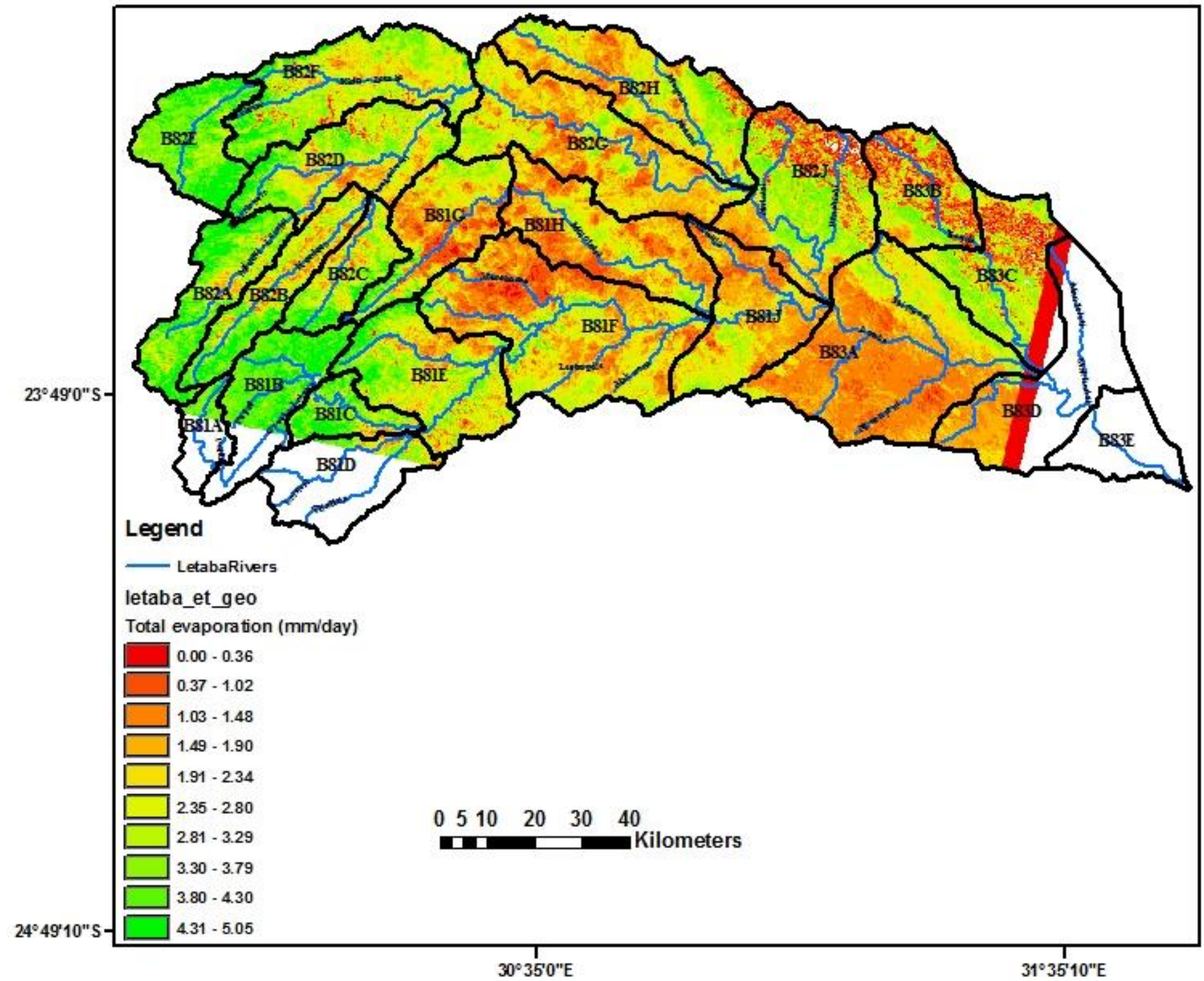

Figure A1.II: Variation of SEBS total evaporation over the Letaba catchment for the 05th June 2015

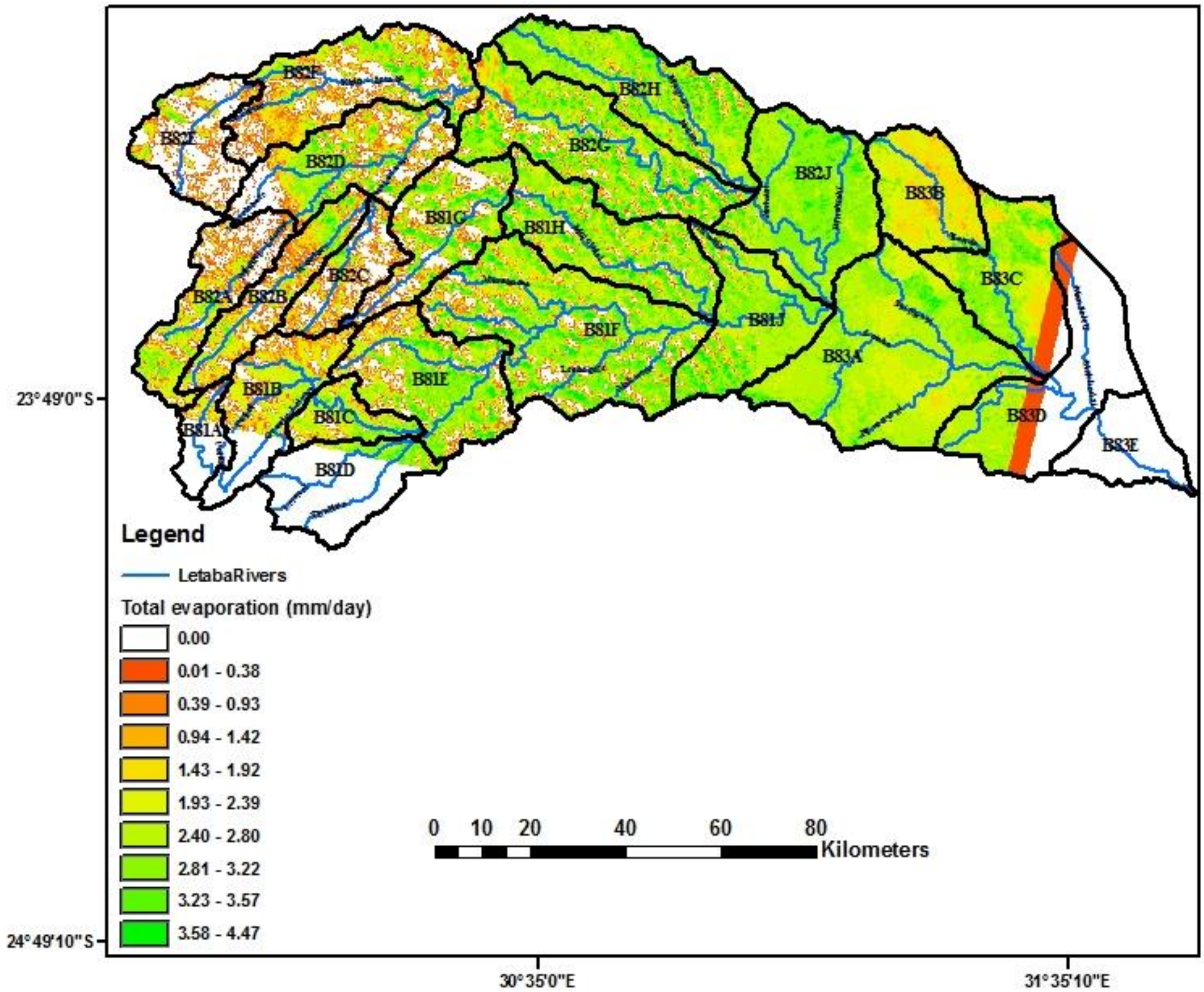

Figure A1.III: Variation of SEBS total evaporation over the Letaba catchment for the 21st June 2015

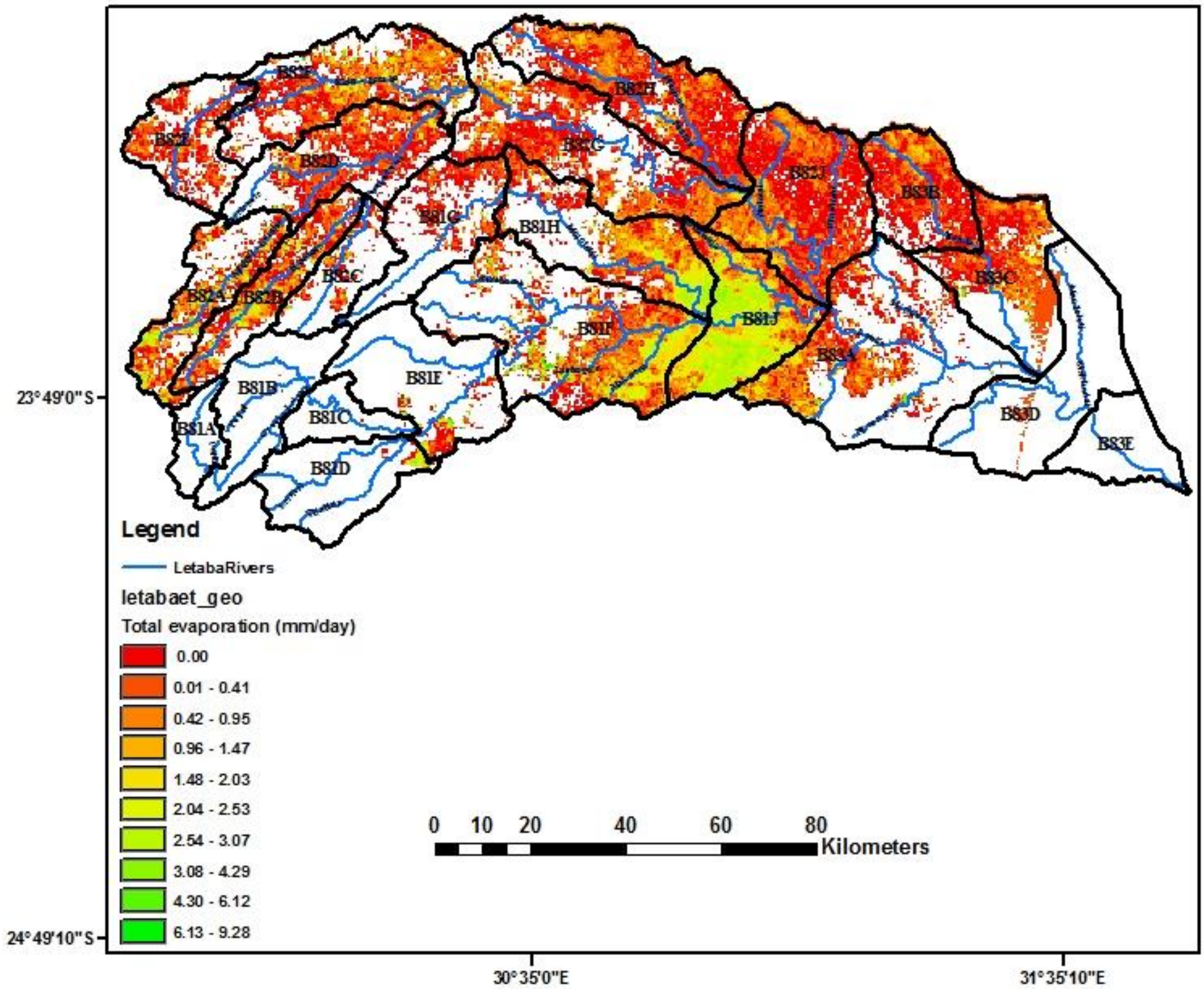

Figure AI.IV: Variation of SEBS total evaporation over the Letaba catchment for the 07th July 2015

Appendix II Site Instrumentation and Field Surveying

Figure A2.I: Location of the measurements at the Mahale Weir (B8H007)

Figure A2.II: Solinst Level Logger Installation at the Mahale weir to record streamflow head, installed on 22 April 2015.

Figure A2.III: Instream flow measurements upstream of the Mahale weir

Figure A2.IV: With Environmental Monitors measuring flow at the low flow pipes of the Mahale weir.

Figure A2.V: Installation of the Eddy Co-variance system in channel with location of sensors

Figure A2.VI: Performing Electro-Magnetic surveys in farms adjacent to the Letaba River.

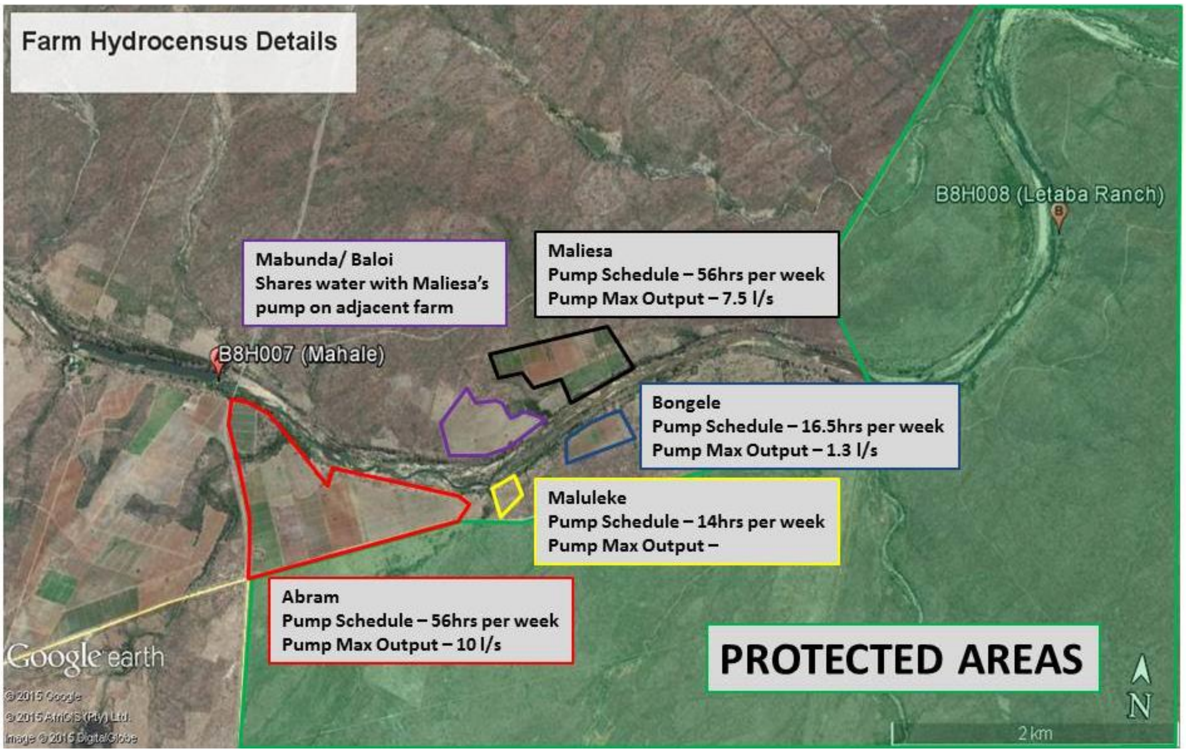

Figure A2.VII: Example updated hydro-census information for farms adjacent to the Letaba River.

Appendix III Borehole Drilling Logs

Of the total number of boreholes drilled thus far, three borehole logs have been explicitly analysed. These borehole logs are displayed in the following tables.

BOREHOLE NAME:	LF0051A	DEPTH (m):	54
Depth (m)	**Description**	**Average Chip Size (mm)**	**NOTES**
1	Orangey white, medium-highly weathered, granite	2-5	
2	Orangey white, medium-highly weathered, granite	2-5	
3	Black and white, medium-weathered, granite	~1	
4	Black and white, medium-weathered, granite	~1	
5	Black and white, medium-weathered, granite	~1	
6	Black and white, medium-weathered, granite with trace amounts of dark black with white, medium-weathered, gabbro/dolerite (10mm)	2-5	
7	Black and white, medium-weathered, granite with minor amounts of dark black with white, medium-weathered, gabbro/dolerite (5-10mm)	~1	
8	Dark black with white, medium-weathered, gabbro, with trace amounts of orangey white, medium-weathered, granite (~1mm)	2-5	Gold Muscovite and abundant black minerals present
9	Black and white, medium-weathered, granite	2-5	
10	Black and white, medium-weathered, granite	2-5	
11	Black and white, medium-weathered, granite	2-5	
12	White with black, slightly-weathered, granite	2-5	
13	White with black, slightly-weathered, granite	2-5	
14	White with black, slightly-weathered, granite	2-5	
15	White with black, slightly-weathered, granite	2-5	

16	White with black, slightly-weathered, granite	2-5	
17	White with black, slightly-weathered, granite	2-5	
18	White with black, slightly-weathered, granite	2-5	
19	White with black, slightly-weathered, granite	5-10	
20	White with black, slightly-weathered, granite	5-10	
21	White with black, slightly-weathered, granite	2-5	
22	White with black, slightly-weathered, granite	5-10	
23	White with black, slightly-weathered, granite	5-10	
24	White with black, slightly-weathered, granite	5-10	
25	White with black, slightly-weathered, granite with minor amounts of dark green, silty clay, residual granite	2-5	WATER STRIKE
26	Pinkish white with black, slightly-weathered, granite		
27	Pinkish white with black, slightly-weathered, granite		
28	Pinkish white with black, slightly-weathered, granite		
29	Pinkish white with black, slightly-weathered, granite		
30	Pinkish white with black, slightly-weathered, granite	~1	
31	Pinkish white with black, slightly-weathered, granite		
32	Pinkish white with black, slightly-weathered, granite with minor amounts of dark black/green, slightly-weathered, gabbro/dolerite		
33	Black green, slightly-weathered, gabbro/dolerite with equal parts of pinkish white with black, slightly-weathered, granite		
34	Black green, slightly-weathered, gabbro/dolerite with minor traces of pinkish white with black, slightly-weathered, granite		
35	Black green, slightly-weathered, gabbro/dolerite with minor traces of pinkish white with black, slightly-weathered, granite		

36	Black green, slightly-weathered, gabbro/dolerite with minor traces of pinkish white with black, slightly-weathered, granite		
37	Pinkish white with black, slightly-weathered, granite		
38	Pinkish white with black, slightly-weathered, granite		
39	Pinkish white with black, slightly-weathered, granite	2-5	
40	Pinkish white with black, slightly-weathered, granite	2-5	WATER STRIKE
41	Pinkish white with black, slightly-weathered, granite	2-5	
42	Pinkish white with black, slightly-weathered, granite	1-2	Abundant muscovite
43	Pinkish white with black, slightly-weathered, granite	2-5	
44	Pinkish white with black, slightly-weathered, granite	2-5	
45	Pinkish white with black, slightly-weathered, granite with minor amounts of black and white, slightly-weathered, gabbro/dolerite (5-10mm)	2-5	
46	Pinkish white with black, slightly-weathered, granite		
47	White with black, slightly-weathered, granite with black and white, slightly-weathered, gabbro-dolerite	5-10	
48	White with black, slightly-weathered, granite with black and white, slightly-weathered, gabbro-dolerite	2-5	
49	White with black, slightly-weathered, granite with black and white, slightly-weathered, gabbro-dolerite	2-5	
50	White with black, slightly-weathered, granite with black and white, slightly-weathered, gabbro-dolerite	2-5	
51	Black with white, unweathered, gabbro/dolerite		
52	Black with white, slightly-weathered, gabbro/dolerite		
53	Black with white, slightly to ununweathered, gabbro/dolerite		
54	Black with white, unweathered, gabbro/dolerite		

Figure A3.I: Students analysing borehole logs

BOREHOLE NAME:	LF003B	DEPTH (m):	20
Depth (m)	**Description**	**Average Chip Size (mm)**	**NOTES**
1	Red/ brown, silty sand, alluvium with trace amounts of brownish/white with black, highly-weathered, granite	2-5	
2	Red/ brown, silty sand, alluvium with trace amounts of brownish/white with black, highly-weathered, granite	2-5	
3	Red/ brown, silty sand, alluvium with trace amounts of brownish/white with black, highly-weathered, granite	2-5	
4	Light brown, silty sand, alluvium with trace amounts of brownish white with black, highly-weathered, granite	2-5	
5	Light brown, silty sand, alluvium with trace amounts of brownish white with black, highly-weathered, granite	2-5	
6	Light brown, silty sand, alluvium with trace amounts of brownish white with black, highly-weathered, granite	2-5	
7	Light brown, silty sand, alluvium with trace amounts of brownish white with black, highly-weathered, granite	5-7	
8	Brown/ red, sandy gravel, alluvium		
9	Brown/ red, silty sand, alluvium		
10	Brown/ red, sandy gravel, alluvium		
11	Brown/ red with black, silty sand, alluvium with trace amounts of black with white, highly-weathered, granite		

12	Brown/ red with black, silty sand, alluvium with abundant amounts of black, medium-weathered, shale		WATER STRIKE
13	Black, medium-weathered, shale with trace amounts of brown/red with black, silty sand, alluvium		
14	Black, medium-weathered, shale	5-10	
15	Black, medium-weathered, shale	10-20	
16	Black, medium-weathered, shale	10-20	
17	Black, medium-weathered, shale	5-10	
18	Black, medium-weathered, shale	5-10	
19	Black, medium-weathered, shale with trace amounts of brownish, medium-weathered, quartz	5-10	
20	Black, medium-weathered, shale with trace amounts of brownish, medium-weathered, quartz	5-11	

BOREHOLE NAME:	LF005B	DEPTH (m):	42
Depth (m)	**Description**	**Average Chip Size (mm)**	**NOTES**
1	Red/ brown, silty sand, alluvium with trace amounts of brownish with white, highly-weathered, granite	2-5	
2	Red/ brown, silty sand, alluvium with trace amounts of brownish with white, highly-weathered, granite	2-5	
3	Red/ brown, silty sand, alluvium with trace amounts of brownish with white, highly-weathered, granite	2-5	
4	Red/ brown, silty sand, alluvium with trace amounts of brownish with white, highly-weathered, granite	2-5	
5	Red/ brown, silty sand, alluvium with trace amounts of brownish with white, highly-weathered, granite	2-5	
6	Red/ brown, silty sand, alluvium with trace amounts of brownish with white, highly-weathered, granite	2-5	
7	Red/ brown, silty sand, alluvium with trace amounts of brownish with white, highly-weathered, granite	2-5	
8	Red/ brown, silty sand, alluvium with trace amounts of brownish with white, highly-weathered, granite	2-5	
9	Brown, silty sand, alluvium with trace amounts of brown, highly-weathered,	5-7	

	granite		
10	Brown, highly-weathered, granite	5-7	
11	Brown, highly-weathered, granite	5-7	
12	Brown/ grey, highly-weathered, granite	8-10	
13	Brownish cream, medium-weathered, granite with trace amounts of black dolerite (iron-stained)	10	WATER STRIKE
14	Brownish cream, medium-weathered, granite with trace amounts of black dolerite (iron-stained)	15	
15	Brownish cream, medium-weathered, granite with trace amounts of black dolerite	10	
16	Brownish cream, medium-weathered, granite with trace amounts of black dolerite (iron-stained)	10	
17	Brownish cream, medium-weathered, granite with trace amounts of highly-weathered black shale (iron-stained)	10	
18	Brownish cream, medium-weathered, granite with trace amounts of medium-weathered, black dolerite (iron-stained)	10	
19	Brownish cream with red, medium-weathered, granite with trace amounts of dolerite	10	
20	Brownish cream with red, medium-weathered, granite with trace amounts of dolerite	10	
21	Brownish cream with red, medium-weathered, granite with trace amounts of medium-weathered, dolerite	10-15	
22	Brownish cream with red, medium-weathered, granite with trace amounts of slightly-weathered, dolerite	10	
23	Brownish cream with red, medium-weathered, granite with trace amounts of slightly-weathered, dolerite	5-10	
24	Brownish cream with red, medium-weathered, granite with trace amounts of slightly-weathered, dolerite	8-10	
25	Brownish cream,red with black, medium-weathered, granite with trace amounts of unweathered, dolerite	10-15	
26	Brownish cream,red with black, medium-weathered, granite with trace amounts of unweathered, dolerite	10-15	
27	Brownish cream,red with black, medium-weathered, granite with trace amounts of unweathered, dolerite	10-15	

28	Brownish cream with red, slightly-weathered, granite	2-5	
29	Brownish cream with red, slightly-weathered, granite with trace amounts of dolerite (iron-stained)	5-7	
30	Brownish cream with red, slightly-weathered, granite with trace amounts of unweathered dolerite (iron-stained)	5-7	
31	Greyish brown with red, unweathered, granite	2-5	
32	Greyish cream, red with black mafic minerals, unweathered, granite	2-5	
33	Greyish cream, red with black mafic minerals, unweathered, granite	2-5	slight iron-staining
34	Greyish cream, red with black mafic minerals, unweathered, granite	2-6	
35	Grey/ Black with brown, unweathered, granite	10	
36	Grey/ Black with brown, unweathered, granite with trace amounts of iron-stained dolerite	5-7	
37	Grey/ Black with brown, unweathered, granite	5-7	
38	Grey/ Black with brown, unweathered, granite	5-7	
39	Grey/ Black with brown, unweathered, granite	5-7	
40	Grey/ Black with brown, unweathered, granite	5-7	
41	Grey/ Black with brown, unweathered, granite	5-7	
42	Grey/ Black with brown, unweathered, granite	5-7	

Figure A3.II: Example of a borehole log collected before analysis and how samples look after rinsing.

Appendix IV Letaba Storm, 27th April 2015 – Stakeholder Report to Farmers and Reserve Managers

STAKEHOLDER REPORT

LETABA STORM – 27TH APRIL 2015

A total of three Davis™ Weather Stations (Fig. 1) are scattered across an area covering the Selwane, Mbaula and Phalaubeni villages. During the time of the storm, the weather stations were recording various climatic variables (such as temperature, humidity, wind direction, wind speed, rainfall intensity and quantity) at 30 minute intervals. Additionally, a logger was installed at Mahale Weir to record depth of the river and water temperature at 5 minute intervals. A detailed time-line of events recorded at the three weather stations is provided below.

Figure 1 The locations of the three Davis weather stations scattered across the study site.

TIME	RIVER CONDITIONS	MAHALE FARM (SELWANE)	MTHIMKHULU PRIVATE RESERVE	PHALAUBENI
27/04/2015 22:30	Background water temperature was 27°C	1. Wind direction changed from an Easterly direction to a Southerly direction 2. Rain/ hail begins to fall	1. Wind direction changed from an Easterly direction to a Southerly direction (similar to Mahale Farm) 2. Rain/ hail begins to fall (similar to Mahale Farm)	
23:00	Water temperature dropped to 25°C	1. Air temperature dropped from 23°C to 16°C. 2. Wind speed increased from approx. 1.5 km/h to 6.4 km/h. 3. Rain intensity peaked at 311.4 mm/h.	1. Air temperature dropped from 24°C to 19°C.	
23:05	Sudden temperature drop to 4°C			
23:15	Lowest temperature recorded at 1.7°C; water level started rising			
23:20	Water temperature remained extremely low for many hours following the storm. Temperatures fluctuated between 3°C-10°C			
23:30		Wind speed peaks at 11.3 km/h	1. Rain intensity peaked at 640 mm/h. 2. Wind speed peaks at 11.3 km/h (similar to Mahale farm)	1. Air temperature dropped from 24°C to 17°C. 2. Rain intensity peaked at 768 mm/h.
00:00		Wind changes direction and wind speed dies down to 1.5 km/h again		Rain intensity decreased to 51.6 mm/h.
02:00			Wind speed dies down to 1.6 km/h again (later than Mahale Farm)	
28/04/2015 08:15				
20:05	Water temperature returned to a decent temperature of 25°C			
NOTES:	River level rose by 30cm at 02:45 (28/04/2015) and returned to its pre-storm level by 08:00. This significant rise in water level would not have been witnessed due to the time of morning.	Between 22:30-23:00, 23.6mm of rain* fell	Between 22:30-00:30, 42.2mm of rain* fell	Between 23:00-01:00, 27.6mm of rain* fell

* Inaccurate value due to a combination of rain and hail. Water stations are not designed to record hail readings. Furthermore, hailstones collected in the rain gauge bucket would slowly melt and mimic raindrops falling onto rainfall measuring instruments.

STORM SUMMARY:

* Phalaubeni Village was the worst hit by the storm. The storm lasted longer in Phalaubeni (nearly 3 hours) than in Mahale Farm (1.5 hours) and Mthimkhulu (2 hours). Rain intensity was greatest than Mahale Farm and Mthimkhulu.

* Mahale Farm and Mthimkhulu experienced similar storm conditions but the rain intensity at Mthimkhulu was about double that of Mahale Farm.

* Fish deaths were reported in Letaba River following the storm. This is most likely due to the sudden decrease in water temperature as indicated by the temperature logger submerged in the river during the storm at Mahale Weir (Fig. 3).

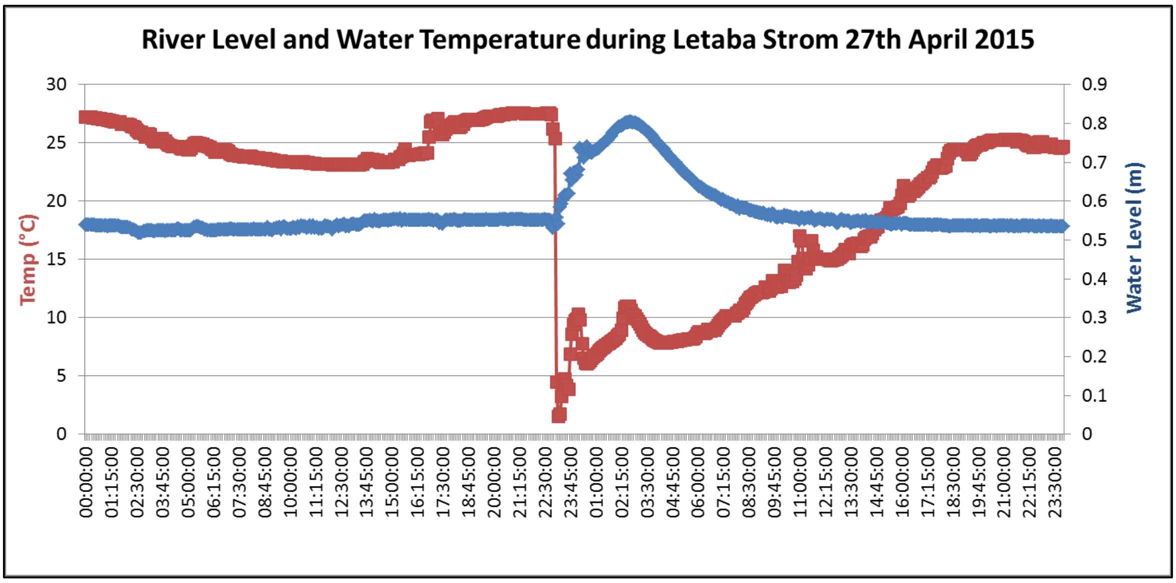

Fig. 3 River level readings and water temperature measurements collected at 5 minute intervals during the 27th April 2015 storm.

Fig. 4 Photos of hail which fell 27th April 2015.

(Photos courtesy of Thinus Jansen van Vuuren)

Report Complied By:	Tercia Strydom (SANParks: Scientific Services)
Date:	07/08/2015
Collaborating Organizations:	SAEON Ndlovu Node
	University of KwaZulu-Natal
	GCS Pretoria